Optoelectronic Structure Fabrication by Organometallic Vapor-Phase Epitaxy and Selective Epitaxy

Thesis by

Charles Su-Chang Tsai

In Partial Fulfillment of the Requirements

for the Degree of

Doctor of Philosophy

California Institute of Technology

Pasadena, California

1996

(Submitted May 16, 1996)

Acknowledgements

I would like to express my gratitude to Professor Kerry J. Vahala, my thesis advisor, for his guidance and support. He provided many ideas of fundamental importance to the work presented here, including that of using selective epitaxy in fabricating nanostructures. His advice, both in regard to this thesis and other matters, was indispensable.

I thank Professor Axel Scherer for his encouragement and technical advice, and his graduate students, especially Oskar Painter, for processing the samples from the visible VCSEL project. I also thank Robert Lee for the many many hours he spent at JPL assisting me during the OMVPE growths.

I thank John Lebens and Professor Thomas Kuech for their guidance and assistance during the initial work in selective epitaxy. John taught me the critical skills of sample processing, e-beam lithography, and scanning electron microscopy. Professor Kuech introduced me to the OMVPE growth technique.

I am grateful to everyone who had helped me in the course of my graduate work. I thank Mike Hoenk, Mike Newkirk, Channing Ahn, Gang He, Peter Sercel, Paul Maker, Rich Muller, Akbar Nouhi, James Singletery, and Siamak Forouhar for their assistance during various stages of this work. And most of all, I am grateful to my family for their support.

I am also grateful to the AT&T Foundation and the National Science Foundation for providing fellowship support for my graduate studies.

Abstract

The internal configuration and external supports of OMVPE reactors are examined. The quality of epitaxial layers deposited by an OMVPE reactor is strongly influenced by its internal configuration. The quality of the external supports determines the safety, the environmental impact, and the operating efficiency of the OMVPE reactor.

Optoelectronic structures are fabricated by selective epitaxy. The morphology and growth behavior of GaAs, AlGaAs, and InGaAs using selective epitaxy are presented. Highly selective growth can be achieved through the use of organometallic compounds which contain halogens. The selective growth of nanometer-scale GaAs wire and dot structures is demonstrated. Spectrally-resolved cathodoluminescence images as well as spectra from single dots and wires, passivated by an additional AlGaAs layer, are presented. A blue shifting of the GaAs luminescence peak is observed as the size scale of the wires and dots decreases. Formation of highly-uniform and densely-packed arrays of GaAs dots by selective epitaxy is described. The smallest GaAs dots formed are 15-20 nm in base diameter and 8-10 nm in height with slow-growth crystallographic planes limiting growths of individual dots. Completely selective GaAs growth within dielectric-mask openings at these small size-scales is also demonstrated. The technique of facet-modulation selective epitaxy and its application to quantum-well wire doublet fabrication are described. The smallest wire fabricated has a crescent cross-section less than 140 Å thick and less than 1400 Å wide.

The development of OMVPE epitaxial layers for a visible-wavelength vertical-cavity surface-emitting laser (VCSEL) is presented. The defect density of the mirror layers was reduced to a negligible level by optimizing gas switching. Electroluminescence spectrum of an InGaP heterostructure p-n diode is presented. The defect density of the active region was also reduced to a negligible level by optimizing the gas-switching sequences.

Table of Contents

List of Figures

Chapter 1

Introduction

1.1 Introduction to OMVPE

Organometallic vapor-phase epitaxy (OMVPE), often referred to as metal-organic chemical-vapor deposition (MOCVD) or other permutations of these same letters (MOVPE or OMCVD), began with the work of Manasevit [1-3] in the late 1960s. In OMVPE, organometallic (OM) compounds such as trimethylgallium (TMGa) or trimethylindium (TMIn), and hydride gases such as arsine (AsH_3) or phosphine (PH_3), are utilized in an OMVPE reactor for the epitaxial growth of semiconductor materials such as GaAs or InP [4]. In the OMVPE reactor, the OM compounds and the hydride gases flow over a semiconductor substrate that is heated and supported by a hot graphite susceptor. The OM compounds and the hydride gases decompose thermally and deposit epitaxial material on the substrate. Normally an additional large flow of a carrier gas such as hydrogen conveys the OM compounds and the hydride gases onto the substrate.

Compared to other epitaxial growth techniques such as molecular-beam epitaxy (MBE) or liquid-phase epitaxy (LPE), the chemistry of the OMVPE process is more complex. In MBE, simple elemental sources such as gallium and arsenic are evaporated at a controlled rate onto a heated substrate under ultra-high-vacuum (UHV) conditions for the epitaxial growth of semiconductor materials such as GaAs. In LPE, epitaxial materials such as GaAs are grown on a substrate as the substrate contacts molten solutions of semiconductor compounds dissolved in metal, such as GaAs dissolved in Ga. Although both MBE and LPE offer simpler chemistry, OMVPE is more versatile. For example, the growth of compounds containing both Al and In is nearly impossible in LPE, and the growth of alloys containing both As and P is particularly difficult in MBE, but the growth of these materials is routine in OMVPE.

As will be shown in this thesis, the more complex chemistry of the OMVPE process offers many useful variations in the epitaxial-growth process. Selective epitaxy, or the laterally controlled growth of epitaxial material within dielectric-mask openings on a substrate, was achieved here with complete selectivity by substituting the conventional OM compounds with halogenated OM compounds. In selective epitaxy, the epitaxial growth of material is controlled in three dimensions instead of in one dimension as in conventional OMVPE. This three-dimensional control of epitaxy has resulted in the first demonstration of selectively grown nanometer-scale structures.

1.2 Outline of the Thesis

This thesis can be divided into three parts. Chapters 2 and 3 describe the physical configuration of the OMVPE reactors utilized for this work. Chapters 4 to 7 describe the experimental efforts and results in the fabrication of optoelectronic structures using selective epitaxy. Chapter 8 describes the experimental efforts to fabricate a visible-wavelength *vertical-cavity surface-emitting* laser (VCSEL) by OMVPE.

In chapter 2, the internal configuration of OMVPE reactors is examined in detail. The quality of epitaxial layers deposited by an OMVPE reactor is strongly influenced by its internal configuration. Design variations are described in relation to their potential impacts on the quality of epitaxial layers produced. Comparisons are made between a "Reactor A" and a "Reactor B" to illustrate the similarities and differences between an earlier-generation reactor and a state-of-the-art reactor.

In chapter 3, the external supports for OMVPE reactors are examined in detail. The external supports for an OMVPE reactor do not directly influence the quality of epitaxial layers deposited by the OMVPE reactor. Instead, the quality of the external supports determines the safety, the environmental impact, and the operating efficiency of the OMVPE reactor. Specific examples will be used to illustrate possible variations in the external supports and their consequences on the safety, the environmental impact, and the operating efficiency of OMVPE reactors.

In chapter 4, experimental results on the morphology and growth behavior of GaAs, $Al_xGa_{1-x}As$ and $In_xGa_{1-x}As$ using selective epitaxy are presented. Highly selective growth can be achieved through the use of organometallic (OM) sources which contain halogens, such as diethylgallium chloride $(C_2H_5)_2GaCl$ (DEGaCl), diethylaluminum chloride $(C_2H_5)_2AlCl$ (DEAlCl), and dimethylindium chloride $(CH_3)_2InCl$ (DMInCl). The single-layer materials and selectively grown heterostructures produced by this technique have been characterized. The interface between the selectively grown material and the underlying substrate was investigated and the conditions for achieving high-quality defect-free interfaces were determined.

In chapter 5, the selective growth of nanometer-scale GaAs wire and dot structures using OMVPE is demonstrated. Spectrally-resolved cathodoluminescence images as well as spectra from single dots and wires, passivated by an additional $Al_xGa_{1-x}As$ layer, are presented. Growth behavior of GaAs wires with thick $Al_xGa_{1-x}As$ overgrowths is also presented for potential device applications. A blue shifting of the GaAs luminescence peak is observed as the size scale of the wires and dots decreases.

In chapter 6, formation of highly-uniform and densely-packed arrays of GaAs dots by selective epitaxy is described. The arrays of GaAs dots are imaged using atomic-force microscopy (AFM). Accounting for the AFM tip radius of curvature, the smallest GaAs dots formed are 15-20 nm in base diameter and 8-10 nm in height with slow-growth crystallographic planes limiting growths of individual dots. Completely selective GaAs growth within dielectric-mask openings at these small size-scales is also demonstrated. The uniformity of the dots within each array ranged from 6% for the larger dots to 16% for the smallest dots.

In chapter 7, the technique of facet-modulation selective epitaxy, a variation of selective epitaxy, and its application to quantum-well wire doublet fabrication are described. Successful fabrication of wire doublets in the $Al_xGa_{1-x}As$ material system is achieved. The smallest wire fabricated has a crescent cross-section less than 140 Å thick and less than 1400 Å wide. Backscattered-electron images, transmission electron micrographs, cathodoluminescence spectra, and spectrally-resolved cathodoluminescence images of the wire doublets are presented.

In chapter 8, the development of OMVPE epitaxial layers for a visible-wavelength vertical-cavity surface-emitting laser (VCSEL) is presented. Passive fabry-perot cavities with $Al_{0.5}Ga_{0.5}As/AlAs$ $\lambda/4$-stack mirrors were grown as test structures for mirror calibration. The defect density of the mirror layers was reduced to a negligible level by optimizing gas-switching sequences during OMVPE growth. Transmission electron micrographs and reflectance measurements of one calibration cavity are presented. $In_{0.5}Ga_{0.5}P/In_{0.5}Al_{0.5}P$ heterostructure p-n diodes, processed by using the actual fabrication procedures for VCSEL, were prepared as an intermediate test structure for the $In_{0.5}Ga_{0.5}P/In_{0.5}Al_{0.2}Ga_{0.3}P/In_{0.5}Al_{0.5}P$ multiple-quantum-well (MQW) active region. Electroluminescence spectrum of the p-n diode is presented. Test structures containing only the MQW active region were grown. The defect density of the MQW active region was also reduced to a negligible level by optimizing the gas-switching sequences. Full structures containing both the mirror and the MQW active region were grown. Optical micrographs of these full structures are also presented.

Bibliography

[1] H. M. Manasevit, Appl. Phys. Lett. **12**, 156 (1968).

[2] H. M. Manasevit and W. I. Simpson, J. Electrochem. Soc. **116**, 1725 (1969).

[3] H. M. Manasevit, J. Crystal Growth **13/14**, 306 (1972).

[4] G. B. Stringfellow, *Organometallic Vapor-Phase Epitaxy*, Academic Press (1989).

Chapter 2

Internal Configuration of OMVPE Reactors

The quality of epitaxial layers deposited by an OMVPE reactor is strongly influenced by the internal configuration of the OMVPE reactor, where the quality of epitaxial layers is gauged by the purity of the deposited materials, the uniformity of material composition and thicknesses, the abruptness of transitions between different epitaxial layers, and the density of crystalline defects.

In this chapter, the internal configuration of OMVPE reactors is examined in detail. Design variations are described in relation to their potential impacts on the quality of epitaxial layers produced. Comparisons are made between a "Reactor A" and a "Reactor B" to illustrate the similarities and differences between an earlier-generation reactor and a state-of-the-art reactor. Specifically, "Reactor A" is the General-Air OMVPE reactor, and "Reactor B" is the AIXTRON 200/4 OMVPE reactor [1]. Both reactors are currently located at the Microdevices Laboratory (MDL), NASA Jet Propulsion Laboratory (JPL), Pasadena. Both reactors have been utilized extensively during the course of this thesis project. "Reactor B" was selected, procured, designed, manufactured, inspected, and brought on-line as a significant portion of this thesis project.

2.1 Basic Modules within OMVPE Reactors

Most OMVPE reactors, although complex in appearance, can be partitioned into several basic modules as illustrated in figure 2.1. These basic modules include: gas sources and carrier gases module, organometallic (OM) sources module, gas switching

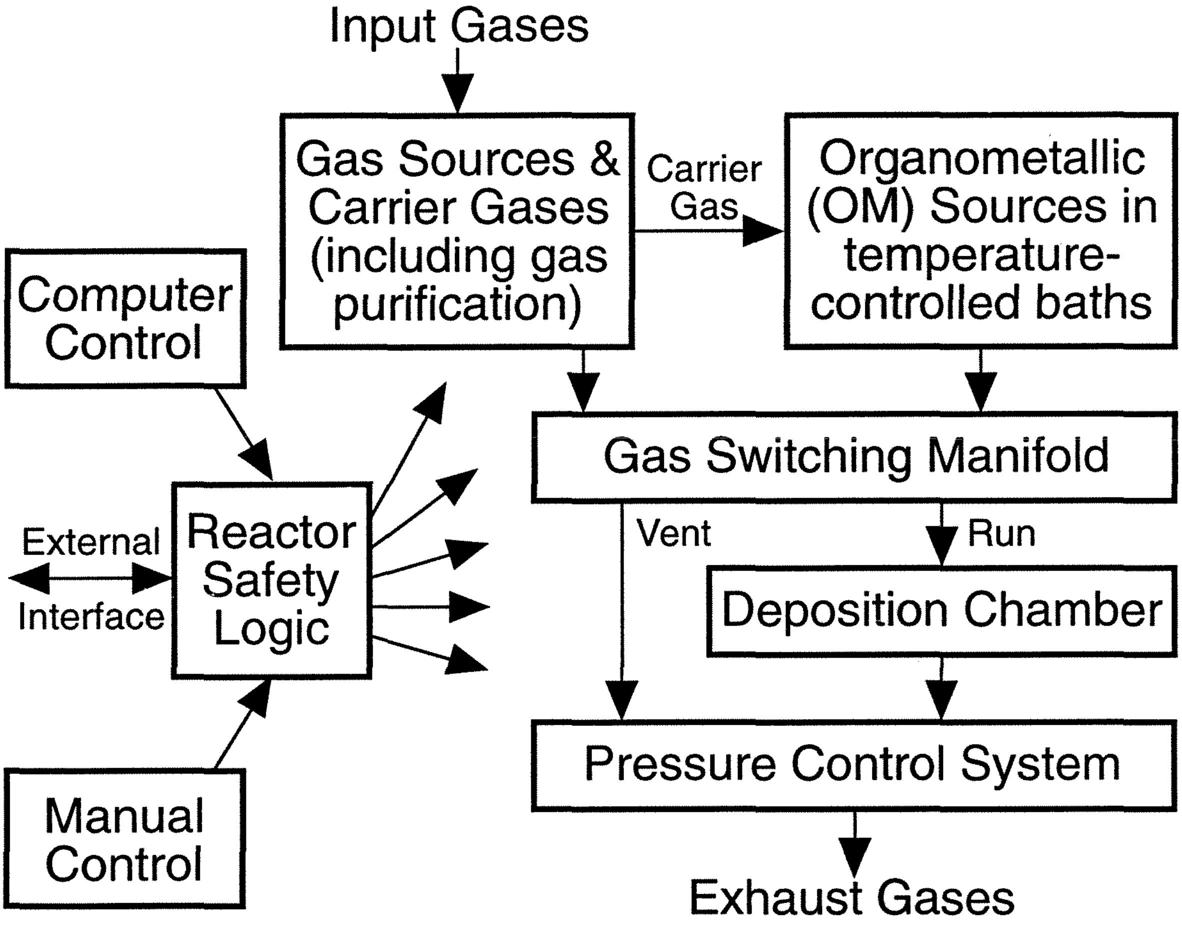

Figure 2.1. Schematic diagram of basic modules within an OMVPE reactor.

manifold, deposition chamber, pressure control system, computer control module, manual control module, and reactor-safety-logic module.

Input gases, for example hydrogen (H_2), nitrogen (N_2), arsine (AsH_3), phosphine (PH_3), and silane (SiH_4) required for the epitaxial growth of doped GaAs or InP semiconductor materials, are directed into the gas sources and carrier gases module. The input gases are purified and filtered to remove solid particles from the gas delivery lines and impurities such as water vapor (H_2O) or oxygen (O_2), which are impurities detrimental to the epitaxial growth of any material containing aluminum (Al) or silicon (Si).

Typically H_2 is purified by gas diffusion through a heated palladium (Pd) membrane, because H_2 is the only gas that can diffuse through such a membrane. Purification by Pd membrane results in exceedingly pure H_2 that is suitable for use as the main carrier gas in the OMVPE epitaxial growth process. Purification by forcing gases through chemically-activated-resin matrix, also commonly known as Nanochem®, is another popular technique for purifying N_2 and hydrides (AsH_3, PH_3, SiH_4) where the diffusion technique using a Pd membrane cannot be applied.

After purification, the gases required by the OMVPE epitaxial growth process are precisely measured and controlled by various arrangements of gas valves, mass-flow controllers, and/or pressure controllers, and subsequently directed into the gas switching manifold. In addition, carrier gases such as H_2 and N_2 are directed into the OM sources module.

In the OM sources module, carrier gases such as H_2 or N_2 are used as vapor carriers for OM materials. For each OM source, a carrier gas is forced through the OM source bubbler maintained at a constant temperature by immersion in a temperature-controlled recirculating-coolant bath. The carrier gas conveys a quantity of the OM material proportional to the vapor pressure of the OM material. The amount of OM material required by the OMVPE epitaxial growth process is precisely measured and controlled by various arrangements of gas valves, mass-flow controllers, and/or pressure controllers, and subsequently directed into the gas switching manifold.

The source gases, supplied by the gas sources and carrier gases module, and the OM materials, conveyed by carrier gases from the OM sources module, are mixed together in the gas switching manifold. Those source gases and/or OM materials required during a particular step of the OMVPE epitaxial growth process are directed into one or more run lines, and those source gases and/or OM materials not required are directed into the vent line. The run lines are routed to the deposition chamber, and the vent line bypasses the deposition chamber and is routed directly to the pressure control system.

In the deposition chamber, a substrate is placed on a susceptor. The susceptor and the substrate are heated to a temperature up to 800°C. For most OMVPE epitaxial growth processes, the gases flowing in the run lines are mostly H_2 gas that is mixed with trace amounts of OM materials ($<< 0.1\%$ of the total gas flow) and small amounts of hydride gases such as AsH_3 and/or PH_3 ($< 10\%$ of the total gas flow). When heated by the susceptor and the substrate, the OM materials and hydride gases decompose and deposit epitaxial layers on the substrate. After flowing over the hot susceptor and substrate, the depleted gases are directed into the pressure control system.

The pressure control system maintains the deposition chamber at a constant pressure, usually below atmospheric pressure. The operation of the pressure control system in an OMVPE reactor is made more complicated by the solid decomposition products and particles generated in the deposition chamber and by the acutely toxic gases such as AsH_3 and PH_3 present in the gas stream. Without a properly designed pressure control system, the solid components in the gas stream would quickly clog and damage the vacuum pump and gas valves in the system and result in an unusable OMVPE reactor.

After proceeding through the pressure control system, the gaseous waste from the vent line and the deposition chamber is conducted through stainless-steel tubing to the exterior of the OMVPE reactor for further treatment.

An OMVPE reactor is incomplete without the means to control its operations. For most reactors, computer-automated operation and manual operation are possible. Computer-automated operation allows an operator to program the sequences of a complex OMVPE epitaxial growth process before the growth. The actual growth process would be controlled entirely by the computer without any human intervention. Manual operation requires an operator to actuate valves, adjust mass-flow controller setpoints, etc., by physically moving toggle switches and turning knobs. Manual operation is possible only for the growth of the simplest epitaxial structures.

Reactor-safety-logic modules are included in certain OMVPE reactors, especially in newer reactors such as "Reactor B." This module oversees all of the operations of the OMVPE reactor to prevent actions or procedures which might result in damage to the reactor, injury to the human operator, release of toxic gases, or any other combinations thereof. In addition, this module verifies the correct operation of key components within the reactor. In the event of a serious malfunction internal to the reactor, such as a pump failure, or an emergency situation external to the reactor, such as a toxic gas release, the reactor would automatically revert to a safe condition, thereby preventing further problems from occurring.

2.2 Gas and OM Sources

The gas sources module and the OM sources module in an OMVPE reactor determines the overall performance of the OMVPE reactor. Figure 2.2 illustrates the different types of gas sources and OM sources, ranging from the simplest sources containing only one mass-flow controller to more elaborate sources containing multiple mass-flow controllers and one pressure controller. In general, the performance of the more elaborate sources is superior to the simplest sources in all respects except for the higher complexity, lower margin of stability, and higher initial cost.

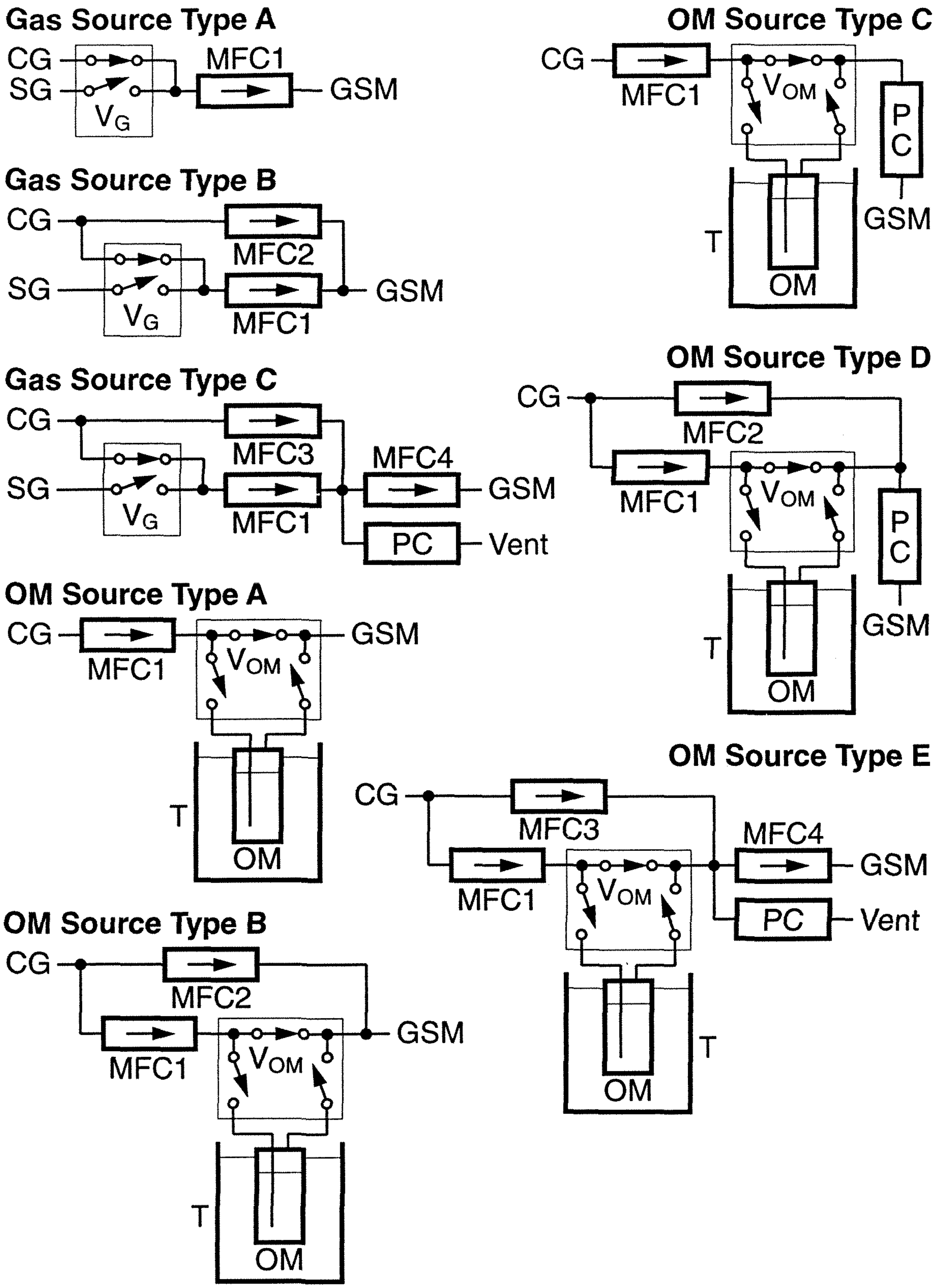

Figure 2.2. Schematic illustration of different types of gas sources and OM sources.

In gas source type A, the simplest gas source, a gas valve (V_G) selects between the carrier gas (CG) and the source gas (SG) and directs the gas flow through a mass-flow controller MFC1 into the gas switching manifold (GSM). The flow through MFC1 is called the source flow. The actual flow rate F (in sccm, standard cubic centimeter per minute) of the source gas delivered to the gas switching manifold is regulated by MFC1, and is equal to:

$$F = \frac{F_{\mathrm{MFC1}}\, X_{\mathrm{SG}}}{100},$$

and the partial pressure P of the source gas in the deposition chamber is equal to:

$$P = P_{\mathrm{D}} \frac{F}{F_{\mathrm{T}}},$$

where P_{D} is the absolute pressure measured in the deposition chamber, F_{MFC1} is the flow-rate setpoint (in sccm) of MFC1, X_{SG} is the actual concentration (in percent) of source gas supplied by the gas cylinder, and F_{T} is the total flow rate (in sccm) of gases entering the deposition chamber.

Although simple and low cost in construction, this type of gas source suffers from significant drawbacks. For flow rates F_{MFC1} less than about 50 sccm, it takes a significant amount of time for changes in flow rates F_{MFC1} to reach the gas switching manifold and to stabilize, which results in prolonged delays and compositional drifts during an epitaxial growth process. Excessively long interruptions between epitaxial layers can significantly increase impurity incorporation and defect density at the interfaces between epitaxial layers. This type of gas source is used exclusively in "Reactor A." As a result, it is essentially impossible to grow complex multilayer structures in this particular reactor.

In gas source type B, a gas valve selects between carrier gas and source gas and directs the gas flow into MFC1. In addition, a separate flow of carrier gas is directed into another mass-flow controller MFC2. The flows from MFC1 and MFC2 are combined as close to MFC1 as possible. The combined flow is directed into the gas switching manifold. The flow through MFC2 is called the pusher flow. The actual flow rate F of the source gas delivered to the gas switching manifold is regulated by MFC1, and is identical to the formulas presented for gas source type A.

The addition of MFC2 significantly improves the operation of this gas source. As the name suggests, the pusher flow increases the velocity of gas flow between MFC1 and the gas switching manifold. Changes and stabilization of flow rates that required minutes using gas source type A would take seconds to accomplish using gas source type B. This type of gas source significantly improves the OMVPE growth process, and is used exclusively in "Reactor B" for all non-dopant gas sources.

In gas source type C, a gas valve selects between carrier gas and source gas and directs the gas flow into MFC1. In addition, a separate flow of carrier gas is directed into another mass-flow controller MFC3. The flows from MFC1 and MFC3 are combined as close to MFC1 as possible. A portion of the combined flow is directed through a mass-flow controller MFC4 into the gas switching manifold. Remainder of the combined flow is directed through a pressure controller (PC) into the vent line of the pressure control system. The flow through MFC3 is called the dilution flow, and the flow through MFC4 the injection flow. The actual flow rate F (in sccm) of the source gas delivered to the gas switching manifold is equal to:

$$F = \frac{F_{\mathrm{MFC4}}\, F_{\mathrm{MFC1}}\, X_{\mathrm{SG}}}{100\,(F_{\mathrm{MFC1}} + F_{\mathrm{MFC3}})},$$

where F_{MFC3} is the flow-rate setpoint (in sccm) of MFC3 and F_{MFC4} is the flow-rate setpoint (in sccm) of MFC4.

The larger number of interacting active elements in this type of gas source contributes to the lower margin of stability, where flow-rate oscillations may occur under certain conditions. The flow rate F is more susceptible to variations and drifts, because F is dependent on the calibrations of multiple mass-flow controllers where cumulative errors may occur. In addition, a portion of the source gas is always discarded as waste gas during the operation of this gas source. This type of gas source is primarily used for controlling dopant gases where the required range of flow rates F is large in order to accommodate the order-of-magnitude changes in doping concentrations during an OMVPE epitaxial growth process. It is uncommon to use this type of gas source for main components of the epitaxial layers such as AsH_3 for As or PH_3 for P in GaAs or InP materials, where the precise control of flow is more important than the available dynamic range.

The different types of OM sources are also illustrated in figure 2.2. In OM source type A, the simplest OM source, a flow of carrier gas is directed through the mass-flow controller MFC1 into a gas valve assembly (V_{OM}). The gas valve assembly either directs the flow through the OM bubbler or allows the flow to bypass the OM bubbler. The flow from the gas valve assembly is directed into the gas switching manifold. The OM bubbler is maintained at a constant temperature T by immersion in a temperature-controlled recirculating-coolant bath. The flow through MFC1 is also called the source flow. The actual flow rate F (in sccm) of the OM material as a vapor delivered to the gas switching manifold is equal to:

$$F = \frac{F_{\mathrm{MFC1}}\, P_{\mathrm{OM}}[\mathrm{T}]}{P_{\mathrm{D}} - P_{\mathrm{OM}}[\mathrm{T}]},$$

where $P_{\mathrm{OM}}[\mathrm{T}]$ is the vapor pressure of the OM material at temperature T.

This type of OM source suffers from the same drawbacks as the gas source type A. In addition, F is strongly dependent on the chamber pressure P_{D}. Any small fluctuations in P_{D} is mirrored in F, which causes compositional fluctuations in epitaxial layers. In order to keep F constant, F_{MFC1} adjusted for one chamber pressure has to be changed when another chamber pressure is used. This type of OM source is also used exclusively in "Reactor A." As a result, it is essentially impossible to grow complex multilayer structures in this particular reactor.

In OM source type B, the addition of MFC2 results in the same improvements over OM source type A as gas source type B over gas source type A. The formula specified for OM source type A applies to OM source type B. Unfortunately, this OM source still suffers from the same sensitivity to chamber pressure as OM source type A.

In OM source types C and D, the addition of pressure controllers (PC) significantly improves the operation of these OM sources over OM source types A and B respectively. The actual flow rate F (in sccm) of the OM material as a vapor delivered to the gas switching manifold is equal to:

$$F = \frac{F_{\mathrm{MFC1}}\, P_{\mathrm{OM}}[\mathrm{T}]}{P_{\mathrm{PC}} - P_{\mathrm{OM}}[\mathrm{T}]},$$

where P_{PC} is the pressure setpoint of the pressure controller.

The additional pressure controller isolates the OM bubbler from the chamber pressure. The OM bubbler pressure can be set independently from the chamber pressure. F is independent of P_{D}. OM source type D significantly improves the OMVPE growth process, and is used exclusively in "Reactor B" for all non-dopant OM sources.

For OM source type E, the previous discussions on gas source type C also apply. The actual flow rate F (in sccm) of the OM material as a vapor delivered to the gas switching manifold is equal to:

$$F = \frac{F_{\mathrm{MFC4}}\, F_{\mathrm{MFC1}}\, P_{\mathrm{OM}}[\mathrm{T}]}{(F_{\mathrm{MFC1}} + F_{\mathrm{MFC3}})\,(P_{\mathrm{PC}} - P_{\mathrm{OM}}[\mathrm{T}])}.$$

2.3 Gas Switching Manifold

In an OMVPE reactor, a properly designed gas switching manifold is critical to the production of defect-free abrupt transitions between epitaxial layers. Two gas switching manifolds are illustrated in figure 2.3.

The source gases, supplied by the gas sources module, and the OM materials, conveyed by carrier gases from the OM sources module, are combined in the gas

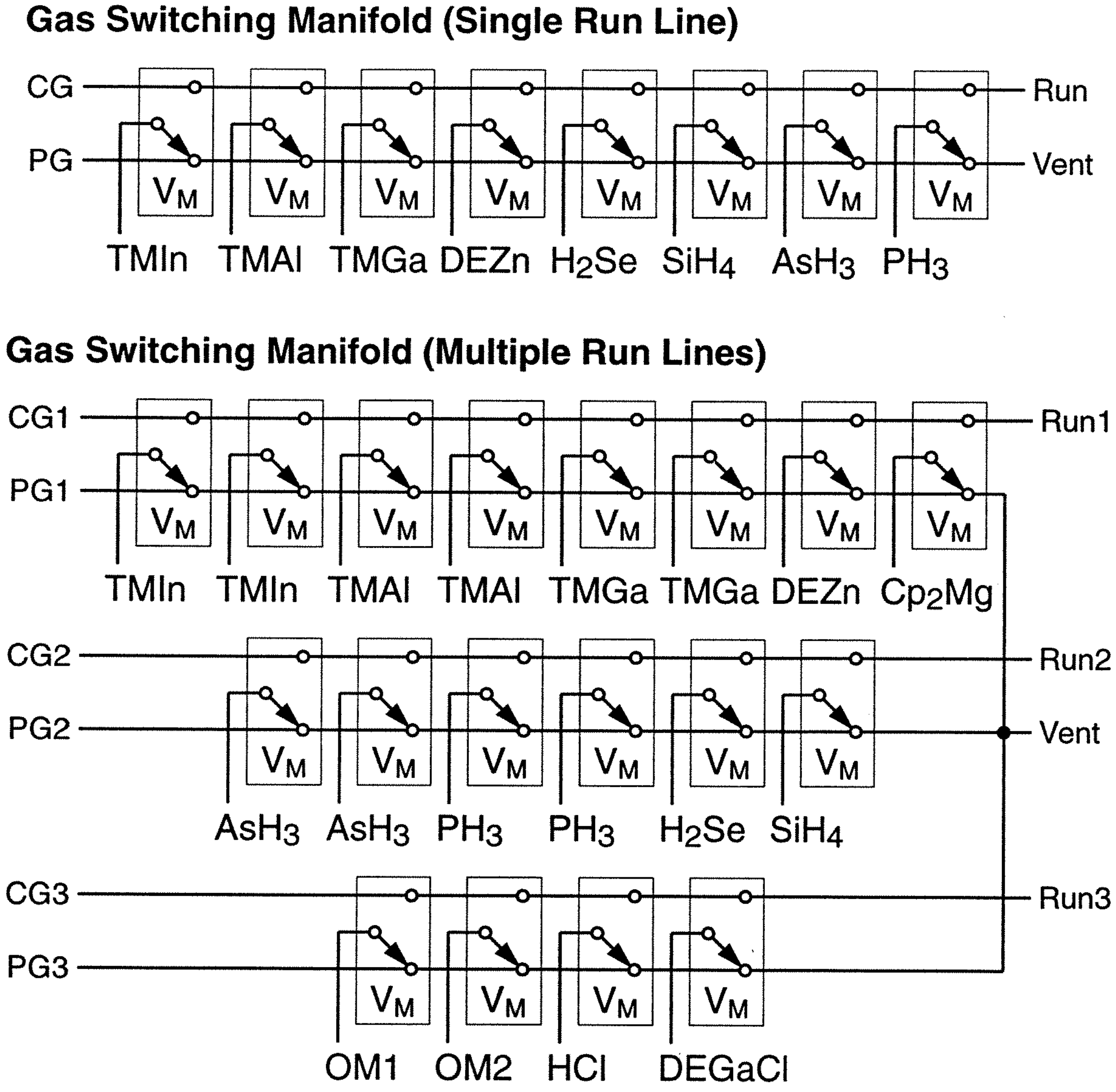

Gas Switching Manifold (Single Run Line)

Gas Switching Manifold (Multiple Run Lines)

Figure 2.3. Schematic illustration of two different gas switching manifolds.

switching manifold. Those source gases and/or OM materials required during a particular step of the OMVPE epitaxial growth process are directed by the manifold gas valves (V_M) into the run lines, and those source gases and/or OM materials not required are directed by the manifold gas valves into the vent line. The run lines are routed to the deposition chamber. The vent line bypasses the deposition chamber and is routed directly to the pressure control system.

Separate high flows of carrier gas (CG, CG1, CG2, and CG3) are maintained in the run lines (Run, Run1, Run2, and Run3). These flows, also called the main flows, provide a steady source of carrier gas into the deposition chamber when none of the manifold gas valves are directed into the run lines. These main flows also serve to quickly propel the source gases and/or OM materials into the deposition chamber, thereby making the exact placement of the manifold gas valve within the manifold inconsequential. For some OMVPE reactors, separate flows of purge gas (PG, PG1, PG2, and PG3) are also maintained in the vent lines (Vent) to quickly flush the unneeded source gases and/or OM materials into the pressure control system.

Properly designed manifold gas valves are critical for an OMVPE reactor. Any unpurged space (dead space) within a manifold gas valve must be minimized or eliminated. The unpurged spaces within the valve may act as reservoirs for source gases. Source gases from these reservoirs would leach out and cause compositional shifts or blurred interfaces between epitaxial layers in the OMVPE epitaxial growth process.

Another critical issue for the gas switching manifold is the equalization of pressure between the run lines and the vent lines. If large pressure imbalance exists between these lines, the switching of the manifold gas valves would produce glitches in the gas flow that disturb the OMVPE epitaxial growth process with effects ranging from minor compositional shifts to major increases in the density of crystalline defects.

Two different gas switching manifolds are illustrated in figure 2.3, one with single run line, and the other with multiple run lines. The manifold with single run line is implemented in "Reactor A." This manifold is restricted to source gases and OM materials which are chemically compatible. If there are parasitic reactions between the source gases and/or the OM materials, the manifold and the run line could be coated with the by-products from the parasitic reactions and the epitaxial layers could be contaminated. In addition, the number of sources that can be used at any one time is limited by the physical size of the single-run-line manifold.

The manifold with multiple run lines is implemented in "Reactor B." Compatible OM materials and source gases are grouped together for each run line, thereby eliminating any possible parasitic reactions. For example, conventional OM materials such as trimethylindium (TMIn), trimethylaluminum (TMAl), trimethylgallium (TMGa), diethylzinc (DEZn), and cyclopentadienylmagnesium (Cp_2Mg) are grouped together for Run1. Hydride gases such as AsH_3, PH_3, hydrogen selenide (H_2Se), and SiH_4 are grouped together for Run2. Others such as diethylgallium chloride (DEGaCl), hydrogen chloride (HCl), and experimental OM materials (OM1 and OM2) are grouped together for Run3. Many more sources can be used with this multiple-run-line manifold, including duplicate source gases and OM materials. Duplicate sources are necessary for the growth of complex multilayer structures because very little time, if any, is available between epitaxial layers to stabilize large changes in flow rates.

2.4 Deposition Chamber

The deposition chamber is where the deposition of epitaxial layers takes place. As shown in figure 2.4, a substrate, wafer or sample, is placed on a graphite susceptor. A quartz tube contains the susceptor and the substrate. In addition, the susceptor disk supporting the substrate in "Reactor B" also rotates during an epitaxial growth in order to achieve excellent uniformity in the composition and thicknesses of the epitaxial layers. As shown in figure 2.4, the susceptor disk rotates parallel to the main susceptor body about the rotation axis [2]. The susceptor disk is held in sustentation and caused to rotate

Deposition Chamber (Reactor A)

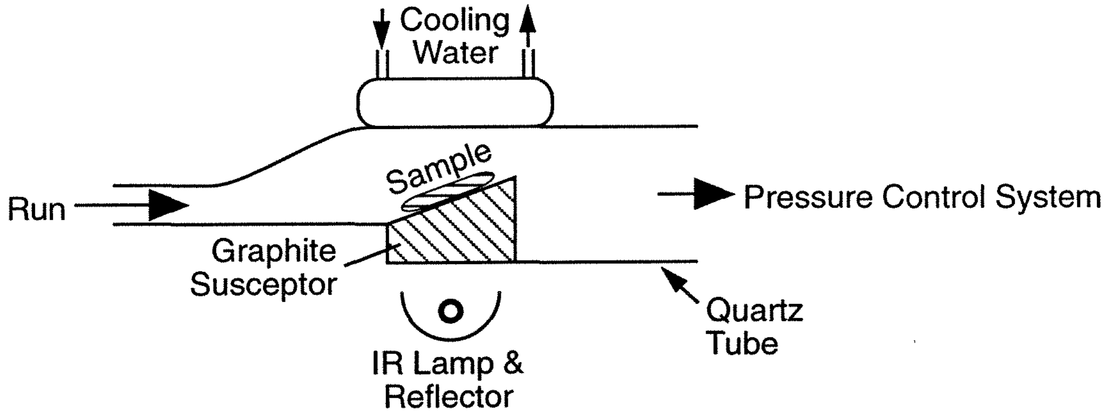

Deposition Chamber (Reactor B)

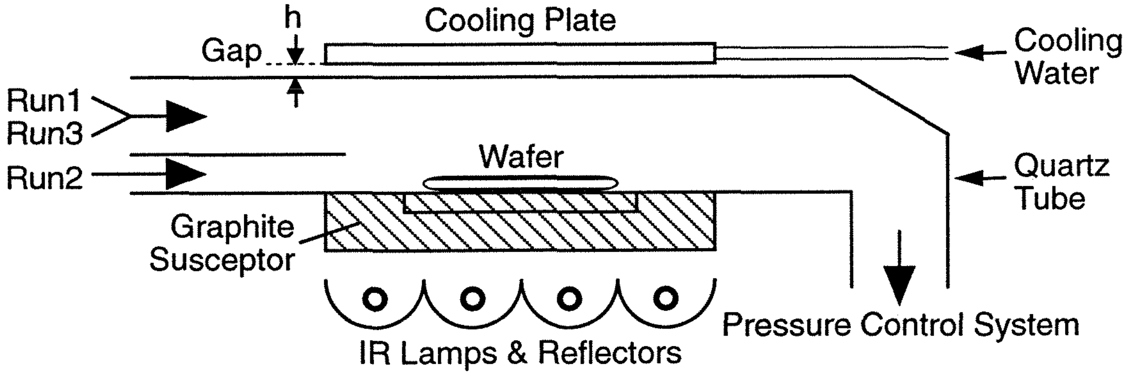

Gas-Flow Susceptor Rotation (Reactor B)

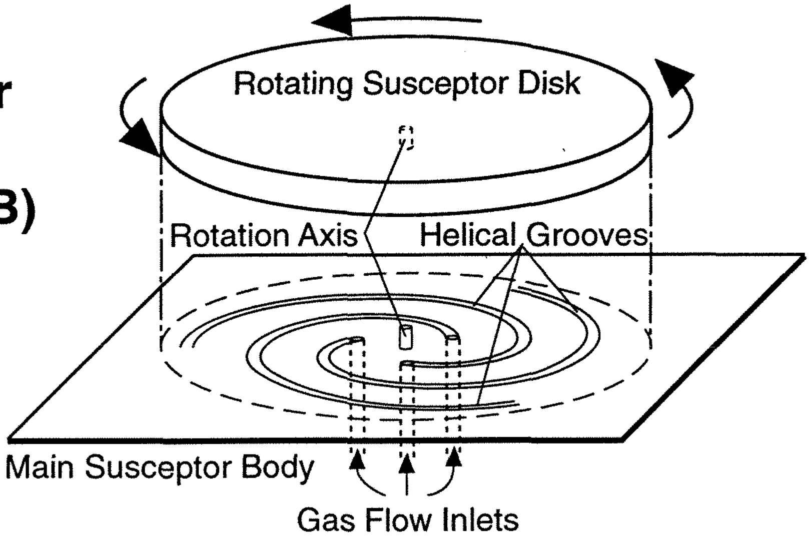

Figure 2.4. Schematic illustration of two different deposition chambers. Gas-flow susceptor rotation utilized in the deposition chamber of "Reactor B" is also shown.

in the indicated direction by the action of gas flow through several inlets into several helical grooves on the main susceptor body. The rotary movement is obtained by a force of viscosity of the gas. No particles are generated during susceptor rotation, because no frictional contact occurs between the susceptor disk and the susceptor body.

The susceptor and the substrate are heated by one or more infrared lamps with built-in water-cooled parabolic reflectors. The actual temperature of the susceptor is measured by a thermocouple placed into the susceptor. Feedback corrections are made to the power supplies for the infrared lamps to maintain the susceptor at a constant temperature.

In "Reactor A," the gases from one run line (Run) flow into the deposition chamber through a single inlet. In "Reactor B," the gases from three run lines (Run1, Run2, and Run3) flow into the deposition chamber through two separate inlets. The OM materials (Run1 and Run3) enter through the top inlet and the source gases (Run2) enter through the bottom inlet. The flows from these two inlets combine directly above the leading edge of the susceptor. This flow arrangement prevents the premature decomposition of the OM materials, and at the same time, enhances the decomposition of the source gases (hydride gases), because the OM materials decompose much more readily than the source gases when heated.

When heated by the susceptor and the substrate, the source gases and the OM materials in the gas flow decompose and deposit epitaxial layers on the substrate. After flowing over the hot susceptor and substrate, the depleted gas flow is directed into the pressure control system.

In "Reactor A," the ceiling of the quartz tube above the susceptor is cooled directly by water flowing through a quartz pocket incorporated into the quartz tube. In "Reactor B," the ceiling of the quartz tube above the susceptor is cooled indirectly by water flowing through a metallic cooling plate that is positioned at a small distance h away from the quartz tube. In addition, the deposition chamber of "Reactor B" actually consists of two concentric quartz tubes, an inner tube for containing the gas flow as shown in figure 2.4

and an outer tube to withstand the pressure from outside atmosphere (not shown). The space between the outer tube and the inner tube is purged by an adjustable mixture of H_2 and N_2.

Cooling the ceiling of the quartz tube prevents excessive decomposition and depletion of the source gases and OM materials on the quartz tube. However, the cooling method as implemented in "Reactor A" results in excessive condensation of OM materials on the quartz tube. The temperature of the ceiling is too low. The indirect cooling method utilized in "Reactor B" allows adjustments in the temperature of the ceiling by changing h and by changing the H_2/N_2 mixture in the gap (the thermal conductivity of H_2 and N_2 are different) [3]. With the appropriate h and H_2/N_2 mixture, the optimum ceiling temperature can be achieved, where the decomposition, depletion, and condensation of the source gases and OM materials on the inner quartz tube are minimized and the deposition of epitaxial materials on the substrate is maximized.

2.5 Pressure Control System

Stable performance of the pressure control system is critical to the reliable operation of an OMVPE reactor. During an epitaxial growth process, the pressure control system maintains the deposition chamber at a constant pressure, usually below atmospheric pressure. The solid decomposition products and particles generated in the deposition chamber and the acutely toxic gases such as AsH_3 and PH_3 present in the gas stream complicate the operation of the pressure control system. Without a properly designed pressure control system, the solid components in the gas stream would quickly clog and damage the throttle valve and the vacuum pump in the system which results in an useless OMVPE reactor. Figure 2.5 illustrates the major components within the pressure control system for an OMVPE reactor. This illustration presents a simplified version of a pressure control system implemented in an actual OMVPE reactor.

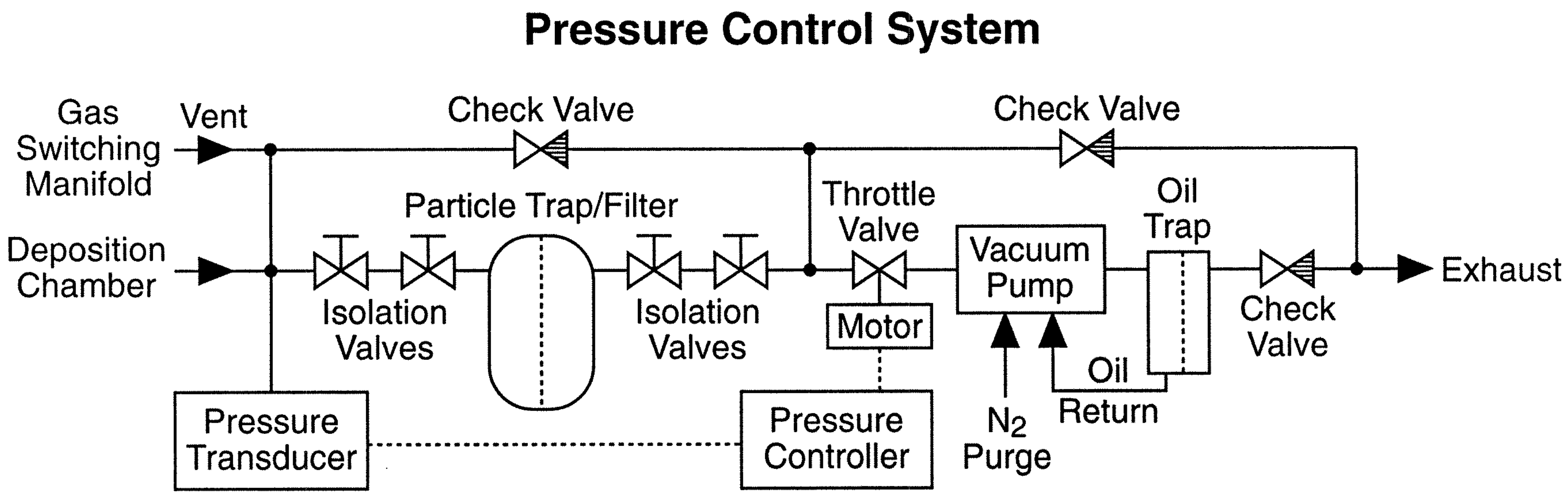

Figure 2.5. Schematic diagram of the major components within the pressure control system for an OMVPE reactor.

During normal operation, the depleted gases from the deposition chamber and the waste gases from the gas switching manifold are combined and directed through a particle trap/filter to remove solid particles in the gas flow. Deleterious contamination of the pressure control system is prevented by this placement of the particle trap/filter. A motorized throttle valve regulates the gas flow into the vacuum pump. The gaseous waste from the vacuum pump is conducted through stainless-steel tubing to the exterior of the OMVPE reactor for further treatment.

The absolute pressure in the deposition chamber is measured by a pressure transducer. Feedback corrections are made to the motorized throttle valve through a pressure controller module to maintain a constant chamber pressure. The placement of the pressure transducer is less than ideal as presented in figure 2.5. The solid particles generated in the deposition chamber can clog the tubing connected to the pressure transducer. A more favorable arrangement would be to place the pressure transducer somewhere upstream of the deposition chamber at a position where the flow of gas into the deposition chamber is not disrupted.

For safety reasons, several check valves are added to the pressure control system to prevent over-pressure or reverse-flow conditions in the OMVPE reactor. A check valve is placed in parallel with the particle trap/filter to allow for a path of gas flow when the particle trap/filter is clogged or is removed for maintenance or cleaning operations. A second check valve is placed in parallel with the vacuum pump to allow for a path of gas flow when the vacuum pump is shutdown for any reason. Another check valve is placed at the output of the vacuum pump to prevent reverse flow of gases into the vacuum pump. This reverse flow could be caused by the reverse rotation of the pump motor.

Two pairs of isolation valves are added in the path of the particle trap/filter. These valves facilitate the removal of the particle trap/filter without exposing the inside of the reactor or the particle trap/filter to outside air. The inner surfaces of the reactor and, to a much greater extent, the filter element inside the particle trap/filter are coated with arsenic and phosphorous residues. If either is exposed to outside air, spontaneous combustion would instantly occur and produce toxic gases such as AsH_3 and PH_3 and various oxides of arsenic and phosphorous.

For pumping toxic hydride gases such as AsH_3 and PH_3, the vacuum pump is filled with a special pump fluid, Fomblin® (PFPE: perfluoropolyethers), that is chemically inert when exposed to these gases and their decomposition products such as phosphoric acid. In addition, a continuous flow of purge gas N_2 into the vacuum pump is maintained to flush out the toxic and corrosive gases entering the vacuum pump. An oil trap with an oil return line connected to the vacuum pump is also highly recommended, because Fomblin® is extremely expensive.

Based on the basic design presented here, pressure control systems can be developed to meet the specific needs of individual OMVPE reactors.

Bibliography

[1] Product brochures for *AIX 200/4, AIX 200*, AIXTRON GmbH, Aachen, Germany, 1992.

[2] P. M. Frijlink, *Device Comprising A Flat Susceptor Rotating Parallel To A Reference Surface About A Shaft Perpendicular To This Surface*, United States Patent No. 4,860,687, August 29, 1989.

[3] P. M. Frijlink, *Epitaxial Reactor Having A Wall Which Is Protected From Deposits*, United States Patent No. 5,027,746, July 2, 1991.

Chapter 3

External Supports for OMVPE Reactors

The quality of epitaxial layers deposited by an OMVPE reactor is not directly influenced by the external supports for the reactor. Instead, the quality of the external supports determines the safety, the environmental impact, and the operating efficiency of the OMVPE reactor.

In this chapter, the external supports for OMVPE reactors are examined in detail. Specific examples will be used to illustrate possible variations in the external supports and their consequences on the safety, the environmental impact, and the operating efficiency of OMVPE reactors. The specific examples illustrated here are derived from the external supports implemented for "Reactor A" and "Reactor B" (see chapter 2) located at the Microdevices Laboratory (MDL), NASA Jet Propulsion Laboratory (JPL), Pasadena [1]. During the course of this thesis project, extensive interactions with these external supports for the two OMVPE reactors were mandatory and essential. Experiences accrued from these interactions are included here.

3.1 Basic Supports for OMVPE Reactors

OMVPE reactors require comprehensive external supports to meet stringent safety and environmental regulations. One specific arrangement of the external supports for two OMVPE reactors is illustrated in figure 3.1. These basic supports include: building safety monitoring and control station, gas bunker for hazardous gas cylinders, isolated air enclosure, primary exhaust treatment, and secondary exhaust treatment. The dotted lines

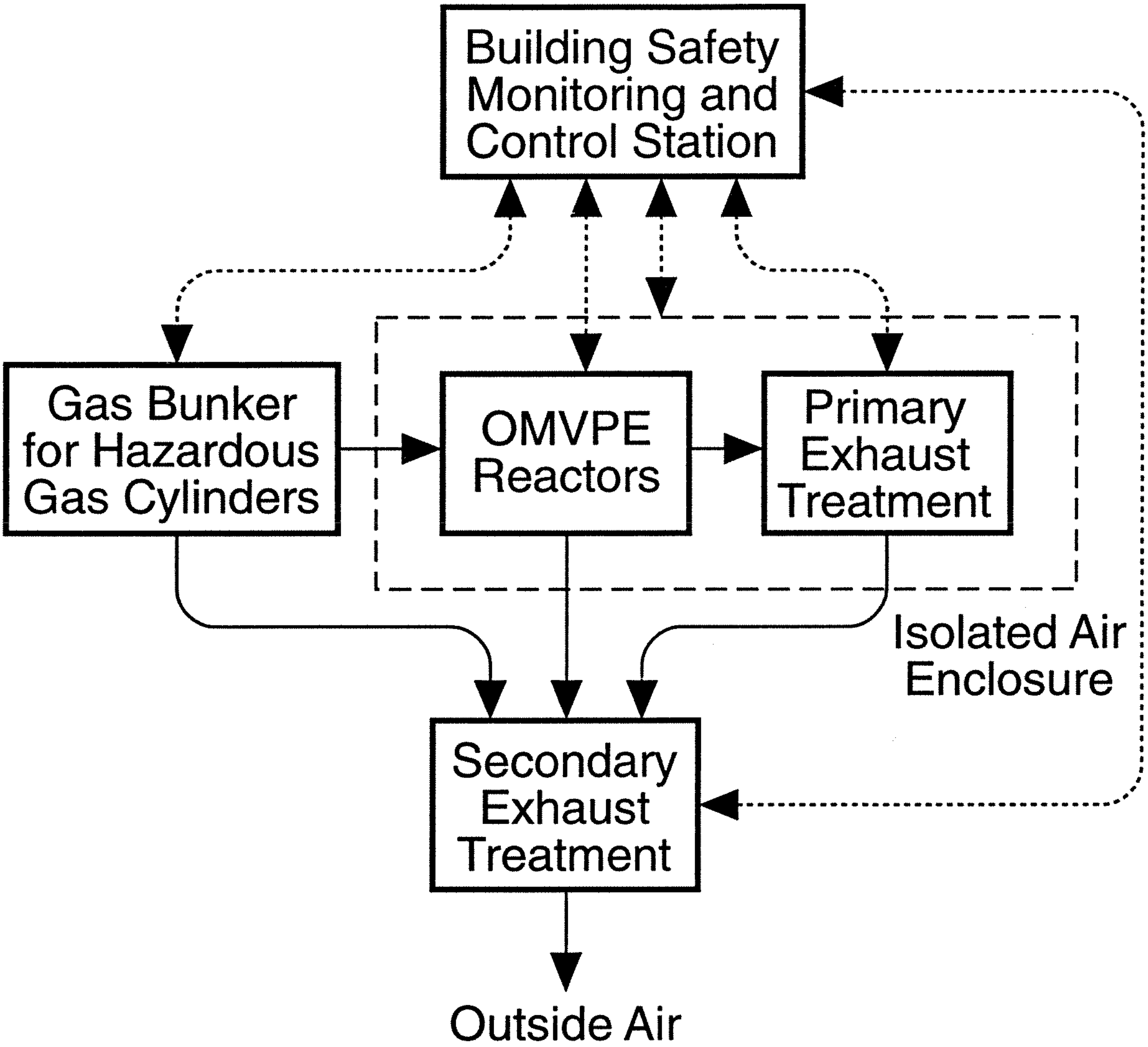

Figure 3.1. Schematic diagram of one specific arrangement of the external supports for two OMVPE reactors.

with arrows indicate paths for electronic control and status lines and hazardous gas sensing lines. The solid lines with arrows indicate paths for gas flow, including process gas flow and exhaust gas flow from the ventilated enclosures. Enclosing the OMVPE reactors and the primary exhaust treatment systems, the box drawn with dashed lines is the isolated air enclosure.

Hazardous gas cylinders, containing gases such as hydrogen (H_2), arsine (AsH_3), phosphine (PH_3), and silane (SiH_4) required for the epitaxial growth of doped GaAs or InP semiconductor materials, are stored in the gas bunker. The gas bunker includes various sensors to monitor for toxic gas leaks and other dangerous conditions. The gases supplied by the gas cylinders are delivered to the OMVPE reactors for epitaxial growths. In addition, the air extracted from the ventilated enclosures containing the hazardous gas cylinders is directed into the secondary exhaust treatment system as a safety precaution.

The hazardous gases delivered from the gas bunker are utilized in the OMVPE reactors for epitaxial growths. The depleted waste gases are sent into the primary exhaust treatment system. The air extracted from the ventilated enclosures containing the OMVPE reactors is directed into the secondary exhaust treatment system as a safety precaution.

The depleted waste gases from the OMVPE reactors are treated by the primary exhaust treatment systems. Residual toxic hydrides and organometallic materials are removed from the gas stream. Any remaining gases are directed into the secondary exhaust treatment system for further treatment.

The OMVPE reactors and the primary exhaust treatment system are located in an isolated air enclosure (room) to shield the rest of the building from potential hazards of the toxic gases.

The secondary exhaust treatment system removes harmful fumes that remain in the gas stream. The gas stream passes through a wet chemical scrubber. The chemical fumes entering the scrubber react with an intensive spray of chemical solutions (pH 9.0-10.0) supplied through a system of nozzles and a recirculation pump. The liquid waste produced is periodically drained as hazardous waste. After passing through the wet chemical scrubber, the gas stream is directed to the outside of the building through a rooftop stack.

The correct operational status of the gas bunker, the isolated air enclosure, the OMVPE reactors, the primary exhaust treatment systems, and the secondary exhaust treatment system are monitored constantly by the building safety monitoring and control station (control room). In addition, sensors are placed in each location to detect dangerous conditions such as toxic gas leaks or fire. The safety equipment in the control station monitors these sensors constantly. If potentially dangerous conditions are detected, the gas cylinders in the gas bunker are shutdown automatically by the safety control equipment, and other automatic responses would also take place to prevent further problems.

3.2 Safety Monitoring and Control Station

The safety monitoring and control station is an extremely important external support for OMVPE reactors. Extremely hazardous and toxic gases are utilized within OMVPE reactors. High temperatures and large electrical currents are also present in OMVPE reactors. The safety monitoring and control station provides constant monitoring for toxic/pyrophoric gases, combustible gases, oxygen deficiency, seismic activity, manual emergency push button activation, fluid leaks, and fire/smoke. Additionally, the control station also verifies the proper operational status of the exhaust ventilation and treatment systems, fire-suppression systems, gas cabinets for hazardous gases at the gas bunker, cooling water system, and door alarms for gas bunker access and emergency-only exits in the building.

The toxic/pyrophoric gases are detected by using Chemcassettes®, which are chemically impregnated dry reaction substrates (paper) used to detect and measure specific toxic gases. The gases are drawn through the dry reaction substrate by suction from a vacuum pump. If any toxic/pyrophoric gases are present, the dry reaction substrate changes color from normally white to brown. The color change is detected and measured by a built-in optical system and displayed in terms of ppb (parts per billion) or ppm (parts per million) at the readout. For rooms where the operators occupy, the level for audio alarm is set at 0.5 TLV and the level for building evacuation is set at 1 TLV. For inside ventilated enclosures of equipment, the level for audio alarm is set at 1 TLV and the level for building evacuation is set at 10 TLV. TLV is the threshold limit value determined for each particular substance at a concentration where workers may be exposed to day after day without any adverse effects. In the event of a building evacuation, caused either by toxic-gas detection or by manual activation of emergency push button, the gas bunker is shutdown, the fire department is notified, and the OMVPE reactor room is switched from positive room pressure to negative room pressure as compared to the rest of the building.

The presence of combustible gases or oxygen deficiency are detected by using sensors containing catalytically-aided platinum-wire bridge. Exposing the wire bridge to specific gases changes the electrical potential across the wire bridge according to gas concentration. The changes in electrical potential are detected and measured by an electrical amplifier and displayed in terms of concentration in percent at the readout. For combustible gases, the level for audio alarm is set at 0.2 LEL and the level for building evacuation is set at 0.5 LEL. LEL is the lower explosive limit, the concentration of a substance in air that is capable of causing an explosion or flash. For oxygen deficiency, the level for audio alarm is set at 19.5% O_2 and the level for building evacuation is set at 16.5% O_2.

Seismic activity is detected by an accelerometer mounted in direct contact with the foundation of the building. Ground accelerations that exceed a set limit will cause a complete shutdown of the gas bunker.

Fluid leaks are monitored by electrical electrodes placed within various dry recesses in the floor. Fluid leaks significant enough to flow into the dry recesses will cause a flow of electrical current between the electrodes and cause an alarm condition.

Fire, or prelude to fire including smoke, is detected by an incipient fire detection system. This system detects the pre-combustion submicron particles that are generated before an actual fire. When the concentration of pre-combustion particles reaches a first level, an audio alarm is initiated. When the concentration of pre-combustion particles reaches a higher second level, building evacuation commences.

This particular arrangement of safety monitoring allows centralized control and maintenance of the building safety equipments. There are drawbacks, however. The centralized location of the toxic-gas monitoring equipment results in long lag times before an actual toxic gas leak is detected, because there are long tubings between the monitored locations and the monitoring equipment. In addition, the toxic gas monitoring equipment is time-shared between different locations which causes further delays.

An improved arrangement would be to locate additional toxic gas monitoring equipment at the individual locations. The local monitoring equipment would be much smaller and less expensive. They would be electrically connected to the central control station, resulting in much faster responses while providing local audio alarm capabilities for immediate warning. The early warning may allow operators to avert complete building evacuation by reacting promptly to the initial local alarm condition.

3.3 Gas Bunker for Hazardous Gas Cylinders

Hazardous gas cylinders, containing gases such as hydrogen (H_2), arsine (AsH_3), phosphine (PH_3), and silane (SiH_4), are stored in a gas bunker away from the main building. A schematic diagram of the gas bunker is shown in figure 3.2. The entire structure of the gas bunker is constructed to be earthquake-resistant and is constructed from steel-reenforced concrete. The two entrances into the gas bunker are protected

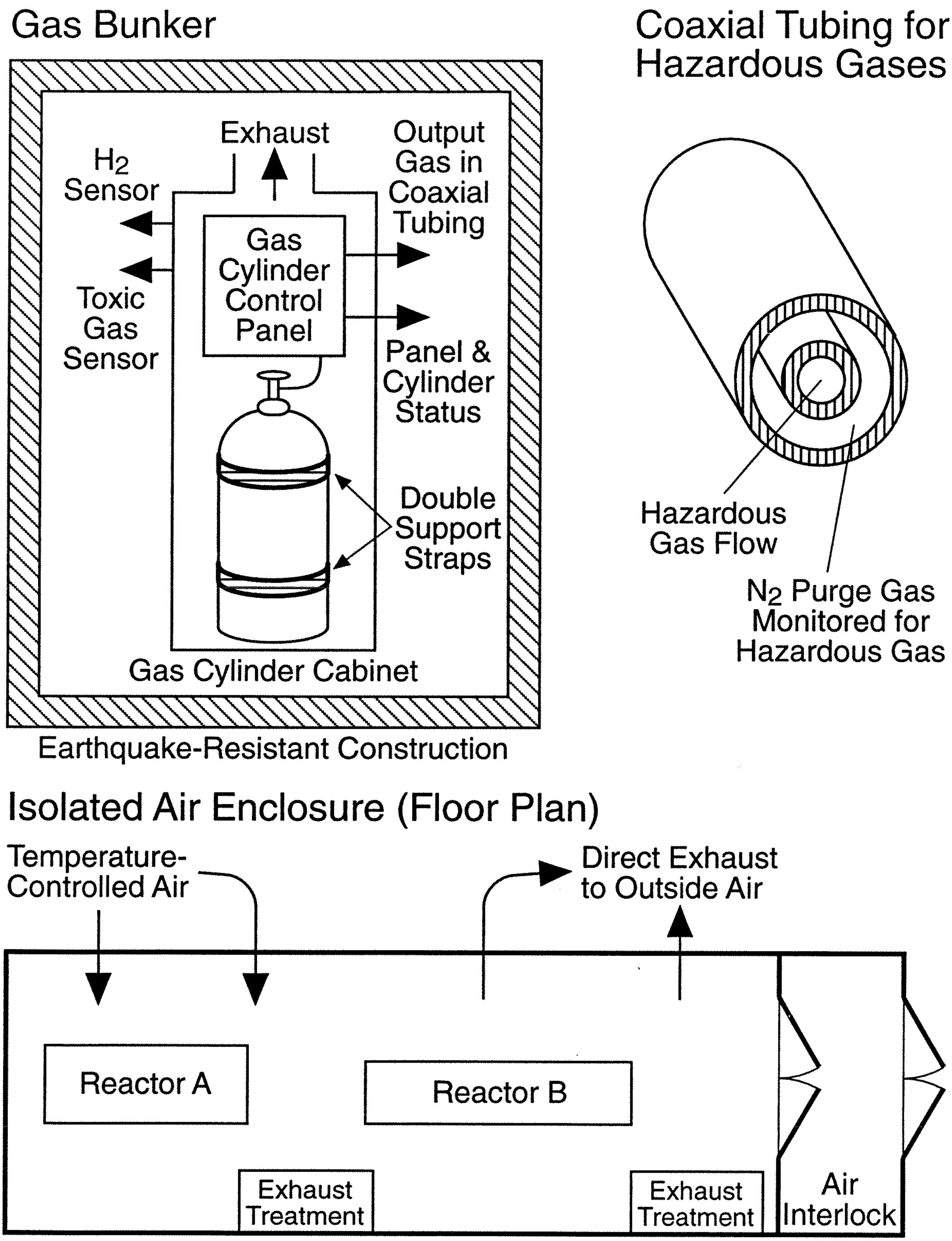

Figure 3.2. *Top left*: schematic diagram of the gas bunker for hazardous gas cylinders. *Top right*: schematic illustration of the coaxial tubing for delivery of hazardous gases. *Bottom*: schematic illustration of the isolated air enclosure for two OMVPE reactors.

from vehicle collisions by thick barriers constructed from steel-reenforced concrete. The two entrances are secured by two security doors. The doors are constructed of closely-spaced steel bars to allow air ventilation in the gas bunker to prevent entrapment of toxic gases. The two doors at the two entrances are locked at all times except during service operations. The two doors are monitored at the control station for any unauthorized accesses.

Inside the gas bunker, there are many gas cylinder cabinets, one of which is shown in figure 3.2. The actual gas cylinder is fastened to the gas cylinder cabinet using two support straps. The two straps are necessary to prevent the toppling of the gas cylinder during an earthquake. If the gas cylinder is secured using only one strap, it is possible for the gas cylinder to slide on the ground and slip out of the single strap during an earthquake. The gas cylinder cabinets are anchored to the floor and to the walls of the gas bunker. The gas cylinder cabinets are ventilated through the building exhaust system. The air extracted from the ventilated gas cylinder cabinets is directed into the secondary exhaust treatment system as a safety precaution.

The gas cylinder is connected to a gas cylinder control panel. This computer-controlled panel allows the automated purging, testing, and evacuating of the tubing connections when gas cylinders are replaced or service operations are performed. The panel is also controlled from the control station, allowing for the remote shutdown of the gas cylinders. Anomalies in the gas delivery system such as excess flow or excess delivery pressure are detected by the panel and indicated in the control station. The specific gas cylinder is also shutdown in such events.

The hazardous gas from the gas cylinder is delivered to the OMVPE reactors through coaxial tubings, as shown in figure 3.2. The inner tubing carries the hazardous gas flow. A flow of N_2 purge gas is maintained between the inner and the outer tubing. At the gas bunker, the N_2 purge gas flow is sampled for the presence of toxic gases. If toxic gases are detected, the gas bunker is shutdown.

Various sensors are placed inside and outside the gas cylinder cabinets to monitor for toxic gas leaks and other dangerous conditions. Toxic gas monitoring points are placed inside the gas cabinets to detect any toxic gas leaks. H_2 sensors are additionally placed inside the gas cylinder cabinets for gas cylinders containing hydrogen.

Building a separate gas bunker away from the main building isolates the large depot of hazardous gases, thereby reducing the risk of exposing the occupants of the main building to any major toxic gas releases. However, the separate gas bunker also makes it more difficult to adjust or check parameters for each gas cylinder, such as adjusting the delivery pressure of the source gas or checking the amount of source gas available from the gas cylinder. Currently, these adjustments or checks can only be made in the gas bunker. In addition, the users of these source gases do not know if the gas cylinder is shutdown or not, since there are no local readouts indicating gas bunker status.

For a gas bunker to function more efficiently and effectively, it is necessary to electronically monitor all of these additional parameters and distribute this electronic signal to local readouts located at the equipments utilizing these source gases. It would be even better if these additional parameters can be adjusted remotely without having to enter the gas bunker.

3.4 Isolated Air Enclosure

As shown in figure 3.2, the OMVPE reactors and the primary exhaust treatment systems are completely enclosed in an isolated air enclosure. Two sets of double doors that form an air interlock are the only entrance to the isolated air enclosure. The doors open outward for ease of escape during emergencies.

As shown in the diagram, temperature-controlled air is pumped into the isolated air enclosure through one path. Some of the air exits through the ventilated enclosures of the OMVPE reactors and the primary exhaust treatment systems into the secondary exhaust treatment system. The remaining air exits directly to the outside of the building through another path. In order to prevent potentially contaminated air from escaping through the doors and other openings, the isolated air enclosure is maintained at a negative pressure as compared to the rest of the building when a toxic gas leak is detected by the toxic-gas monitoring equipment. Normally, the isolated air enclosure is maintained at a slightly positive pressure as compared to the rest of the building to allow for efficient operation of the exhaust ventilation system.

The incoming air must be maintained at a constant temperature for the proper operation of the OMVPE reactors. Since air is not recycled in the isolated air enclosure, the ambient temperature measured at the OMVPE reactors is substantially the same as the temperature of the incoming air. Fluctuations in the temperature of the incoming air would disrupt the temperature-controlled baths for the OM sources and shift the operating points of the mass-flow and pressure controllers. Unwanted shifts in the material composition of epitaxial layers would be the result. For the proper operation of the OMVPE reactors, it is therefore extremely important to maintain a constant temperature in the incoming air.

3.5 Primary Exhaust Treatment

The depleted waste gases from the OMVPE reactors are treated by the primary exhaust treatment systems. Residual hydride gases and organometallic materials are removed from the gas stream. Any remaining gases are directed into the secondary exhaust treatment system for further treatment.

There are two primary exhaust treatment systems illustrated in figure 3.3. One system is the CDO unit, an acronym for the combustion-decomposition-oxidation unit. In this system, the depleted waste gases from the OMVPE reactors are mixed with a gas containing oxygen and then passed through a chamber with heating coils heated to 800°C. The waste gases from the OMVPE reactors decompose and oxidize in the presence of high temperature and oxygen. The treated exhaust gas is directed into the

Primary Exhaust Treatments:

A) C.D.O.: Combustion-Decomposition-Oxidation Unit

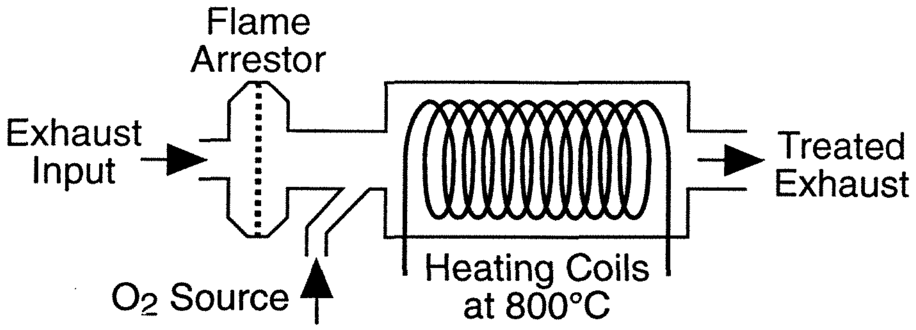

B) AIXTOX Scrubbing System

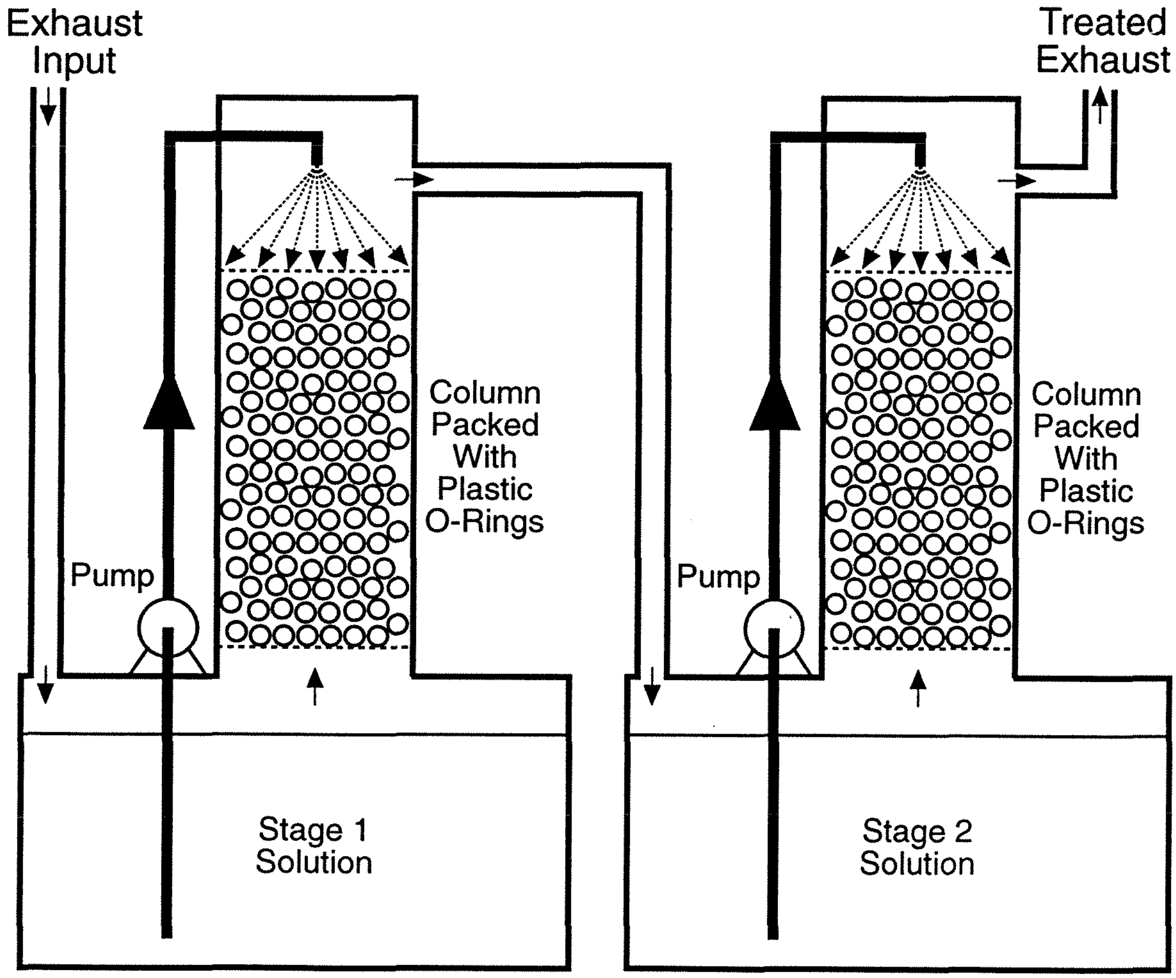

Figure 3.3. Schematic illustration of two different types of primary exhaust treatment systems.

secondary exhaust treatment system. A flame arrestor is installed on the inlet side of the CDO unit to prevent combustion from traveling backwards into the exhaust tubing from the OMVPE reactors.

The CDO unit suffers from extremely serious drawbacks. The unit is not enclosed in a self-contained ventilated enclosure. If any gas leaks occur in the unit, the gas would permeate throughout the whole room. Since the CDO chamber is at a high temperature, there is significant risk for explosions if flow surges occurred in the oxygen source or in the waste gases which may contain large amounts of hydrogen. The combustion by-products, composed of oxides of arsenic and phosphorous, are still highly toxic and corrosive. There is no effective way to dispose of these combustion by-products except to leave them where they remain in the exhaust ducts. When the exhaust ducts are clogged, then the ducts have to be replaced.

There were so many problems and drawbacks to the CDO units that the CDO units installed initially for the OMVPE reactors were replaced by the AIXTOX® scrubbing system [2,3], also illustrated in figure 3.3.

In an AIXTOX® scrubbing system, there are typically two stages, each containing different liquid chemical solutions. Within each stage, a pump for corrosive liquids pulls the chemical solution from a large reservoir (90 liter capacity) and force the solution through nozzles to form a fine spray of droplets that trickle down through a column packed with plastic o-rings. The plastic o-rings enhance the total available surface for chemical reactions.

In the AIXTOX® scrubbing system, the depleted waste gases from the OMVPE reactors flow through stage 1 and react with an acidic solution of bromate or iodate salts. Hydride gases such as AsH_3 or PH_3 are oxidized and converted into water-soluble acids. These water-soluble acids remain dissolved in the chemical solution of stage 1. In this chemical reaction, free molecules of bromine or iodine are also formed. The bromine or iodine molecules are removed in stage 2 by a basic solution that reacts with the free bromine or iodine and forms water-soluble bromate or iodate salts. The treated exhaust gas, containing only hydrogen, is diluted to concentration levels much below the lower explosive limit by the air flowing through the ventilated enclosure containing the scrubbing system. The treated exhaust is directed into the secondary exhaust treatment system as a safety precaution.

When the chemical solution in stage 1 is nearly depleted, trace amounts of hydride gases appear in the treated exhaust and is detected by toxic-gas monitoring equipment to indicate the depletion of the chemical solutions. The chemical solutions would be drained and replaced with new solutions. The depleted chemical solutions, containing water-soluble forms of arsenic and phosphorous, are easily drained and disposed of.

The AIXTOX® scrubbing systems perform extremely well as the primary exhaust treatment systems for the two OMVPE reactors. The only maintenance required, besides the routine drain and refill of the chemical solutions, is the periodic checks for leaks and the replacements of rubber seals to ensure liquid-tight and air-tight systems.

Bibliography

[1] C. Matus, *Microdevices Laboratory Safety Manual: Operations, Policies, and Procedures Plan*, NASA Jet Propulsion Laboratory, September 1992.

[2] W. Fabian, H. Roehle, and P. Wolfram, *Method Of Removing Noxious Substances From Gases*, United States Patent No. 4,612,174, September 16, 1986.

[3] Product brochures for *AIXTOX Scrubbing System*, AIXTRON GmbH, Aachen, Germany, 1990.

Chapter 4

Selective Epitaxy of GaAs, AlGaAs, and InGaAs

Many device structures benefit from the ability to selectively deposit epitaxial materials. Through the use of a masking material, such as silicon nitride (Si_3N_4) or silicon dioxide (SiO_2), on the substrate surface, patterns generated through standard lithographic procedures can be used to define regions for selective deposition.

Highly selective growth can be achieved through the use of organometallic (OM) sources which contain halogens, such as diethylgallium chloride $(C_2H_5)_2GaCl$ (DEGaCl), diethylaluminum chloride $(C_2H_5)_2AlCl$ (DEAlCl), and dimethylindium chloride $(CH_3)_2InCl$ (DMInCl). These compounds decompose, most probably, to the volatile mono-halogenated species, for example gallium chloride GaCl, and also generate hydrogen chloride HCl in the gas phase as a reaction by-product.

Experimental results on the morphology and growth behavior of GaAs, $Al_xGa_{1-x}As$ and $In_xGa_{1-x}As$ using this technique are presented. The single-layer materials and selectively grown heterostructures produced by this technique have been characterized. The interface between the selectively grown material and the underlying substrate was investigated and the conditions for achieving high-quality defect-free interfaces were determined.

4.1 Introduction to Selective Epitaxy

The drive to smaller device dimensions has led to the development of epitaxial growth techniques which controllably deposit material on a nanometer scale. Thin layer structures can be produced in which the local band structure is modified by changes in the material composition along the growth direction. As device dimensions become smaller, lateral control over the composition and band structure is also needed. Such laterally defined and controlled growth of semiconductor materials require new growth techniques and growth chemistries. Selective epitaxy has been developed, in many forms, to address some of these new technological challenges. Laterally controlled growth has been investigated in all the major methods of epitaxial growth [1-18]. The term selective epitaxy has been used to refer to several forms of laterally controlled growth. There are three current research areas which use the term selective epitaxy:

(1) The first area is conformal deposition on a partially masked substrate [19]. In this case, the deposited material grows as an epitaxial single-crystal only within the mask openings to the substrate. Polycrystalline deposition occurs on the masking material and the edge morphology of the epitaxial regions typically exhibit enhanced growth rates.

(2) Growth on non-masked, patterned substrates, also referred to as selective epitaxy, is a second area of active research. The substrate patterning is accomplished prior to growth through chemical or dry etching and standard lithographic procedures. Growth on such patterned substrates can exhibit lateral variations in the composition and growth rate [20]. These lateral variations result from selective adsorption and surface diffusion of growth precursors. Certain crystallographic surfaces will preferentially incorporate a particular growth precursor, locally altering the material characteristics. This technique has been widely investigated for the formation of advanced optoelectronic structures within a single growth procedure.

(3) The last form of selective epitaxy refers to the local preferential growth of epitaxial materials without extraneous or polycrystalline growth on a masking material. External energy sources, such as a focussed laser, have been used to locally heat the substrate surface to promote the thermally-driven decomposition reactions [21]. This form of selective epitaxy allows the 'writing' of epitaxial structures on the substrate surface. The

lateral definition of the selective epitaxy regions is limited by the wavelength of the laser and the thermal diffusion characteristics of the substrate material. This last definition of selective epitaxy can be extended to truly selective growth with masked and patterned substrates. Selective epitaxy with no deposition on the masked areas is particularly applicable to device applications where the polycrystalline deposits and variable edge morphologies are potentially destructive to device performance.

This chapter will present results on this third form of selective epitaxy. As illustrated in figure 4.1, epitaxial materials such as GaAs or AlGaAs are deposited within openings of a masking material, such as silicon nitride, on a substrate. For device fabrication, one distinct advantage of selective epitaxy is the efficient injection of current carriers into the active region of the device. In addition to defining the active region of the device, the dielectric layer also performs well as a current focusing element that funnels the injected carriers through the active region of the device. When selective epitaxy is applied to semiconductor lasers, the threshold current for lasing could be reduced significantly.

Selective epitaxy of GaAs, $Al_xGa_{1-x}As$, and $In_xGa_{1-x}As$ were demonstrated using alternative halogen-based organometallic precursors such as DEGaCl and DEAlCl [22]. The use of halogen-based organometallic compounds can result in the epitaxial growth of compound semiconductors within openings of a dielectric-coated substrate [13,22]. No deposition will occur on the masking material under appropriate conditions unlike the use of conventional OMVPE precursors, such as trimethylgallium (TMGa), trimethylaluminum (TMAl), and trimethylindium (TMIn).

GaAs growth process using conventional OMVPE precursors is illustrated in figure 4.2 [23]. Selective epitaxy using this process results in polycrystalline deposits over the masked area in addition to deposition occurring within the openings of the masking material. The poor selectivity is the result of the surface reaction, where no mechanism exists for the Ga atom to return to the gas phase once nucleation has taken place over the masked area.

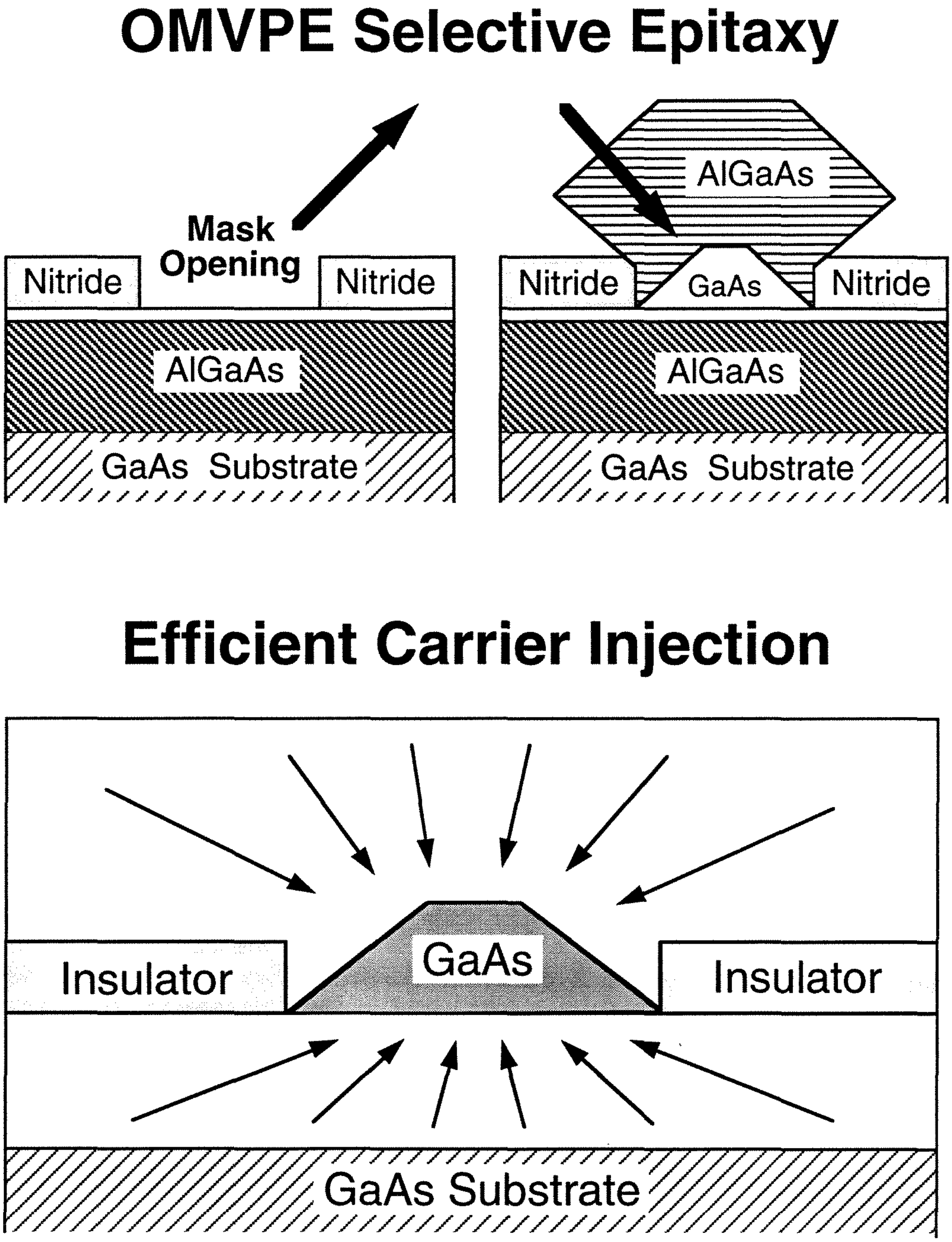

Figure 4.1. *Top*: schematic illustration of epitaxial deposition within mask openings by OMVPE selective epitaxy. *Bottom*: efficient electrical-carrier injection is a distinct advantage of device fabrication by selective epitaxy.

Gallium Arsenide Growth Process in Conventional OMVPE

$(CH_3)_3Ga$ = trimethylgallium
AsH_3 = arsine

Complete Reaction

$$(CH_3)_3Ga + AsH_3 \Rightarrow GaAs + 3\,CH_4$$

Gas-Phase Reaction

$$(CH_3)_3Ga \Rightarrow CH_3Ga + 2\,CH_3$$
$$AsH_3 \Rightarrow AsH + 2\,H$$
$$2\,CH_3 + 2\,H \Rightarrow 2\,CH_4$$

Surface Reaction

$$CH_3Ga + AsH \Rightarrow GaAs + CH_4$$

Surface reaction is **irreversible**
Ga is not volatile

Figure 4.2. Proposed chemical-reaction steps in GaAs growth process using conventional OMVPE growth precursors trimethylgallium and arsine.

GaAs growth process using alternative halogen-based precursors is illustrated in figure 4.3 [13]. In contrast with the conventional process, this process results in complete selectivity under appropriate conditions. The surface reaction is reversible. If GaAs nucleated over the masked area, the surface reaction would reverse under the appropriate growth condition and convert the nucleated GaAs, in the presence of HCl, back into gas phase as As and GaCl.

The growth process using alternative halogen-based precursors has the advantage of being compatible with conventional photolithographic and electron-beam lithographic practices allowing for the selective epitaxy of sub-micron structures. The properties of these materials grown on patterned masked substrates will be presented. The results indicate that these precursors provide a chemical route to achieve selective epitaxy within conventional OMVPE reactors under growth conditions compatible with the deposition of high-purity and high-quality epitaxial structures.

4.2 Substrate Preparation and Growth Conditions

Selective epitaxy was studied using the chlorine-based organometallic compounds DEGaCl and *in situ* formed DMInCl. DEGaCl was supplied in a standard organometallic-source-bubbler arrangement. The low vapor pressure of this source (0.13 Torr at 40°C for DEGaCl) may require the use of elevated source temperatures and heated lines in certain OMVPE reactors. For the initial study, the DEGaCl source was held at ~40°C and used heated source lines. For subsequent studies, the DEGaCl source was held at ~17°C, slightly below room temperature. DMInCl has a prohibitively low vapor pressure (~0.03 Torr at 40°C), preventing its direct use in a conventional bubbler. $In_xGa_{1-x}As$-based growths are carried out using DEGaCl and TMIn. In this case, DMInCl is probably generated *in situ* in the OMVPE reactor through the reaction of DEGaCl and TMIn.

Gallium Arsenide Growth Process in Selective Epitaxy

$(C_2H_5)_2GaCl$ = diethylgallium chloride
AsH_3 = arsine

Complete Reaction

$(C_2H_5)_2GaCl + AsH_3 => GaAs + HCl + 2\ C_2H_6$

Gas-Phase Reaction

$(C_2H_5)_2GaCl => GaCl + 2\ C_2H_5$
$AsH_3 => AsH + 2\ H$
$2\ C_2H_5 + 2\ H => 2\ C_2H_6$

Surface Reaction

$GaCl + AsH <=> GaAs + HCl$

Surface reaction is **reversible**
As, GaCl are volatile

Figure 4.3. Proposed chemical-reaction steps in selective GaAs growth process using halogenated-organometallic precursor diethylgallium chloride and arsine.

The OMVPE reactors utilized for these experiments are conventional horizontal reactors as described in chapter 2. Deposition chamber pressure was maintained between 100 and 200 mBar. Growth temperatures within the range 600-800°C were investigated with most of the growths undertaken at 650 or 700°C. Substrates of semi-insulating and n-type GaAs were used in the studies. The studies of the selectively grown GaAs used substrates consisting of 2 μm layer of $Al_{0.3}Ga_{0.7}As$ capped by 10-20 nm layer of GaAs to prevent oxidation of the $Al_{0.3}Ga_{0.7}As$ layer. The luminescence from the GaAs substrate is prevented from contributing to the luminescence signal by the $Al_{0.3}Ga_{0.7}As$ buffer layer. The patterned substrates were masked with Si_3N_4 or SiO_2, deposited by plasma-enhanced chemical-vapor deposition (PECVD). Most studies used Si_3N_4 masked substrates. The openings in the mask were formed by conventional photolithographic techniques. Micron-sized openings were defined through reactive-ion etching (RIE) using CF_4 plasma. In larger structures, the masking material was etched using buffered HF solutions. The patterned substrates were cleaned in organic solvents to remove the resist materials. An intermediate cleaning step of RIE using O_2 plasma was also applied to ensure the complete removal of resist materials. Prior to loading into the OMVPE reactor, the samples were dipped in concentrated HCl for 20-60 seconds in order to remove the surface oxides, and then rinsed in deionized water. This step was found to be crucial in achieving high-quality interfaces between the substrate and the selectively grown material. The samples were annealed at the growth temperature under a H_2/AsH_3 ambient for 5-10 minutes prior to the beginning of the regrowth step. The basic steps in the fabrication procedure are illustrated in figure 4.4.

The selectively grown materials were characterized by scanning electron microscopy (SEM) and optical microscopy in order to evaluate surface and edge morphology. The luminescence properties of some selectively grown heterostructures were obtained in a modified SEM with room and low temperature (77°K) cathodoluminescence (CL)

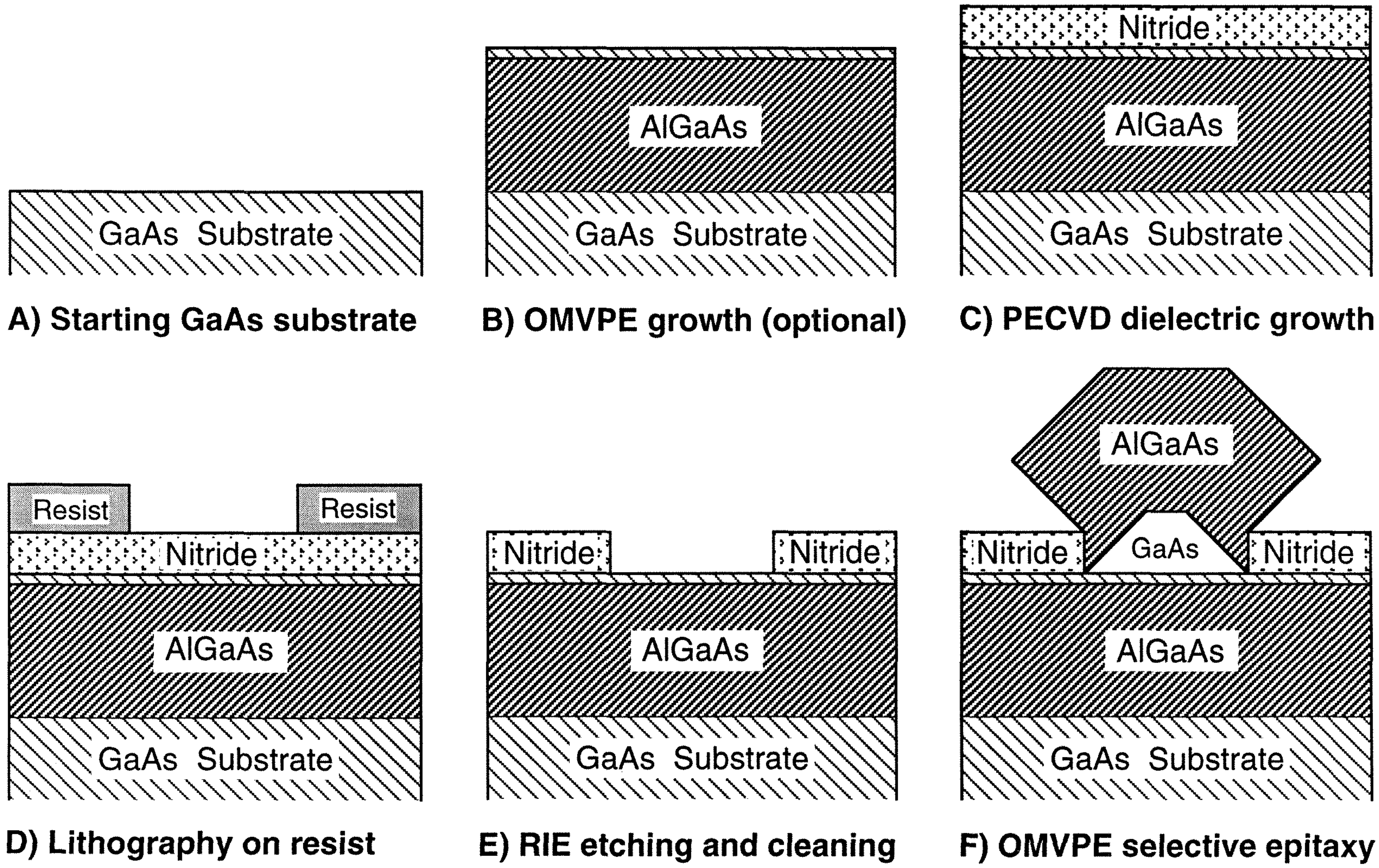

Figure 4.4. Schematic illustration of the basic fabrication procedures for selective epitaxy.

collection system [24]. Cathodoluminescence was used to determine the alloy composition of the ternary growth of AlGaAs.

4.3 Selective Epitaxy on Patterned Substrates

4.3.1 GaAs Selective Epitaxy

The selective epitaxy of GaAs using DEGaCl has been previously reported [13]. The DEGaCl-based GaAs growth is extremely selective with respect to all of the conventionally-deposited dielectric materials Si_3N_4, SiO_2, and $SiON_x$. The range of growth temperatures over which complete selectivity is obtained extends over the entire investigated range of 600-800°C.

The morphology of the GaAs selective epitaxy is dominated by the appearance of the slow-growth crystallographic planes noted in the inorganic-based growth of GaAs [25]. These crystallographic planes are predominantly the (110) and mixed (111) types of planes. The appearance of a particular plane is dependent on the growth temperature, the growth pressure, the growth rate, and the orientation of the mask opening with respect to the substrate crystallographic orientation.

Cross-sectional views of selectively grown GaAs stripes of various orientations are shown in figures 4.5, 4.6, and 4.7. The stripes shown in figures 4.5, 4.6, and 4.7 are oriented along the $[01\overline{1}]$, [011], and [010] directions respectively, where the vertical direction is [100]. Each figure contains backscattered-electron images of various stripes from the same sample. Stripes of different orientations show different facetting characteristics. The thicknesses of the GaAs stripes are reduced as the widths of the initial mask openings are increased. No epitaxial material was deposited over the dielectric masking material outside of the openings.

The selectively grown regions are free of extended defects as characterized by transmission electron microscopy (TEM) [22]. The initial growth interface cannot be resolved using TEM, unlike TMGa-based GaAs layers where the initial growth interface

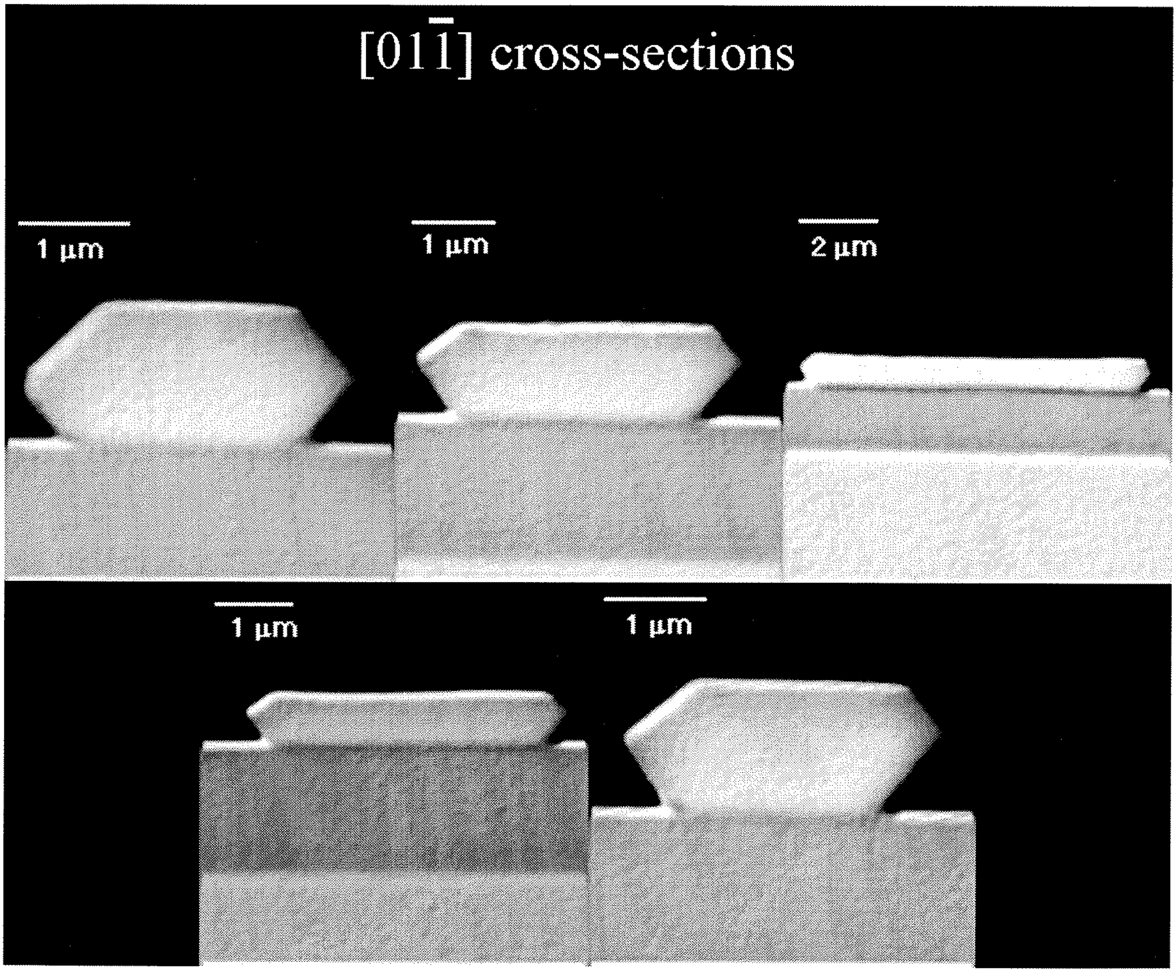

Figure 4.5. Cross-sectional backscattered-electron images of selectively grown GaAs stripes oriented along the [01$\bar{1}$] crystallographic direction.

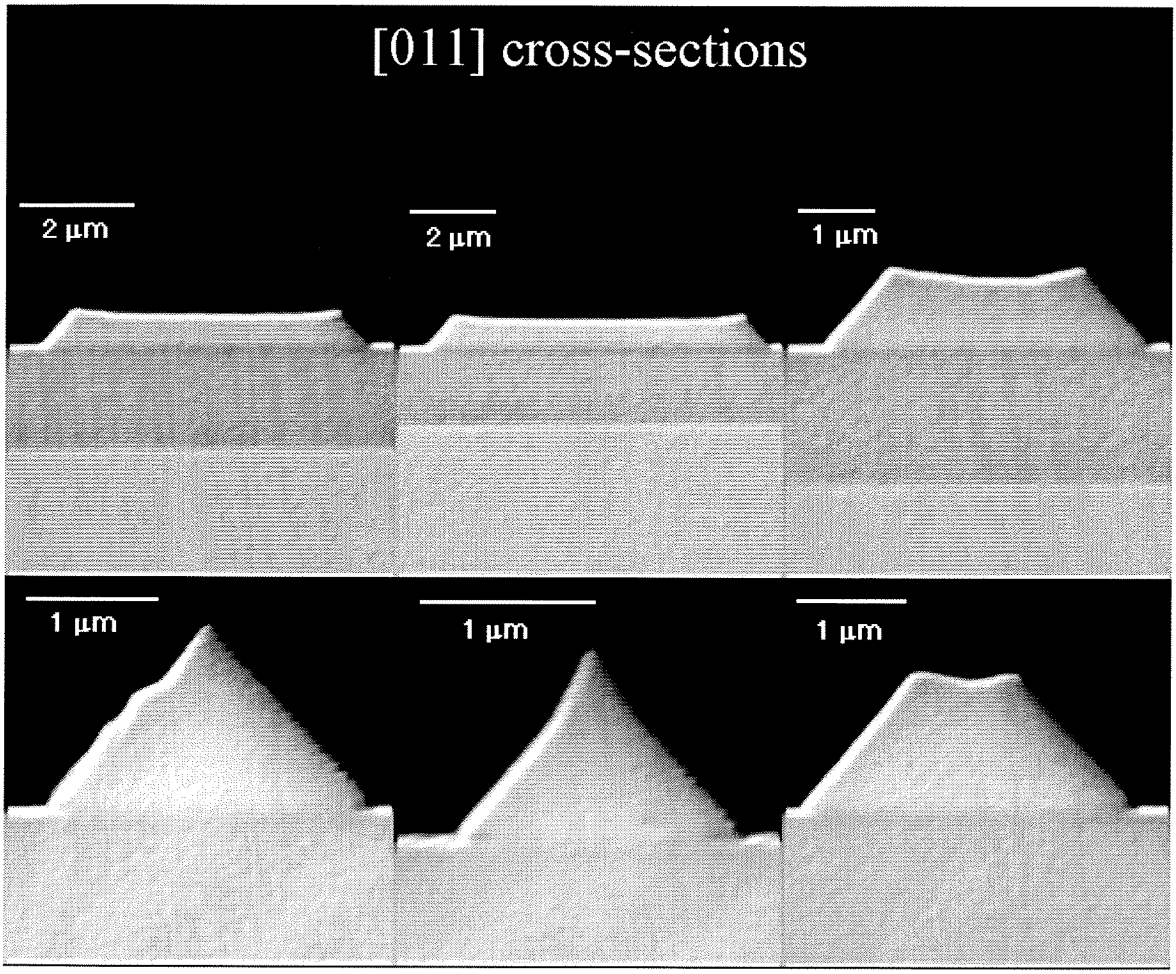

Figure 4.6. Cross-sectional backscattered-electron images of selectively grown GaAs stripes oriented along the [011] crystallographic direction.

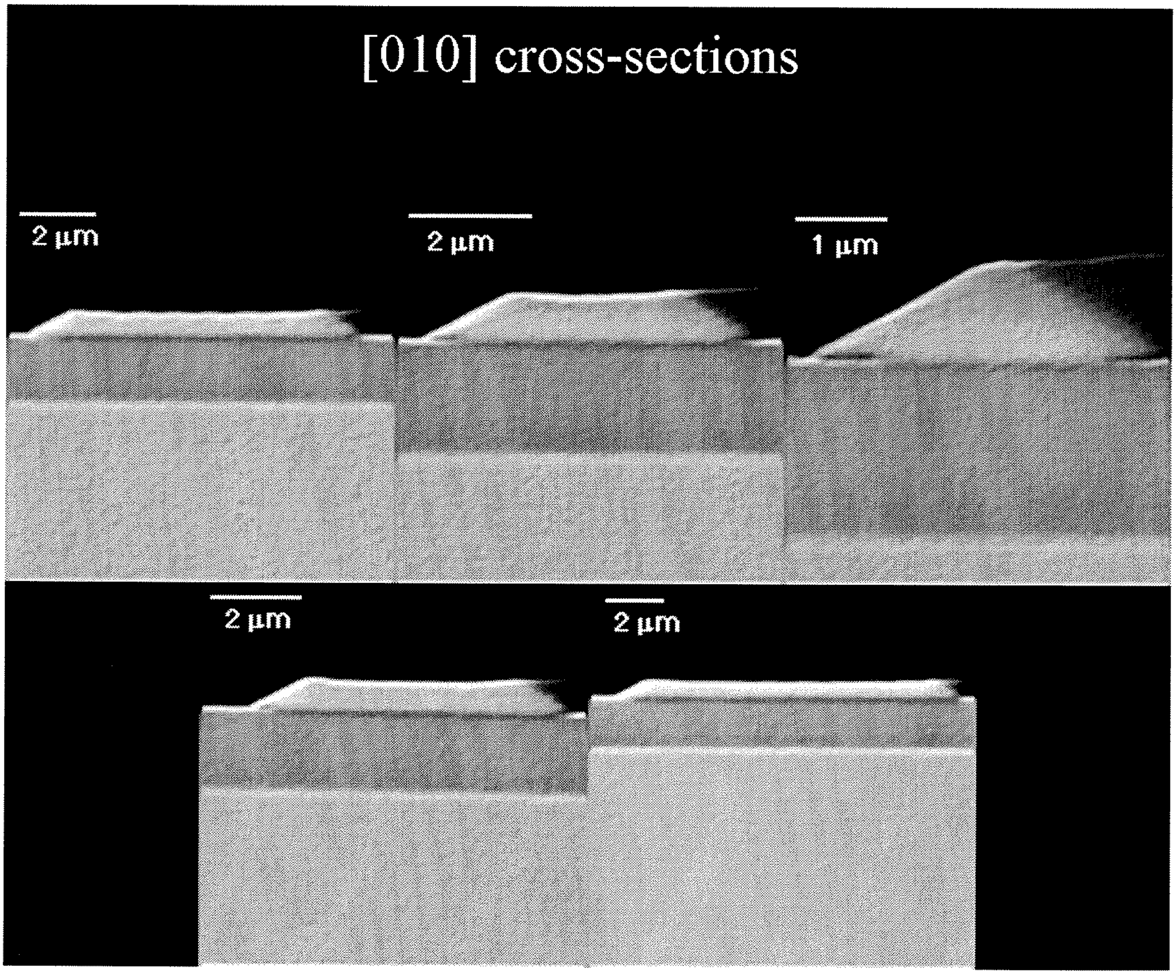

Figure 4.7. Cross-sectional backscattered-electron images of selectively grown GaAs stripes oriented along the [010] crystallographic direction.

can be delineated clearly. This high-quality interface can be produced without measurable chemical or structural defects.

The complete selectivity seen in the DEGaCl-based growth of GaAs has been attributed to the *in situ* formation of GaCl as a result of the decomposition of DEGaCl. The growth mechanism near the substrate surface should parallel that of the inorganic-based GaAs growth [25]. In that case, the selectivity arises from the low local supersaturation and the lack of adsorption of GaCl on the dielectric masking material.

4.3.2 $Al_xGa_{1-x}As$ Selective Epitaxy

The selective epitaxy of $Al_xGa_{1-x}As$ was also undertaken using growth conditions similar to those employed in the studies of GaAs selective epitaxy, except for the use of TMAl. The addition of DEGaCl during the growth of $Al_xGa_{1-x}As$ results in the selective deposition of $Al_xGa_{1-x}As$ over a range of alloy compositions and growth temperatures. The selectivity, however, also depends on the density and pattern of openings in the masking material. $Al_xGa_{1-x}As$ selectivity was not extensively studied below 700°C growth temperature.

The data indicate that layers with low Al content grown at high temperatures exhibit good selectivity. The overall chlorine to metal (Al and Ga) ratio in the gas phase is increased under these growth conditions. Selective GaAs growth will always occur under these growth conditions and will generate HCl. This HCl, in turn, prevents the formation of AlAs deposits on the masked regions, thereby improving selectivity. Higher growth temperatures decrease the overall supersaturation of the growth ambient and reduce the overall driving force for deposition and thus improving selectivity.

The morphology of the selectively grown $Al_xGa_{1-x}As$ regions is similar to that of the selectively grown GaAs. The features are once again dominated by slow-growth crystallographic planes. There is a tendency to have several planes appear along the growth edge with a shorter spatial extent to each facet face. This tendency of AlGaAs growth is exploited effectively in the growth technique to be described in chapter 7.

4.3.3 $In_xGa_{1-x}As$ Selective Epitaxy

The selective epitaxy of $In_xGa_{1-x}As$ is similar to that of $Al_xGa_{1-x}As$, except for the substitution of TMAl with TMIn. There is a limited range of growth temperature and In composition over which complete selectivity is achieved. Low In concentrations and higher growth temperatures result in complete selectivity [22]. The higher In content layers grown at 600 and 700°C do not show complete selectivity. The morphology of the selectively grown $In_xGa_{1-x}As$ regions is also similar to that of the selectively grown GaAs. The features are once again dominated by slow-growth crystallographic planes.

The reduced selectivity seen in the $In_xGa_{1-x}As$ materials is attributed to the low chlorine to metal (In and Ga) ratio employed here. The lower chlorine to metal ratio in the gas phase during $In_xGa_{1-x}As$ growth, compared to the binary growth of GaAs, leads to higher supersaturation. Since TMIn and DEGaCl are used in this study, the chlorine to metal ratio is always less than 1 whereas DEGaCl growth of GaAs has a ratio of 1. The addition of HCl to the gas phase should reduce the overall growth supersaturation and lead to greater selectivity for $In_xGa_{1-x}As$ selective epitaxy [18].

4.4 Growth Uniformity during Selective Epitaxy

4.4.1 Global Uniformity

The uniformity of material deposition is an important parameter for any epitaxial-growth technique. Uniformity during selective epitaxy can be viewed from both a global (i.e. whole wafer) and local perspective. The utility of the deposition process for device applications is affected by uniformity on both length scales. The global uniformity during both selective epitaxy and conventional growth is affected by the thermal-fluid environment within the deposition chamber of the OMVPE reactor. As such, the uniformity of deposition will be influenced by the total flow rate, the thermal boundary conditions at the deposition-chamber walls, the chamber pressure, and the chamber geometry. An additional complicating factor associated with the use of DEGaCl is the introduction of chlorine which may act as an etchant under certain conditions.

The global uniformity was investigated for the growth of GaAs under two different conditions, as shown in figure 4.8. The growth temperature was 700°C in both cases. TMGa and DEGaCl were used in separate growth runs on non-patterned substrates. The uniformity on masked and patterned substrates using DEGaCl was also determined. The main variable changed between these runs was the total flow rate into the deposition chamber. The uniformity of the TMGa-based growth at 7.5 slm (standard liters per minute) total flow is dominated by a monotonic change in the growth rate across the wafer. The growth rate uniformity down the wafer in the flow direction is quite good. This uniformity pattern is attributed to a single convective roll in the gas flow, in the deposition chamber, induced by the thermal expansion of the gas and the slight asymmetry in the position of the susceptor within the quartz tube. Since the susceptor is slightly closer to one of the chamber walls, the gas expansion will be asymmetrical with respect to the tube axis and a roll develops in the gas flow.

The global uniformity of the DEGaCl-based growth on a non-patterned substrate indicates a monotonic decrease in the growth rate down the flow axis of the quartz tube. The lower growth rate on the downstream side of the wafer is probably due to the decrease in the GaAs growth resulting from the generation of HCl from the GaAs growth upstream. Growth on the patterned substrate does not seem to be as strongly influenced by the growth-generated HCl as on the non-patterned substrate. The overall amount of GaAs deposited on the patterned wafer is less than on the non-patterned wafer due to the selective nature of the growth and the small amount of exposed substrate (< 5%). The global uniformity is otherwise very similar to that of the TMGa-based growths.

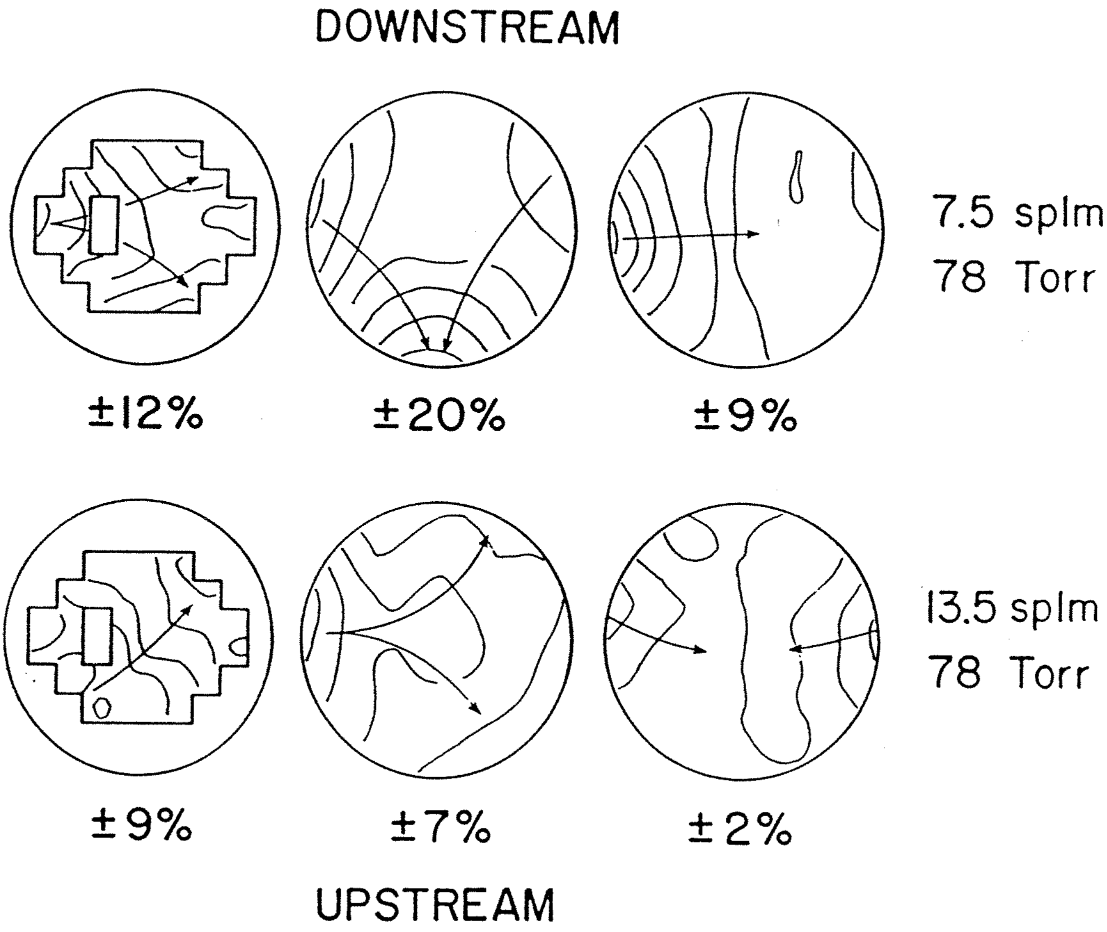

Figure 4.8. Contour plot of growth-rate uniformity of GaAs for: (left) DEGaCl-based growth on patterned substrates, (middle) DEGaCl-based growth on non-patterned substrates, and (right) TMGa-based growth on non-patterned substrates. The arrows indicate the direction of increasing layer thickness. The average thickness deviations from the mean thickness are also shown.

Increasing the total flow rate into the deposition chamber improved the global uniformity in all cases as shown in figure 4.8. The convective roll present in the growth with 7.5 slm total flow rate has been eliminated due to the higher gas velocity in the deposition chamber. The uniformity in the TMGa-based growth is greatly improved. The uniformity is mainly affected by the GaAs deposition on the warm chamber walls which causes some gas-phase depletion. The DEGaCl-based growths on both patterned and non-patterned substrates are similar. The increase in the growth rate across the wafer is quite similar to the roll-generated non-uniformity seen in the TMGa-based growth. The main effect of the higher gas velocity is to greatly improve the uniformity of the growth rate across the wafer.

4.4.2 Local Uniformity

The local growth rate of the DEGaCl-based GaAs growth is affected by several primary factors. The local ratio of the mask opening to masked regions appears to be the primary determinant of the local growth rate. The specific growth chemistry also influences the local growth rate and growth profile, as shown in figure 4.9. These growth profiles are obtained by a mechanical profilometer.

The InAs was grown using TMIn at a growth temperature of 700°C. Under these conditions, the InAs growth was partially selective. The pattern used in this study was an array of lines surrounded by wide borders. The TMIn-based growth exhibits an overall "U shape" to the growth profile. Selectivity in the InAs case can be attributed to the surface diffusion of the deposited In across the mask surface to a mask opening. The "U" profile results from the accretion of material diffusing from the surrounding masking material onto the exposed GaAs with limited diffusion over the exposed growing surface. The surface diffusion length inferred from this profile is about 100 μm at 700°C growth temperature. The surface diffusion length on the masking material may be even higher.

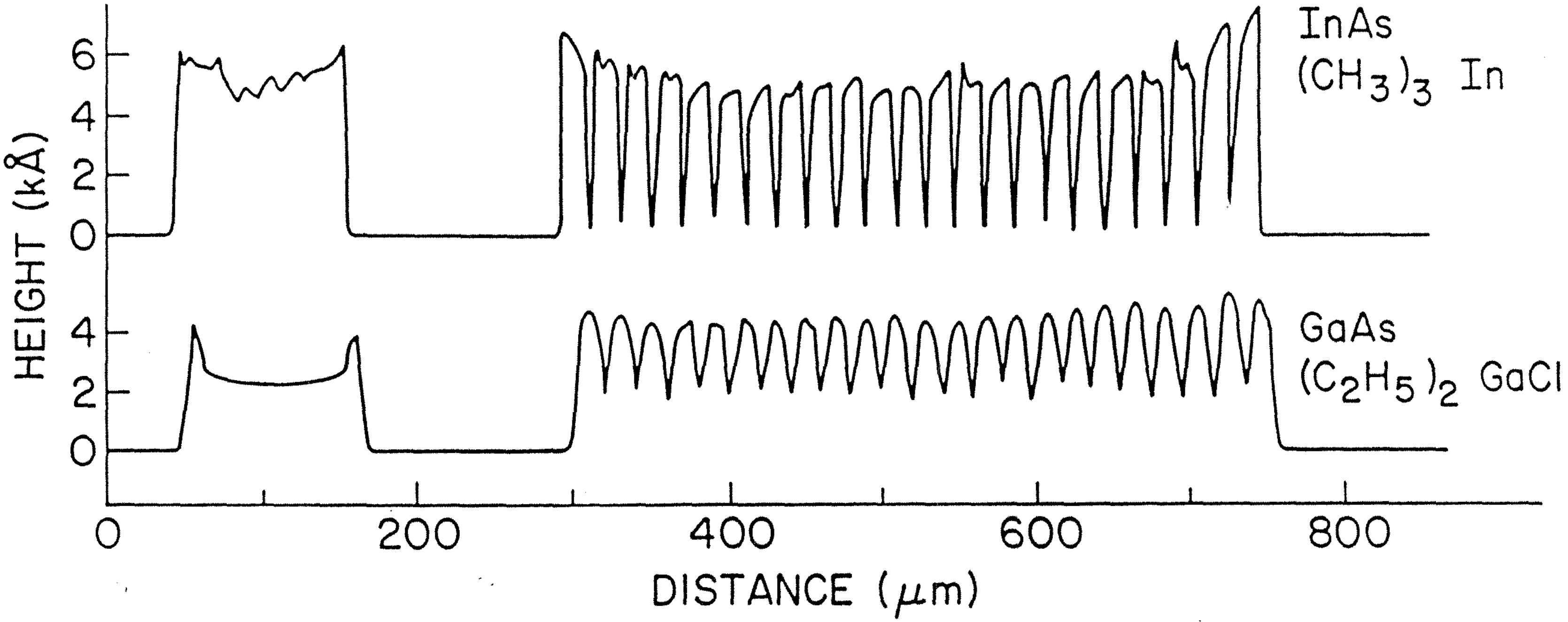

Figure 4.9. The thickness-profile plots of two patterned regions grown using two different growth chemistries. The InAs profile results from the diffusion of In growth species from the surrounding masked region to the mask openings. The flat profiles seen on the DEGaCl-based growth results from the selective adsorption of the growth precursor on the GaAs exposed regions. The sharp peaks on the edge of the DEGaCl profiles are artifacts of the profilometer measurements.

The lower profile in figure 4.9 is from a GaAs growth using DEGaCl. The profile is distinctly different from the InAs case. The wide borders possess sharp peaks at the edges of the growth. This "peak" results from the facet formation at the edges of the selectively grown regions. The sharpness of this peak is exaggerated by the difference on the vertical and horizontal distance scales used in this figure and the finite size of the profilometer tip. Closer examination of the peak profile indicates that the actual slope is about 1°-3°. The growth rate within the stripe openings does not exhibit the "U-shaped" profile as in the InAs case. Growth in these small stripe openings exhibit similar edge peaks to the wider border areas which yield an apparent, not actual, change in growth rate between the border area and the stripes. The DEGaCl selective epitaxy is quite uniform on a local level. The lack of a "U-shaped" profile indicates that the growth mechanism responsible for the selectivity is not the same as in the InAs or conventional OMVPE growth. The uniform growth rate indicates that the mechanism of the selectivity is the preferential adsorption of the growth precursor within the mask openings.

Another important factor affecting the local growth rate is the orientation of the mask opening in relation to the crystallographic directions of the substrate. This factor becomes more important as the growth thickness approaches the width of the initial mask opening. The selective growth of stripes oriented along the [011] direction will be used here as an example. As the selective growth progresses, the trapezoidal cross-sections of the [011] stripes evolve into triangles as shown earlier in figure 4.6. The two non-parallel sides of the trapezoidal cross-section are the (111)-type crystallographic planes shown schematically in figure 4.10. Since these (111)-type planes are slow-growth planes, most of the growth precursor, in this case GaCl, adsorbed on the (111)-type planes will either diffuse onto the masking material and desorb or diffuse onto the (100) plane and contribute to the growth on the (100) plane. The growth-rate equation in figure 4.10 describes this process mathematically, where dH is the enhanced local growth

Local Growth Rate of [011] Stripes

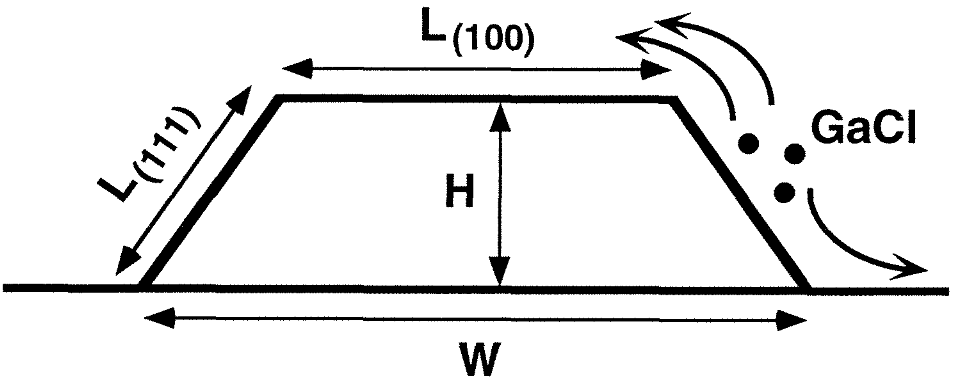

$$dH = dh\left(\frac{L_{(100)} + L_{(111)}}{L_{(100)}}\right)$$

dH = Local Growth Rate
dh = Nominal Growth Rate

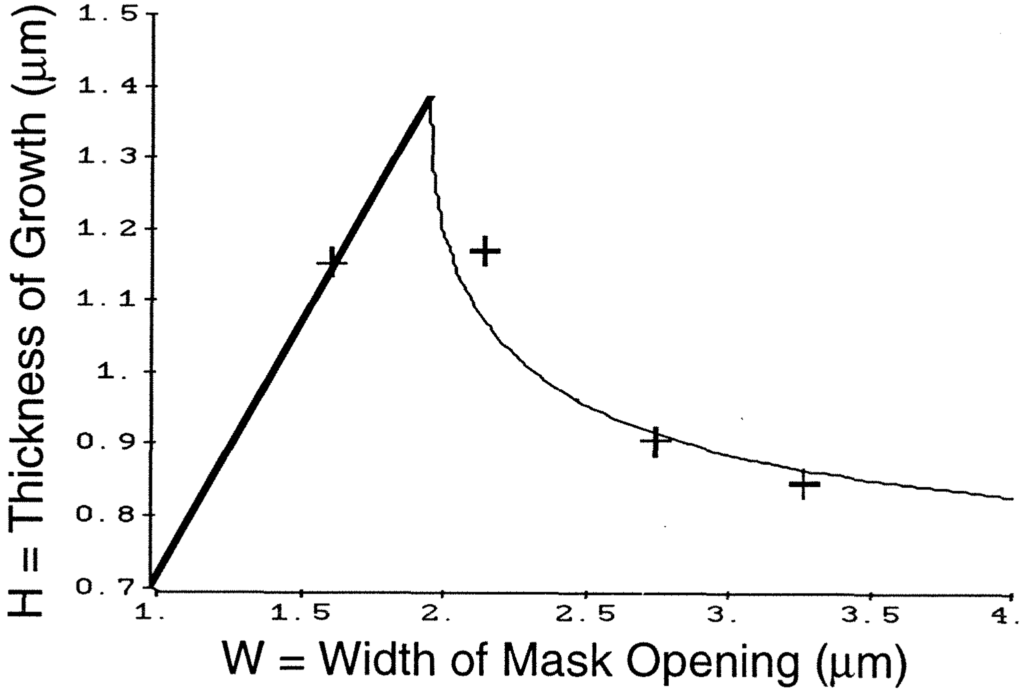

Figure 4.10. *Top*: schematic illustration of a growing [011] stripe with widening (111) facets and a narrowing (100) facet. The widths of the individual facets affect the local growth rate dH. *Bottom*: a plot of growth thickness versus mask opening width for stripes oriented along the [011] crystallographic direction.

rate on the (100) plane, and dh is the nominal growth rate without considering this effect. In figure 4.10, a graph is also plotted relating the thickness of the growth H to the width of the initial mask opening W for a given growth time. The straight portion of the graph is the geometric limit reached by the triangular cross-section. The curved portion of the graph shows the growth-rate enhancement as the trapezoidal cross-section approaches the triangular limit. Also plotted are data points taken from actual growths for comparison. This enhancement of local growth rate becomes more important as the growth thickness approaches the width of the initial mask opening.

4.5 Applications and Selective Heterostructure Formation

The selective epitaxy of GaAs, $Al_xGa_{1-x}As$, and $In_xGa_{1-x}As$ makes possible the selective formation of heterostructures. This application of selective epitaxy was explored in the growth of multilayer heterostructures in stripe mask openings. The complete structures of the selectively grown stripes, oriented along the [010] direction, are shown schematically in figure 4.11. The heterostructures are each composed of a base GaAs layer and two thinner GaAs layers placed in between three AlGaAs layers. The entire heterostructure is grown in a single run on a GaAs substrate precoated with a 2 μm layer of $Al_{0.3}Ga_{0.7}As$, a 20 nm layer of GaAs to prevent the oxidation of the $Al_{0.3}Ga_{0.7}As$ layer, and a 20 nm layer of Si_3N_4 as the dielectric mask. The additional layers in the substrate were necessary in order to suppress the luminescence from the underlying GaAs substrate. Stripe openings were made in the dielectric mask layer using conventional photolithographic procedures. Two different stripes are shown schematically in figure 4.11. The narrow stripe has a triangular cross-section. The wide stripe has a trapezoidal cross-section with the narrow flat side on the top. The wide stripe would eventually develop a triangular cross-section also, if additional material is deposited.

Schematic Cross-Sections of [010] Stripes

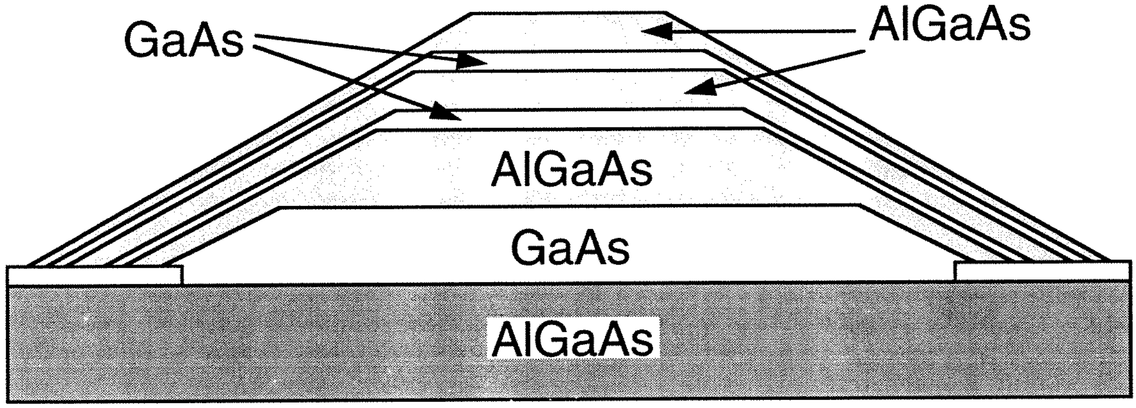

Wide Stripe

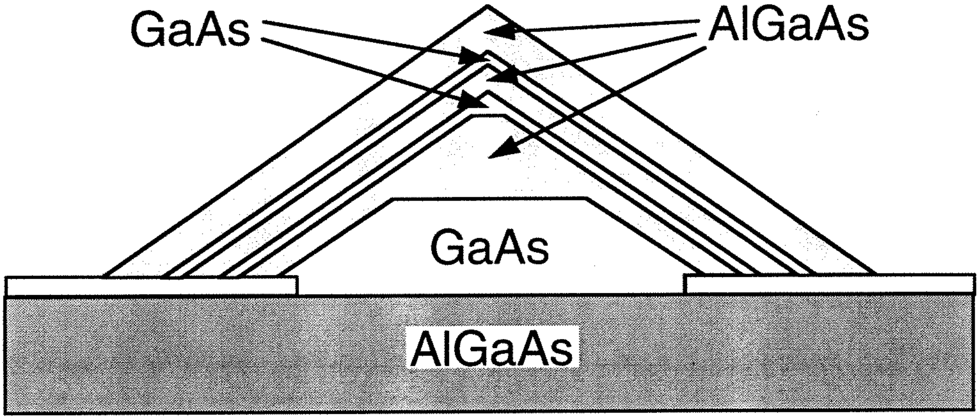

Narrow Stripe

Figure 4.11. Schematic illustration of selectively grown multilayer stripes containing GaAs/AlGaAs heterostructure. These stripes are oriented along the [010] crystallographic direction.

The back-scattered electron (BSE) and cathodoluminescence (CL) images of the actual wide stripe are shown in figure 4.12. In the BSE images, the brighter portion of the image corresponds to GaAs and the darker portion corresponds to AlGaAs. Except for the slight bowing on the top surface, the heterostructure shown in the BSE images corresponds to the wide stripe shown in the schematic diagram.

One distinct characteristic of selective epitaxy emerges from the CL images. For the selective epitaxy of binary compounds such as GaAs, compositional shift is not possible. For the selective epitaxy of ternary or quaternary compounds such as AlGaAs on patterned masked substrates, compositional shifts occur as the selective growth progresses. For example, the peak luminescence wavelength of the bottom AlGaAs layer (not the one in the substrate) is at ~745 nm, as indicated by the strong luminescence shown in the CL image at 745 nm. The luminescence peak of the middle AlGaAs layer is at ~708 nm, indicating that a shift in the material composition has occurred even though all of the AlGaAs layers were grown using identical OMVPE parameters. The magnitude of material-composition shifts for different layers within a heterostructure is determined by a complex set of parameters including the crystallographic orientation and the area filling fraction of the mask opening, the growth rate, the chamber pressure, and other variables in the OMVPE growth process. Careful calibration of individual layer thicknesses and compositions is necessary for the successful growth of heterostructures by selective epitaxy.

One potential device application of the selectively grown heterostructures is a narrow stripe laser as illustrated in figure 4.13. The width of the active region is reduced to ~200 nm. The p-doped top region and the n-doped bottom region are entirely isolated from each other by a layer of silicon nitride. This laser would have low threshold current, low electrical circuit parasitics, and high electrical modulation speed, because there are no parasitic p-n junctions and no leakage current. Additional advantages of this

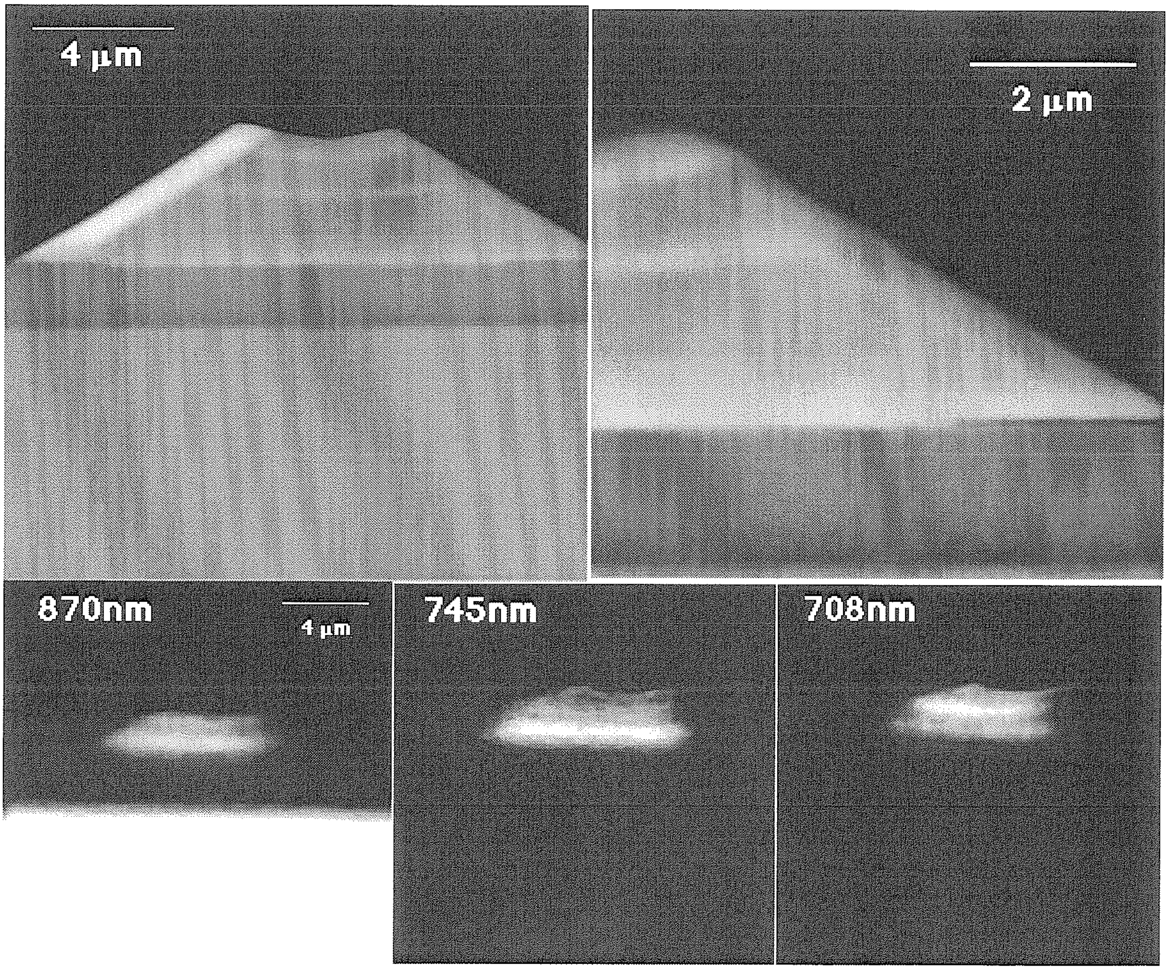

Figure 4.12. Backscattered-electron (top 2) and spectrally-resolved cathodoluminescence (bottom 3) cross-sectional images of a wide stripe oriented along the [010] crystallographic direction.

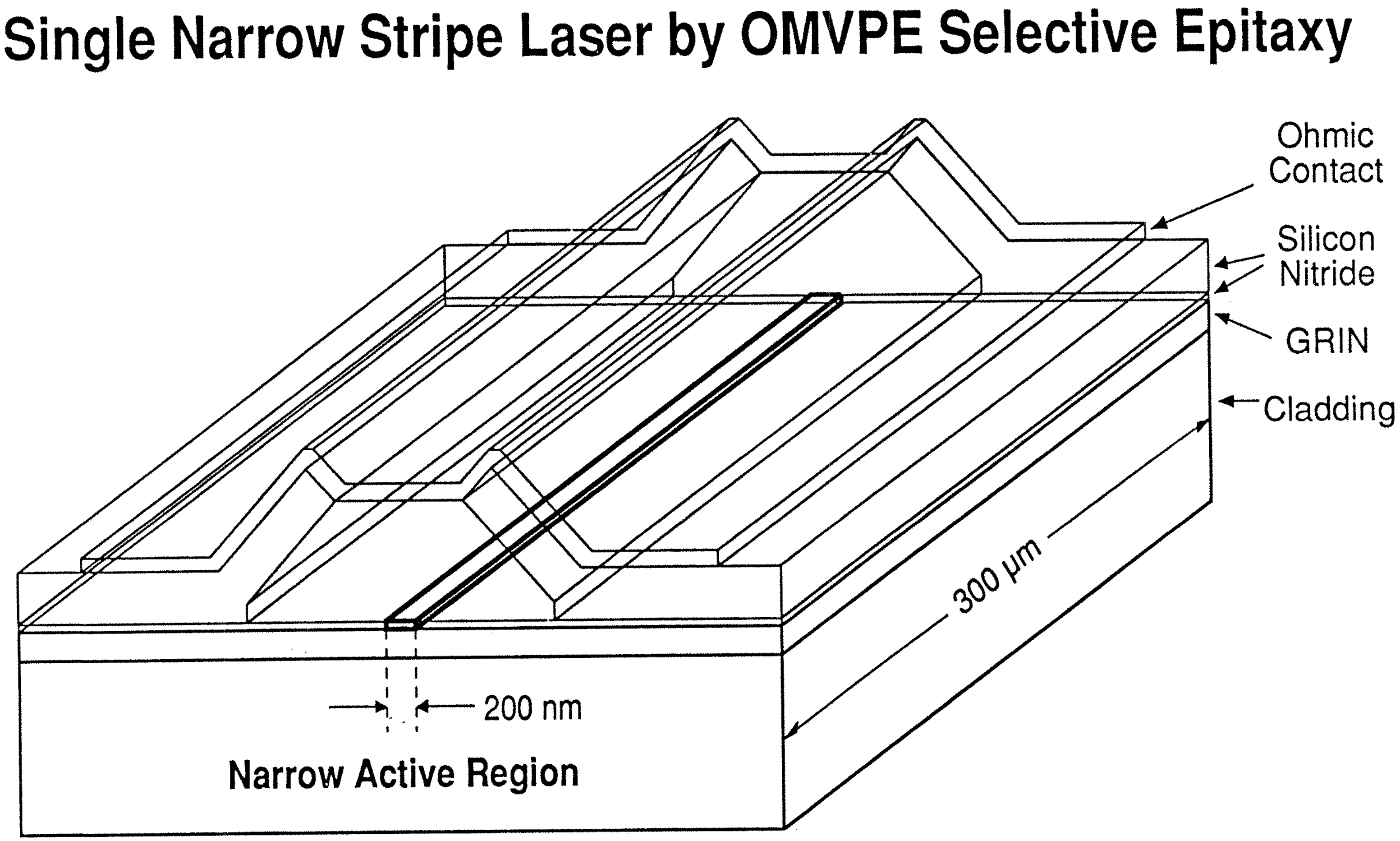

Figure 4.13. Schematic diagram of a narrow-stripe semiconductor diode laser fabricated by OMVPE selective epitaxy.

laser include the high optical-mode confinement possible, the flexible control of waveguide modes, and the relatively simple and straightforward fabrication procedures.

4.6 Discussion and Conclusion

The OMVPE growth chemistry has been known to determine many of the important parameters which impact the utility of the grown materials. Most studies of the growth chemistry have centered on the purity of the growth product and the uniformity of the deposition. This present study utilized halogen-based organometallic compounds such as DEGaCl to achieve extremely selective growth. These organometallic compounds are believed to decompose into the volatile mono-chloride species which are used in the inorganic-based growth of compound semiconductors. The *in situ* generation of these growth reactants mimics the inorganic-based growth chemistry near the growth surface, allowing for complete selectivity on patterned and masked substrates.

The fabrication of selectively grown heterostructures has been demonstrated using these halogenated precursors in combination with the conventional precursors under standard OMVPE growth conditions. The processing required for the selective regrowth step does not seem to adversely impact the pre-processed structure, at least in the $Al_xGa_{1-x}As/GaAs$ material systems. The use of lithographically-defined masked regions to achieve selective epitaxy offers many advantages over the alternative approaches mentioned in the introduction. Control of the growth morphology and facet formation can be used to advantage in many applications. Since the growth is truly selective using DEGaCl, the absence of polycrystalline material eliminates the additional processing steps for the subsequent removal of this extraneous material. Lastly, selective epitaxy can be achieved in a variety of material systems which allow the growth of many combinations of heterostructures. The extension to the phosphorus-based material systems should be straightforward.

This novel growth technique requires further development in the understanding of the factors which influence the local and global uniformity of the deposition. The range of physical dimensions, microns to centimeters, and the many crystallographic directions, each with different growth properties, encountered in the determination of the local and global growth rates make this problem numerically difficult. In addition, shifts in the material composition occur for layers within a heterostructure containing ternary or quaternary materials. For the successful application of selective epitaxy, careful calibration of the layer composition is mandatory for each specific heterostructure and mask pattern. A better understanding of the growth chemistry should lead to the design of more suitable precursors for the growth of alternative materials and expand the application for selective epitaxy.

Bibliography

[1] C. P. Lee, I. Samid, A. Gover, and A. Yariv, Appl. Phys. Lett. **29**, 365 (1976).

[2] S. B. Kim and Y. S. Kwon, J. Appl. Phys. **61**, 5478 (1987).

[3] U. König, U. Langmann, K. Heime, L. J. Balk, and E. Kubalek, J. Crystal Growth **36**, 165 (1976).

[4] H. Heinecke, A. Brauers, F. Grafahrend, C. Plass, N. Pütz, K. Werner, M. Weyers, H. Lüth, and P. Balk, J. Crystal Growth **77**, 303 (1986).

[5] K. Kamon, M. Shimazu, K. Kimura, M. Mihara, and M. Ishii, J. Crystal Growth **77**, 297 (1986).

[6] R. Azoulay, N. Bouadma, J. C. Bouley, and L. Dugrand, J. Crystal Growth **55**, 229 (1981).

[7] C. Ghosh and R. L. Layman, Appl. Phys. Lett. **45**, 1229 (1984).

[8] K. Nakai and M. Ozeki, J. Crystal Growth **68**, 200 (1984).

[9] Y. Takahashi, S. Sakai, and M. Umeno, J. Crystal Growth **68**, 206 (1984).

[10] J. P. Duchemin, M. Bonnet, F. Koelsch, and D. Huyghe, J. Crystal Growth **45**, 181 (1978).

[11] K. Kamon, S. Takagishi, and H. Mori, J. Crystal Growth **73**, 73 (1985).

[12] Y. Nakayama, S. Ohkawa, and H. Ishikawa, Fujitsu Sci. and Tech. J. **13**, 53 (1977).

[13] T. F. Kuech, M. A. Tischler, and R. Potemski, Appl. Phys. Lett. **54**, 910 (1989).

[14] F. W. Tausch Jr. and A. G. Lapierre, J. Electrochem. Soc. **112**, 706 (1965).

[15] D. W. Shaw, J. Electrochem. Soc. **113**, 904 (1966).

[16] G. H. Olsen and V. S. Ban, Appl. Phys. Lett. **28**, 734 (1976).

[17] A. Okamoto and K. Ohata, Appl. Phys. Lett. **51**, 1512 (1987).

[18] E. Colas, C. Caneau, M. Frei, E. M. Clausen Jr., W. E. Quinn, and M. S. Kim, Appl. Phys. Lett. **59**, 2019 (1991).

[19] S. H. Jones and K. M. Lau, J. Electrochem. Soc. **134**, 3149 (1987).

[20] E. Kapon, S. Simhony, R. Bhat, and D. M. Hwang, Appl. Phys. Lett. **55**, 2715 (1989).

[21] N. H. Karam, H. Liu, I. Yoshida, B.-L. Jiang, and S. M. Bedair, J. Crystal Growth **93**, 254 (1988).

[22] T. F. Kuech, M. S. Goorsky, M. A. Tischler, A. Palevski, P. Solomon, R. Potemski, C. S. Tsai, J. A. Lebens, and K. J. Vahala, J. Crystal Growth **107**, 116 (1991).

[23] G. B. Stringfellow, *Organometallic Vapor-Phase Epitaxy*, Academic Press (1989).

[24] M. E. Hoenk and K. J. Vahala, Rev. Sci. Instrum. **60**, 226 (1989).

[25] D. W. Shaw, J. Crystal Growth **31**, 130 (1975).

Chapter 5

Fabrication of Nanometer-Scale Wire and Dot Structures by Selective Epitaxy

The selective growth of nanometer-scale GaAs wire and dot structures using organometallic vapor-phase epitaxy is demonstrated. Spectrally-resolved cathodoluminescence images as well as spectra from single dots and wires, passivated by an additional $Al_xGa_{1-x}As$ layer, are presented. Growth behavior of GaAs wires with thick $Al_xGa_{1-x}As$ overgrowths is also presented for potential device applications. A blue shifting of the GaAs luminescence peak is observed as the size scale of the wires and dots decreases.

5.1 Introduction to Quantum Wires and Dots

Conventional crystal-growth techniques, such as molecular-beam epitaxy (MBE) and organometallic vapor-phase epitaxy (OMVPE), have achieved atomic-scale compositional control in one dimension along the growth direction. This capability has resulted in a wealth of new physical phenomena and device applications, producing structures exhibiting quantum confinement in one dimension (quantum wells). There has been significant interest in developing techniques enabling the equivalent control in the lateral directions perpendicular to the growth direction. Such a capability would greatly enhance the variety of possible structures as well as provide advancements in applications such as monolithic integration of photonic devices. A major goal of this effort is to fabricate structures exhibiting quantum confinement in two or three dimensions, namely quantum wires or quantum dots.

Schematic drawings of a quantum well, a quantum wire, and a quantum dot are presented in figure 5.1 (top). Bulk material is also illustrated for comparison. A quantum well has quantum confinement in one dimension (L_z). A quantum wire has quantum confinement in two dimensions (L_y and L_z). A quantum dot has quantum confinement in three dimensions (L_x, L_y, and L_z). For quantum structures using the GaAs/AlGaAs material systems, L_x, L_y and L_z should be on the order of 10 nm for observable optical effects at room temperature. Also shown in figure 5.1 (bottom) are three-dimensional arrays of quantum wells, quantum wires, and quantum dots. Potential barriers containing material of a higher band-gap confine and isolate the individual quantum structures within each array.

An important application of quantum wires or dots would be their incorporation into the active region of a laser diode, which has been predicted to significantly improve present performance [1,2]. The improvements result from the narrower optical gain spectrum provided by these quantum structures. The optical gain spectrum corresponds roughly to the density of states function as shown in figure 5.2 for bulk material, quantum well, quantum wire, and quantum dot. The narrowing of the density of states function near E_{gap} with increasing quantum confinement, and consequently the narrowing of the gain spectrum, is apparent. The narrowing of the gain spectrum would result in reduced threshold current and linewidths for laser diodes containing quantum wires or dots.

A variety of approaches is being studied to achieve lateral confinement for quantum wires and dots. Lateral confinement has been produced in an already existing quantum well by defining a confinement pattern using techniques such as electron-beam or ion-beam lithography and then transferring this pattern into the quantum well by etching [3-6], impurity-induced disordering using ion-beam implantation [7], or selective

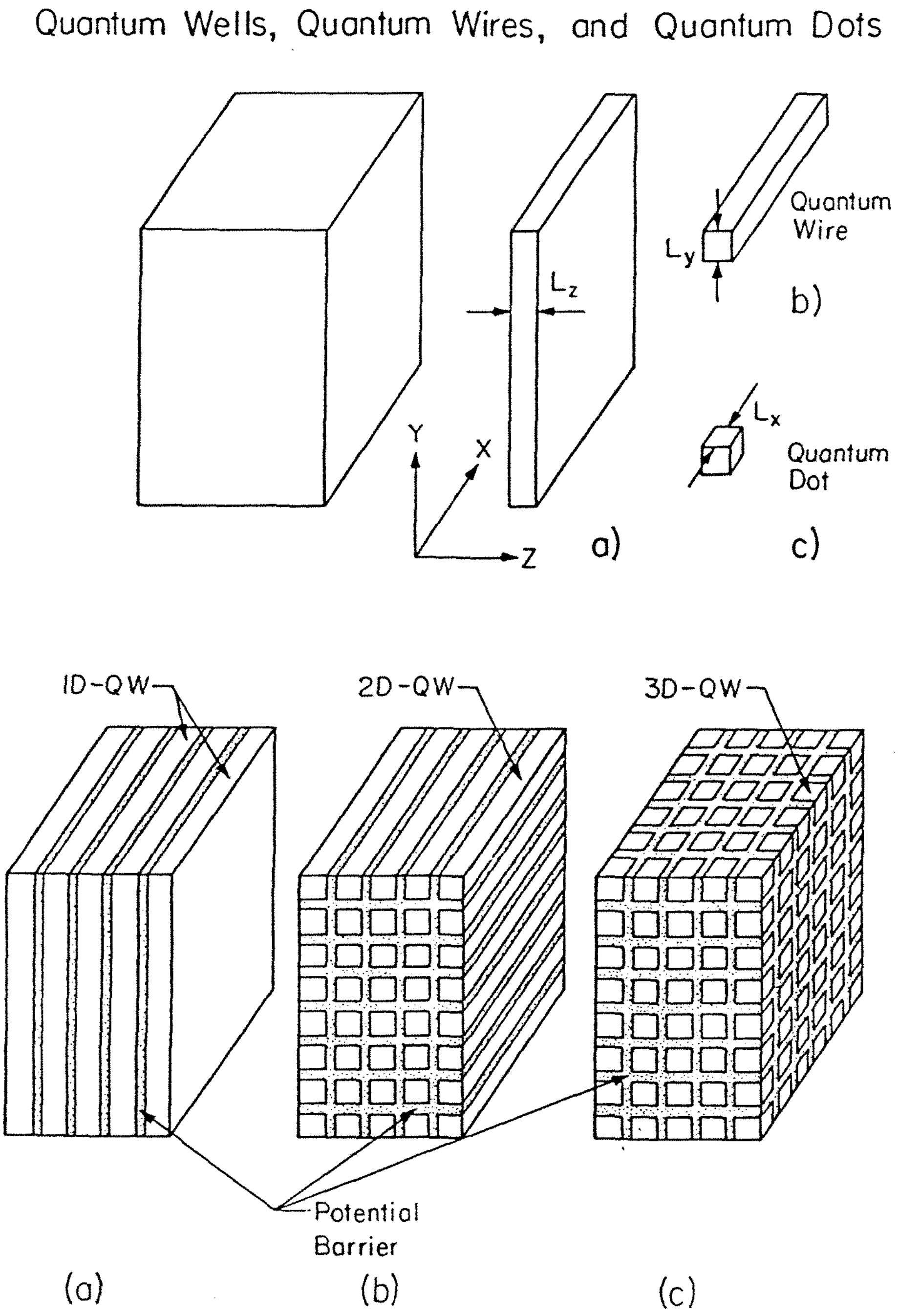

Figure 5.1. *Top*: schematic drawings of a quantum well (a), a quantum wire (b), and a quantum dot (c). Bulk material is also illustrated for comparison. *Bottom*: schematic drawings of three-dimensional arrays of quantum wells (a), quantum wires (b), and quantum dots (c).

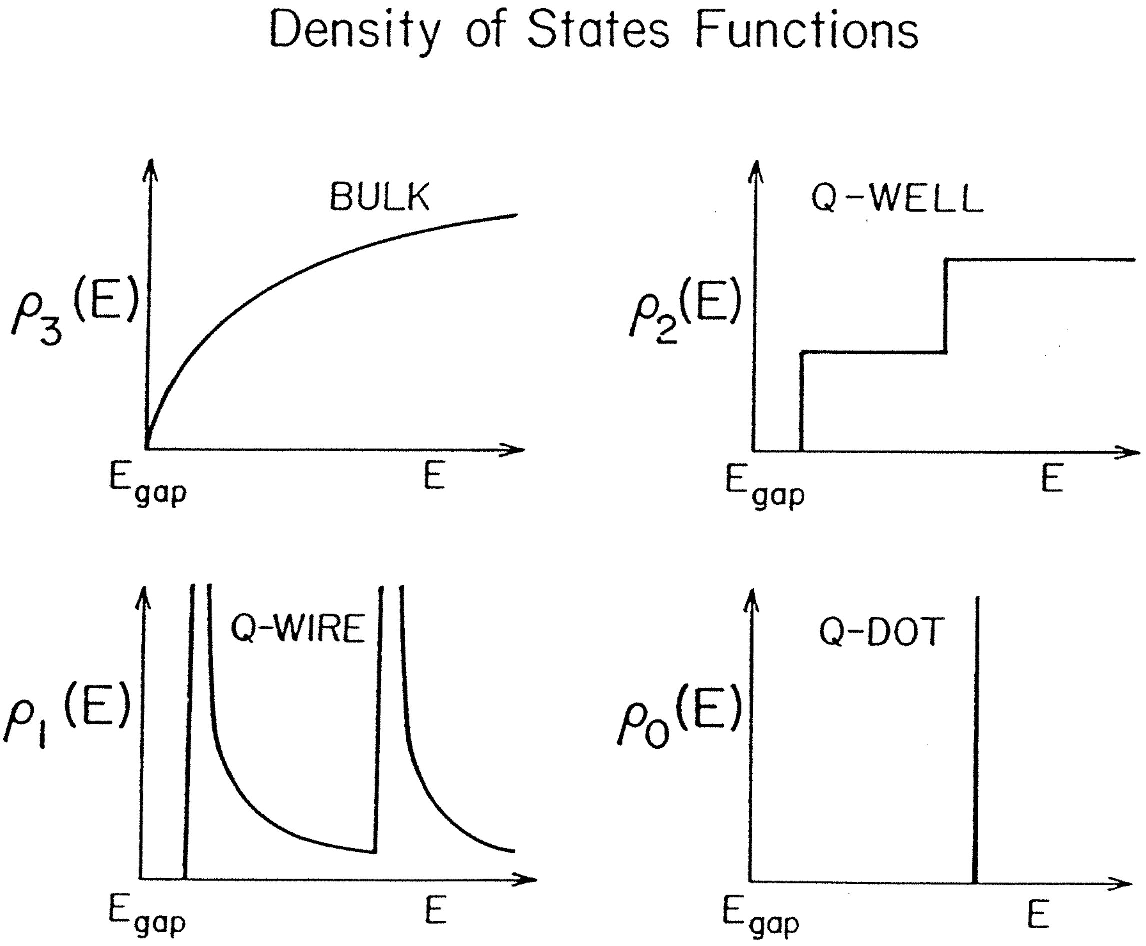

Figure 5.2. The density of states function for bulk material (BULK), quantum well (Q-WELL), quantum wire (Q-WIRE), and quantum dot (Q-DOT).

diffusion [8]. However, such methods suffer from free-surface effects, creation of a damage field during implantation, or lack of interface control due to the random nature of the disordering mechanism. Methods have emerged which allow the formation of nanostructures during the epitaxial growth process itself. Growth on patterned substrates has shown interesting compositional modulation effects [9] and has demonstrated stimulated emission from a single quantum wire [10]. Wires grown by migration-enhanced epitaxy on a tilted substrate have exhibited optical anisotropies associated with confinement effects [11]. These latter methods have not yet been used to produce quantum dot structures however.

In this chapter, the application of selective epitaxy to the fabrication of arrays of nanometer-scale wires and dots is presented [12]. Selective epitaxy, described earlier in chapter 4, refers to the laterally- and spatially-controlled growth of epitaxial material within openings of a masking material. In the work presented here, the structures grown are determined by patterning a masked substrate using electron-beam lithography. This allows the selective growth of GaAs wires and dots which can be followed by a single-crystal growth of $Al_xGa_{1-x}As$ to embed the structures *in situ*. Using cathodo-luminescence (CL) scanning electron microscopy, spectra of single dots and wires as well as spectrally-resolved CL images are presented.

5.2 Sample Preparation and Growth

The samples prepared for selective epitaxy comprised a 2 μm undoped $Al_{0.38}Ga_{0.62}As$ layer followed by a 20 nm GaAs cap layer grown by OMVPE on semi-insulating (100) GaAs substrates. For the masking material, 20 nm of silicon nitride was formed by plasma-enhanced chemical-vapor deposition (PECVD) on the samples. Arrays of 100-μm-long stripe openings with widths ranging from 90 nm to 300 nm were patterned into the silicon-nitride layer using electron-beam lithography and CF_4 plasma etching. The stripe openings were oriented in the [011], $[01\bar{1}]$, and [010] crystallographic directions. 100 μm x 100 μm square openings were also written into each sample as control.

The selective growth of GaAs was performed in a low-pressure horizontal OMVPE reactor. Details of the selective growth process have been described in chapter 4. A range of samples was grown with the growth temperatures varying from 600°C to 750°C. Approximately 100 nm of GaAs was grown on the samples as measured from the cross-section of the square area on the samples. The actual growth thicknesses of the dots and lines were different depending on the crystallographic orientation of the initial mask openings. The GaAs was found to grow selectively within the openings of the mask and the selectivity did not depend on growth temperature. We observed growth of GaAs in all openings, including the smallest.

5.3 Characterization of Wire and Dot Growths

Figure 5.3a shows a micrograph of an array of dots grown by this technique. The growth displays a highly facetted profile with excellent size uniformity. The exact orientations of the crystallographic bounding planes are difficult to measure for such small structures. In general, the slow-growth crystallographic planes determine the facet profile of each dot. For the inorganic-based growth of GaAs, these have been observed to be the {110} and {111} families of planes [13,14]. Selectively grown GaAs wires also exhibited facetted profiles with bounding planes depending on the crystallographic orientation of the initial stripe opening. Figure 5.3b shows wires grown oriented in the [010] direction. For the three wire orientations used in this study, a uniform facet profile was observed along each wire.

To obtain strong luminescence from such small structures, it is important that no free surface exists that would generate nonradiative-recombination centers. Also, both types of carriers (electrons and holes) should be confined within each wire or dot by surrounding the entire structure with a higher band-gap material. This was accomplished

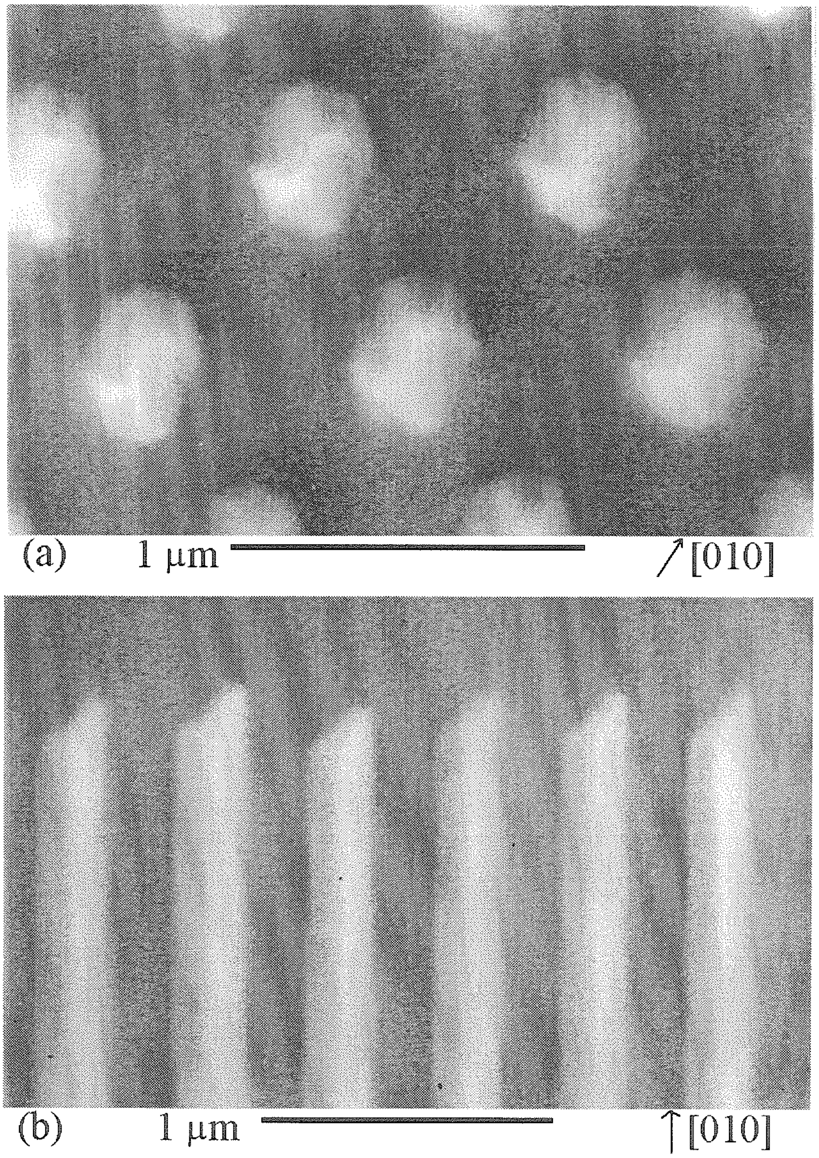

Figure 5.3. Scanning electron micrographs of selectively grown GaAs wires and dots. Both the dots in (a) and the wires in (b) show facetted growth profiles. Crystallographic orientations are as indicated in the figures.

in a second set of samples in which the GaAs selective growth (identical to the previous set) was followed by a growth of $Al_xGa_{1-x}As$ (nominally x = 0.3) with an approximate growth thickness of 250 nm. These samples contained patterns with similar electron-beam-exposure conditions as the previous set.

The luminescence properties of such passivated structures were investigated using cathodoluminescence (CL). Details of the CL collection system are given elsewhere [15]. CL spectra at 77°K of single wires and dots were measured as a function of lateral width and diameter, respectively. These spectra are shown in figures 5.4a and 5.4b. For comparison, the spectrum of a selectively grown square area on the same sample is also included in the figures. The luminescence intensity of these square areas was comparable to conventionally grown GaAs layers. The exact size of the GaAs wire or dot is difficult to ascertain for the passivated samples since the lateral growth of the $Al_xGa_{1-x}As$ passivation layer is dependent upon the initial size of the GaAs structures, the wire orientation, the pattern density, and the growth conditions. The sizes were estimated by using the first set of samples which have similarly exposed patterns on which only GaAs was grown. For each size range, numerous spectra of dots and wires were taken, showing only a small distribution in peak position about the luminescence peaks seen in the figures. As the dimensions of the structures decrease, the luminescence peaks show an increasing blue shift.

One possible cause of the blue shift is the increasing quantum confinement of the carriers in the GaAs structures. The shifts, however, are larger than those predicted for quantum confinement at the estimated structure sizes. There are other possible effects that might contribute to lateral confinement. Electrostatic band-bending arising from the free surface on top of the passivating $Al_xGa_{1-x}As$ layer will alter the confinement potential. Strain created by the surrounding nitride layer could modulate the band gap in the wires and dots. Both effects could potentially increase the quantum confinement of the structures.

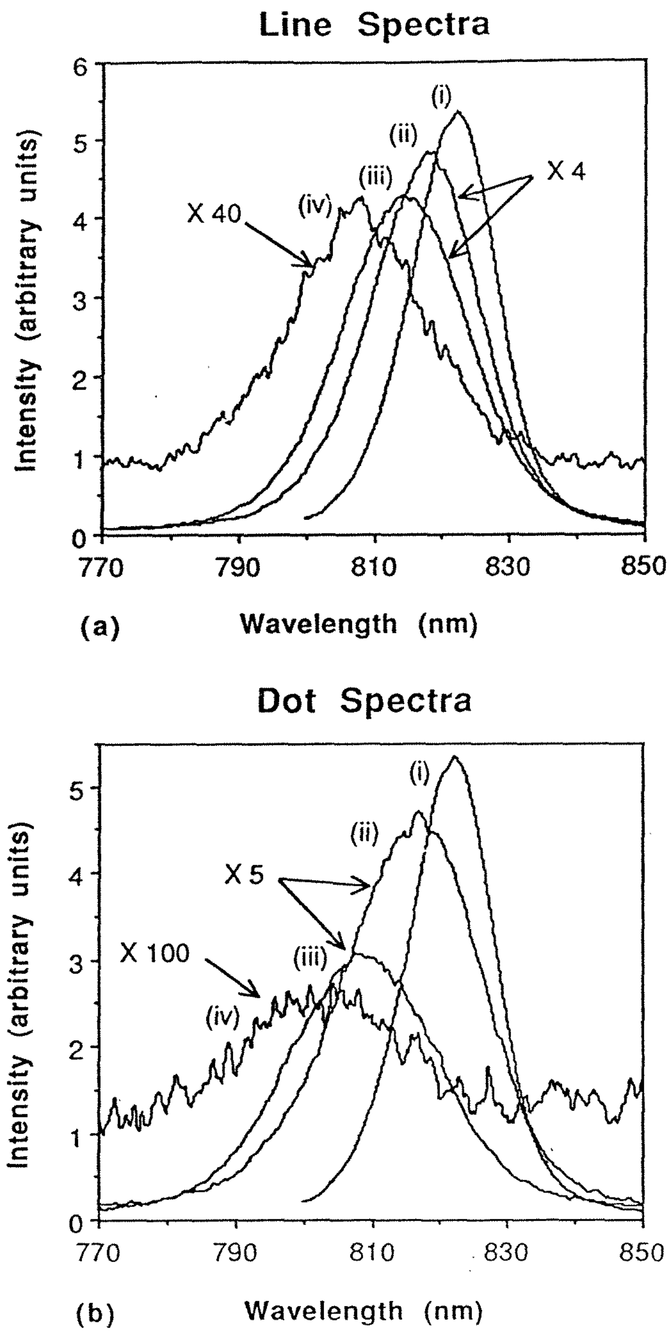

Figure 5.4. Cathodoluminescence spectra of wires and dots for three different wire widths and dot diameters, respectively. Plot (a) shows the wire spectra. For reference, spectra (i) is from a square-area control region. The estimated widths of the wires are (ii) 160 nm, (iii) 140 nm, and (iv) 100 nm. Plot (b) shows the dot spectra. (i) is the control region. The estimated dot diameters are (ii) 140 nm, (iii) 110 nm, and (iv) 80 nm.

Spectrally-resolved CL images with the wavelength set at the emission peak of the arrays of wires and dots were also taken. Typical images of wires and dots are shown in figures 5.5 and 5.6, respectively. The images shown consisted of 140-nm-wide wires with 0.83 μm center-to-center spacing and 110-nm-diameter dots with 0.66 μm center-to-center spacing. The wires and dots exhibit uniform emission intensity. This uniformity decreased somewhat for the smallest wires and dots.

In a third set of samples, the GaAs selective growth was followed by a much thicker growth of $Al_xGa_{1-x}As$ (nominally $x = 0.2$) with an approximate growth thickness of 1 μm. These samples contained patterns with similar electron-beam-exposure conditions as the previous sets. The growth behavior of the GaAs wires with thick $Al_xGa_{1-x}As$ overgrowths can be seen from the cross-sectional backscattered-electron images in figure 5.7. The thick $Al_xGa_{1-x}As$ overgrowths from the GaAs wires coalesce and form a continuous corrugated top surface. Depending on the crystallographic orientation of the initial stripe openings, the corrugated top surface planarizes to form a smooth plane and allows further growth or processing steps to form useful device structures. Overgrowths on wires oriented along the [010] direction seem to join and planarize most readily and perfectly, leaving no void within the final structure.

5.4 Conclusion

The application of selective epitaxy to the fabrication of nanometer-scale wires and dots was demonstrated. Wires and dots with diameters as small as 70 nm were prepared. Spectrally-resolved CL showed that the luminescence from single wires and dots was blue-shifted with respect to the bulk GaAs. Cross-sectional images of GaAs wires with thick $Al_xGa_{1-x}As$ overgrowths were presented. The $Al_xGa_{1-x}As$ overgrowths eventually planarize, allowing further growth or processing steps to form useful device structures. The success of this growth process shows promise for many potential device applications including quantum-wire and quantum-dot lasers.

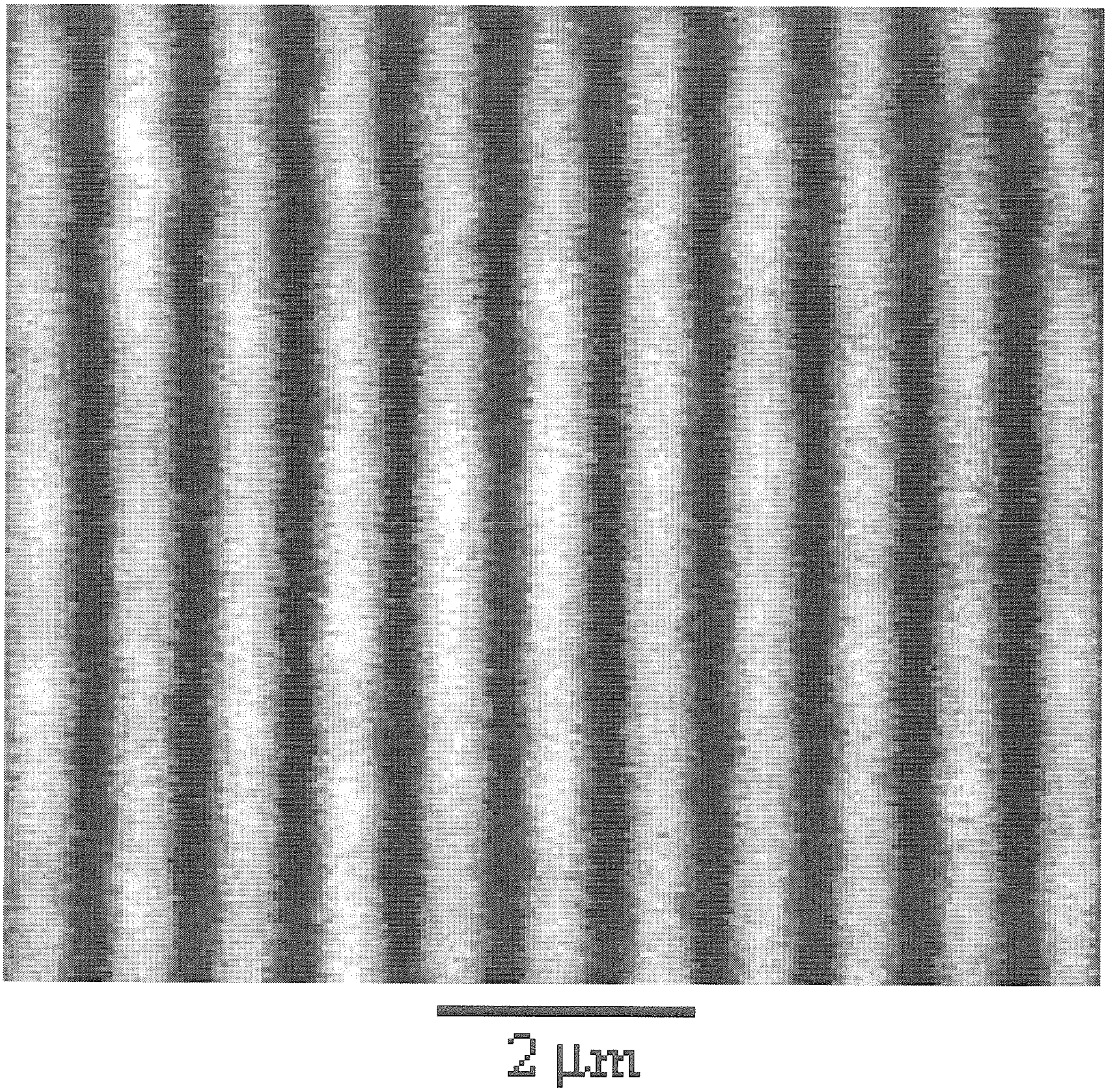

Figure 5.5. Spectrally-resolved cathodoluminescence image of an array of wires corresponding to spectra (iii) of figure 5.4(a). The wavelength is set to 814 nm.

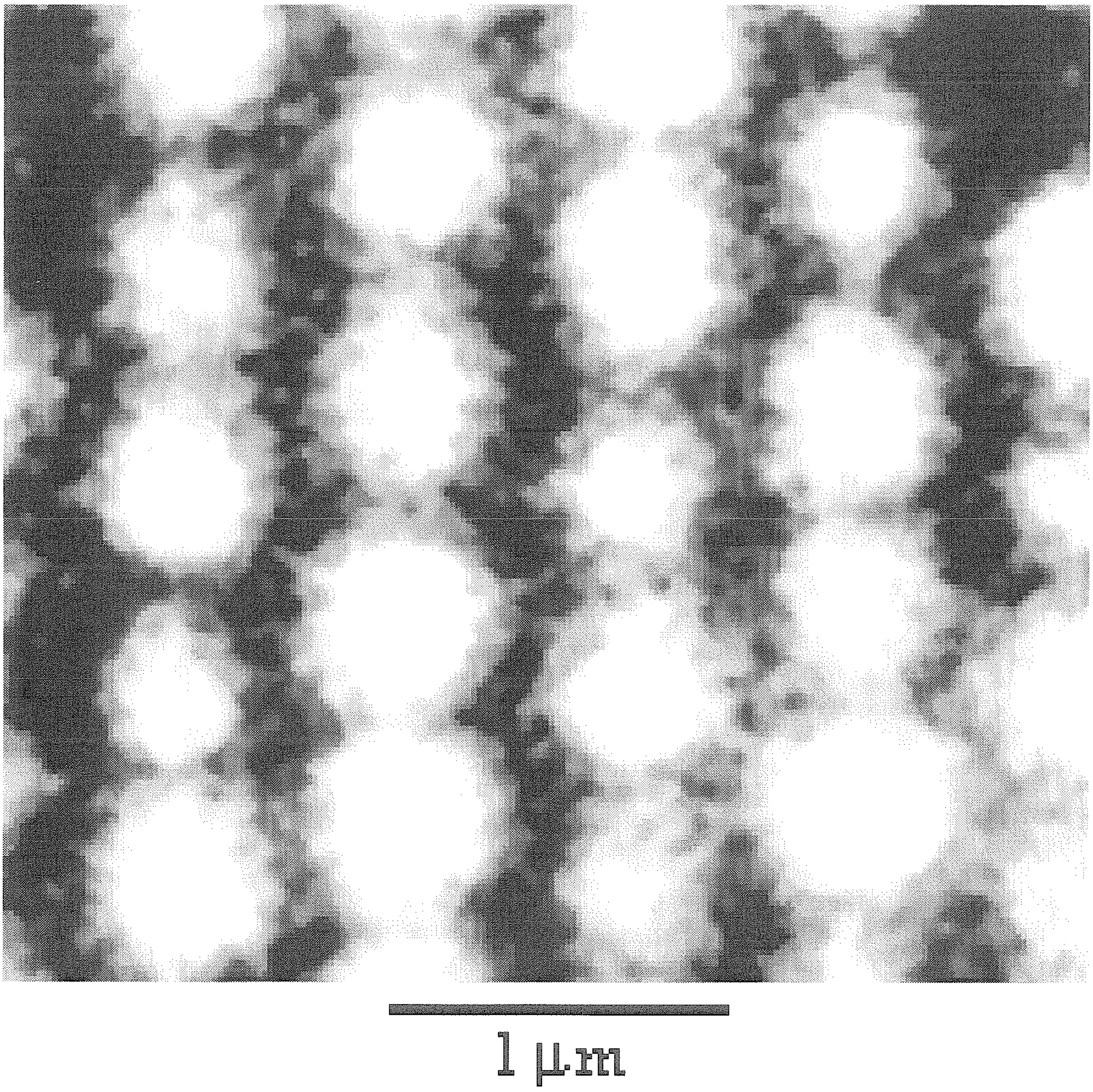

Figure 5.6. Spectrally-resolved cathodoluminescence image of an array of dots corresponding to spectra (iii) of figure 5.4(b). The wavelength is set to 809 nm.

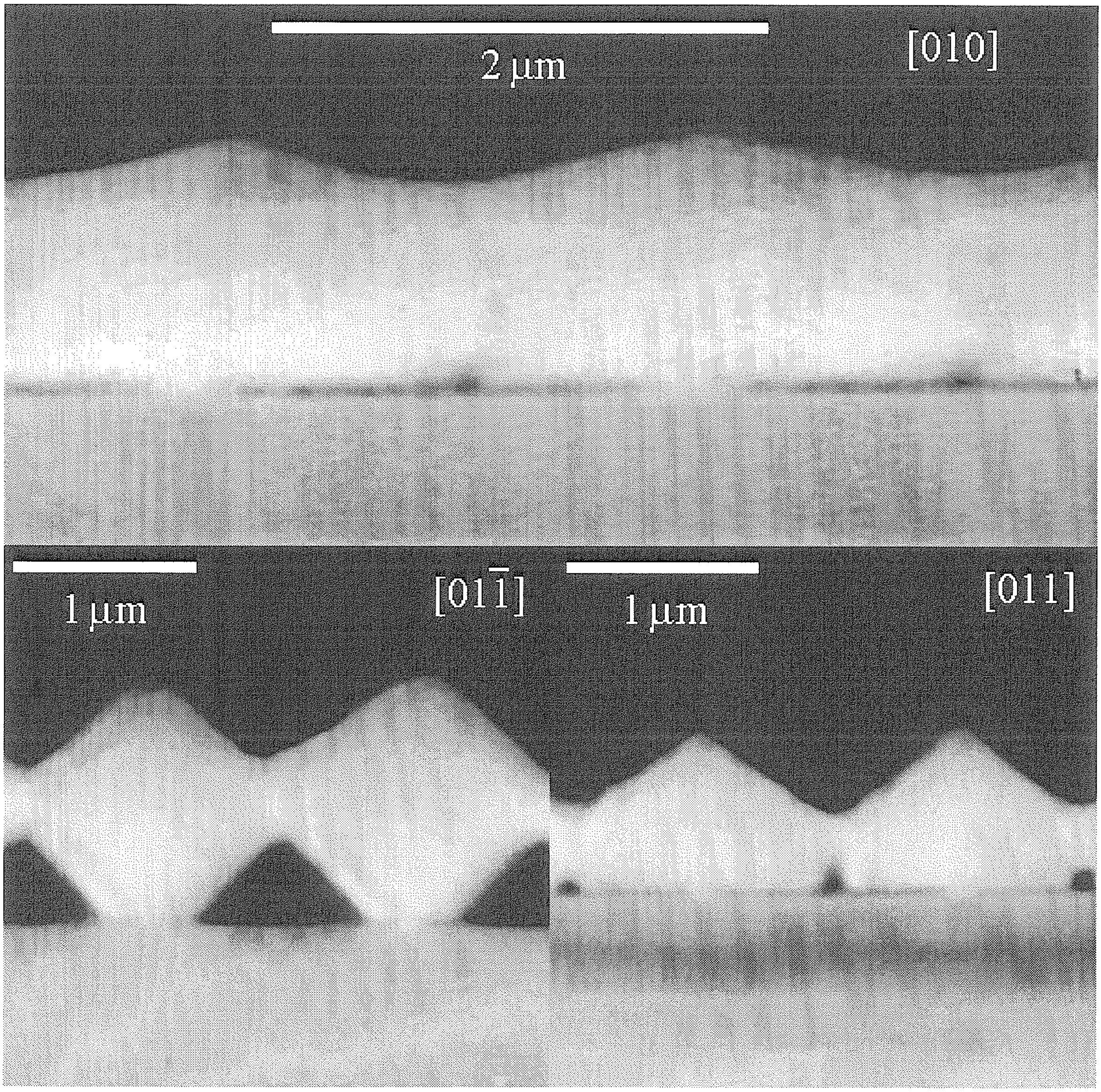

Figure 5.7. Cross-sectional backscattered-electron images of GaAs wires overgrown with thick $Al_xGa_{1-x}As$ layers. The wires are oriented along the [010], [01$\bar{1}$], and [011] crystallographic directions.

Bibliography

[1] Y. Arakawa, K. Vahala, and A. Yariv, Appl. Phys. Lett. **45**, 950 (1984).

[2] M. Asada, Y. Miyamoto, and Y. Suematsu, J. Quantum Electron. **QE-22**, 1915 (1986).

[3] K. Kash, A. Scherer, J. M. Worlock, H. G. Craighead, and M. C. Tamargo, Appl. Phys. Lett. **49**, 1043 (1986).

[4] H. Temkin, G. J. Dolan, M. B. Panish, and S. N. G. Chu, Appl. Phys. Lett. **50**, 413 (1987).

[5] D. Gershoni, H. Temkin, G. J. Dolan, J. Dunsmuir, S. N. G. Chu, and M. B. Panish, Appl. Phys. Lett. **53**, 995 (1988).

[6] B. I. Miller, A. Shahar, U. Koren, and P. J. Corvini, Appl. Phys. Lett. **54**, 188 (1989).

[7] J. Cibert, P. M. Petroff, G. J. Dolan, S. J. Pearton, A. C. Gossard, and J. H. English, Appl. Phys. Lett. **49**, 1275 (1986).

[8] H. A. Zarem, P. C. Sercel, M. E. Hoenk, J. A. Lebens, and K. J. Vahala, Appl. Phys. Lett. **54**, 2692 (1989).

[9] M. E. Hoenk, C. W. Nieh, H. Chen, and K. J. Vahala, Appl. Phys. Lett. **55**, 53 (1989).

[10] E. Kapon, D. M. Hwang, and R. Bhat, Phys. Rev. Lett. **63**, 430 (1989).

[11] M. Tsuchiya, J. M. Gaines, R. H. Yan, R. J. Simes, P. O. Holtz, L. A. Coldren, and P. M. Petroff, Phys. Rev. Lett. **62**, 466 (1989).

[12] J. A. Lebens, C. S. Tsai, K. J. Vahala, and T. F. Kuech, Appl. Phys. Lett. **56**, 2642 (1990).

[13] T. F. Kuech, M. A. Tischler, and R. Potemski, Appl. Phys. Lett. **54**, 910 (1989).

[14] D. W. Shaw, J. Cryst. Growth **31**, 130 (1975).

[15] M. E. Hoenk and K. J. Vahala, Rev. Sci. Instrum. **60**, 226 (1989).

Chapter 6

Formation of Highly-Uniform and Densely-Packed Arrays of GaAs Dots by Selective Epitaxy

Formation of highly-uniform and densely-packed arrays of GaAs dots by selective epitaxy using diethylgallium chloride and arsine is described. The arrays of GaAs dots are imaged using atomic-force microscopy (AFM). Accounting for the AFM tip radius of curvature, the smallest GaAs dots formed are 15-20 nm in base diameter and 8-10 nm in height with slow-growth crystallographic planes limiting growths of individual dots. Completely selective GaAs growth within dielectric-mask openings at these small size-scales is also demonstrated. The uniformity of the dots within each array ranged from 6% for the larger dots to 16% for the smallest dots (normalized standard deviations of the areas of individual dots within each array).

6.1 Introduction

Semiconductor structures that exhibit quantum-confinement effects in three dimensions (quantum dots) have attracted considerable attention for their potential in improving optoelectronic devices as discussed earlier in chapter 5. For these optical effects to be observable at room temperature, the necessary dimensions are on the order of 10-20 nm. Many approaches to form these nanostructures (quantum dots) have been studied, including selective disordering [1] or physical patterning [2,3] of epitaxially-grown quantum-well materials, *in situ* strain-induced formation of epitaxial islands [4,5], and many others. Selective epitaxy, which refers to the laterally-controlled growth of epitaxial material within openings of a masking material, has also produced very promising results to date. In particular, highly-organized dot structures exhibiting excellent uniformity and good luminescence efficiency have been formed by selective epitaxy [6-8].

In this chapter, the successful formation of highly-uniform and densely-packed arrays of GaAs dots by selective epitaxy using diethylgallium chloride and arsine [9,10] is described. Imaged by atomic-force microscopy (AFM), the GaAs dots are as small as 15-20 nm in base diameter and 8-10 nm in height. Completely selective GaAs growth within dielectric-mask openings is also confirmed at these small size-scales using AFM. This is the first demonstration of selective epitaxial growth in dielectric-mask openings at these small size-scales [11].

6.2 Dot Formation by Selective Epitaxy

The substrates prepared for this study contained a 2 μm Si-doped $Al_{0.3}Ga_{0.7}As$ layer and a 10 nm undoped GaAs cap layer, both deposited by low-pressure organometallic vapor-phase epitaxy (OMVPE), on Si-doped (100) GaAs substrates. A dielectric masking layer of silicon nitride was deposited by plasma-enhanced chemical-vapor deposition on the substrates and then annealed under an arsine ambient at typical OMVPE growth conditions. The thickness of the annealed silicon-nitride layer was approximately 15 nm before lithographic patterning. 40 μm x 40 μm arrays of dot openings with center-to-center spacings of 100 nm were patterned into the silicon-nitride layer by high-resolution electron-beam lithography and reactive-ion etching in CF_4 plasma. The electron-beam dosages used for the lithography were varied to produce variations in the dot-opening sizes among different arrays.

The growths of the arrays of GaAs dots were performed in an AIXTRON 200/4 low-pressure horizontal-flow OMVPE reactor ("Reactor B" as described in chapter 2) with susceptor-disk rotation. Growth precursors for the organometallic chloride (III) and the hydride (V) were diethylgallium chloride (DEGaCl) and arsine (AsH_3) respectively. The DEGaCl-bubbler temperature was maintained at 17°C. The growth temperature was 700°C. The reactor-chamber pressure during growth was 200 mbar. Vapor-phase V/III ratio was maintained at >100. The patterned growth samples were annealed under an AsH_3/H_2 ambient at the growth temperature for 10 minutes prior to the actual growth. No dopant was intentionally introduced.

6.3 Characterization and Analysis by Atomic-Force Microscopy

Atomic-force microscopy (AFM) is based on sensing the microscopic forces between the tip of an extremely sharp stylus and a surface of interest. The interatomic forces induce the displacement of the stylus, and in its original implementation, a tunneling junction was used to detect the motion of a diamond stylus attached to an electrically-conductive cantilever beam [12]. Subsequently, optical interferometry was used to detect the cantilever deflection. By maintaining a constant force (constant cantilever deflection) between the stylus tip and a surface and by scanning the stylus over the surface, an image of the surface profile can be generated.

The current AFM [13,14], utilized for this work, uses a position-sensitive photodetector to detect the cantilever deflection, as depicted in figure 6.1. A laser beam is directed onto the back surface of the cantilever. The optical reflection of the laser beam off the cantilever changes direction as the cantilever is deflected by surface features of a sample. The optical reflection is detected by the position-sensitive photodetector, comprising two juxtaposed semicircular photodiodes. Cantilever deflection is measured as the difference between the output signals from these two photodiodes. For generating an image of the surface profile of a sample, a piezoelectric XYZ translator moves the sample and maintains a constant cantilever deflection, to provide a constant contact force between the stylus tip and the sample.

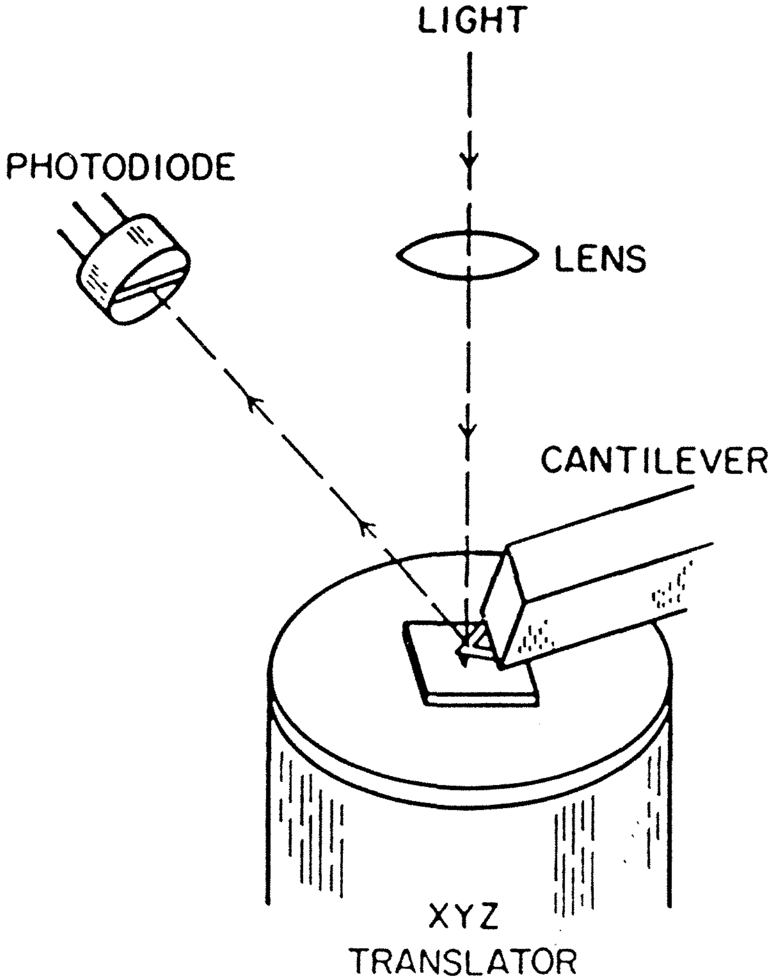

Figure 6.1. Schematic diagram of an atomic-force microscope using optical detection of cantilever deflection.

The arrays of GaAs dots were imaged by the AFM as described. The operating parameters for the AFM were optimized to image these small dot structures. The contact force chosen for the etch-sharpened-silicon AFM stylus tip was an empirical compromise between fast tip-wear and tip lift-off from the granular surface containing aciculate features. For the AFM tip to closely track these surface features, the electrical gain for tip feedback was maximized and slow scan rates and small scan areas were applied. Each AFM image took approximately 20 minutes to complete. The acquired AFM image data were plane-fitted to remove the effects of thermal drifts and small tilts from the samples and/or the AFM. No other image-processing procedures were applied to enhance the image data.

Plane views and three-dimensional views of the arrays of GaAs dots were generated using the AFM. Figure 6.2 contains three plane-view AFM images of the GaAs dots from different arrays. The apparent sizes of the dots are: (a) 22 nm, (b) 35 nm, and (c) 57 nm. Figure 6.3 contains two three-dimensional-view AFM images of the same arrays of GaAs dots from figure 6.2 (figure 6.3a corresponds to figure 6.2b and figure 6.3b to figure 6.2c). These AFM images of the arrays of GaAs dots illustrate that the dots are highly uniform and densely packed within each array. By analyzing the AFM image data, the areas of individual dots within each array were determined. The normalized standard deviations of the areas of individual dots were 16% for the array illustrated in Figure 6.2a, 10% for the array in Figure 6.2b, 8% for the array in Figure 6.2c, and 6% for the arrays with larger dots. In addition, these images confirm that the GaAs deposition is entirely selective under these growth conditions. No deposition occurred outside of the dielectric-mask openings.

After the initial AFM imaging, the samples were etched in a low-bias-voltage CF_4/O_2 plasma to remove the silicon-nitride layer. Figure 6.4 contains two three-dimensional-view AFM images of the arrays of GaAs dots after the removal of silicon nitride. The array in figure 6.4a corresponds to the array in figure 6.2a, and figure 6.4b to figure 6.2b.

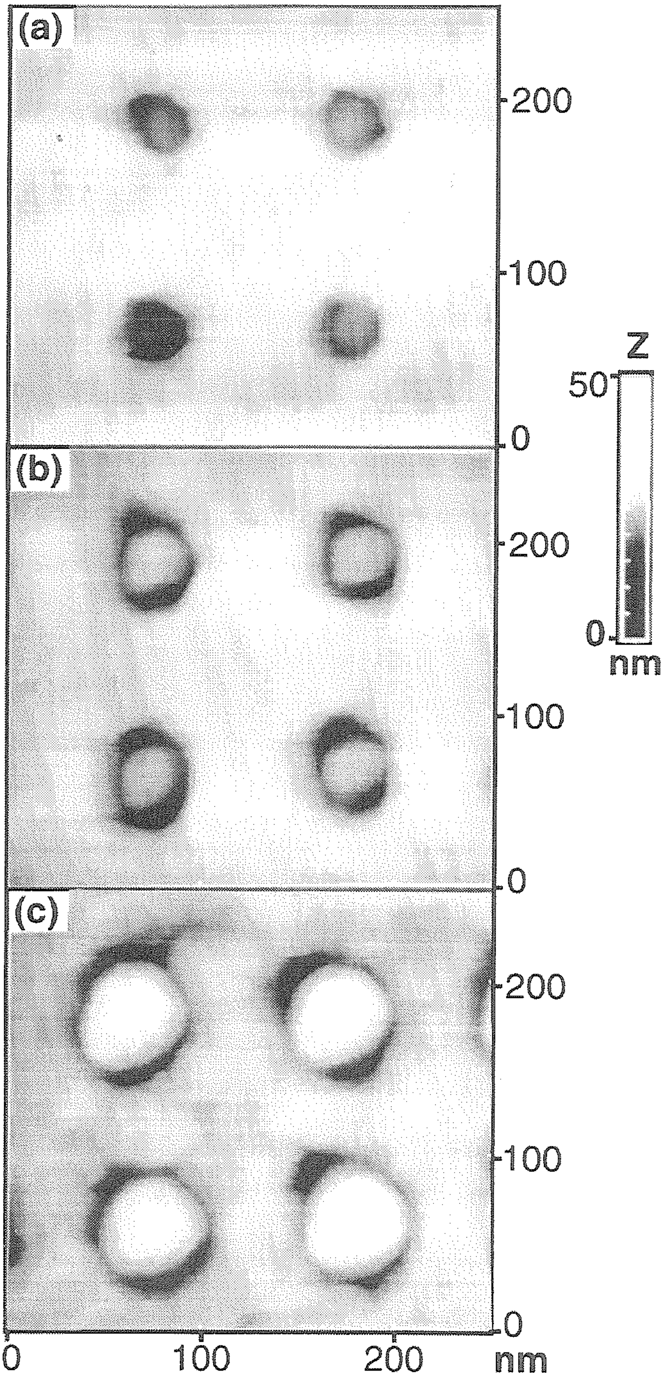

Figure 6.2. Atomic-force micrographs in plane view of arrays of (a) small, (b) medium, and (c) large GaAs dots after growth. The actual scan area is 500 nm x 500 nm. The height (Z) is represented by gray scale. The dot center-to-center spacing is 100 nm.

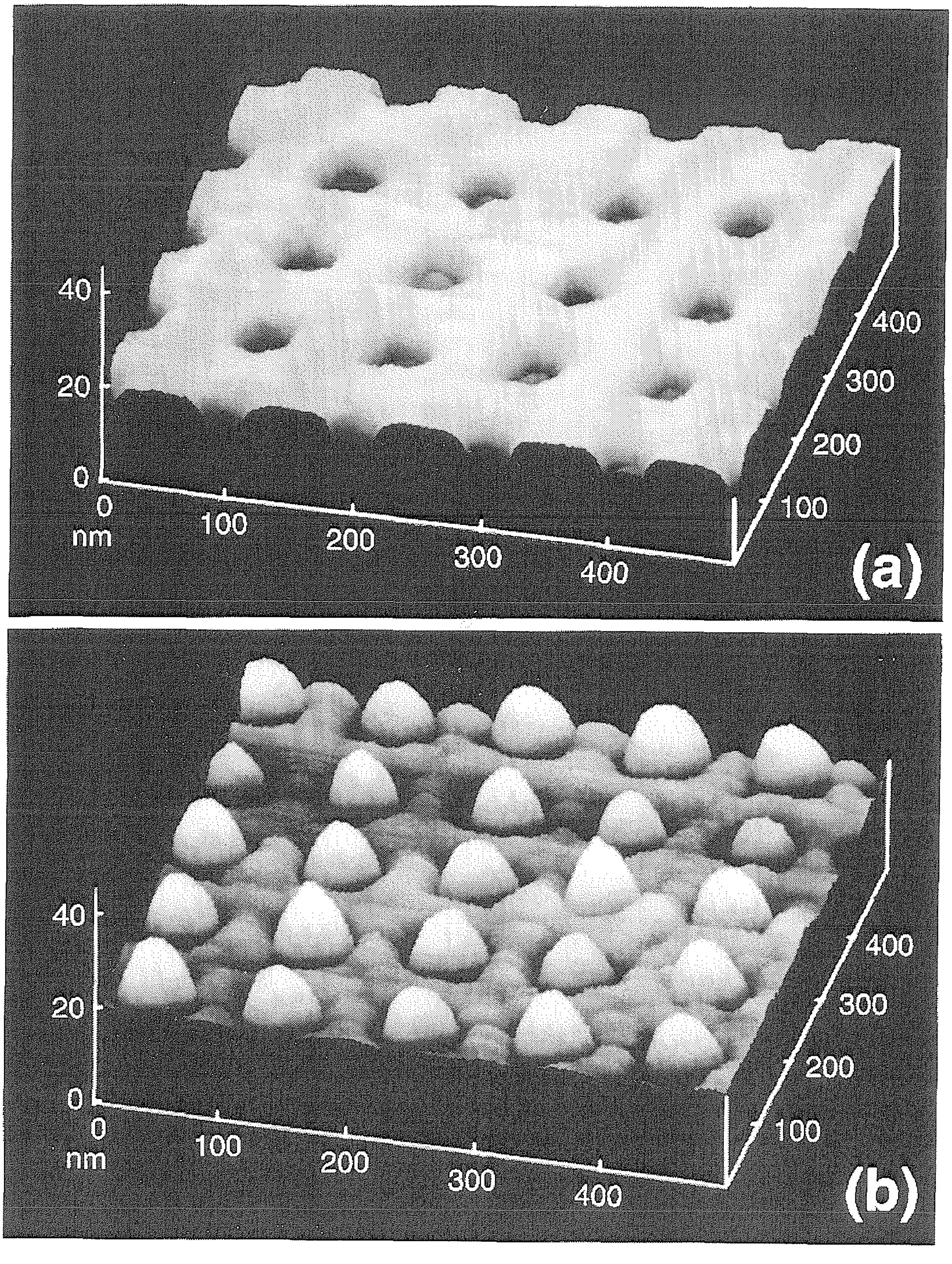

Figure 6.3. Atomic-force micrographs in three-dimensional view of arrays of (a) medium and (b) large GaAs dots after growth. The actual scan area is 500 nm x 500 nm and the height range is 40 nm.

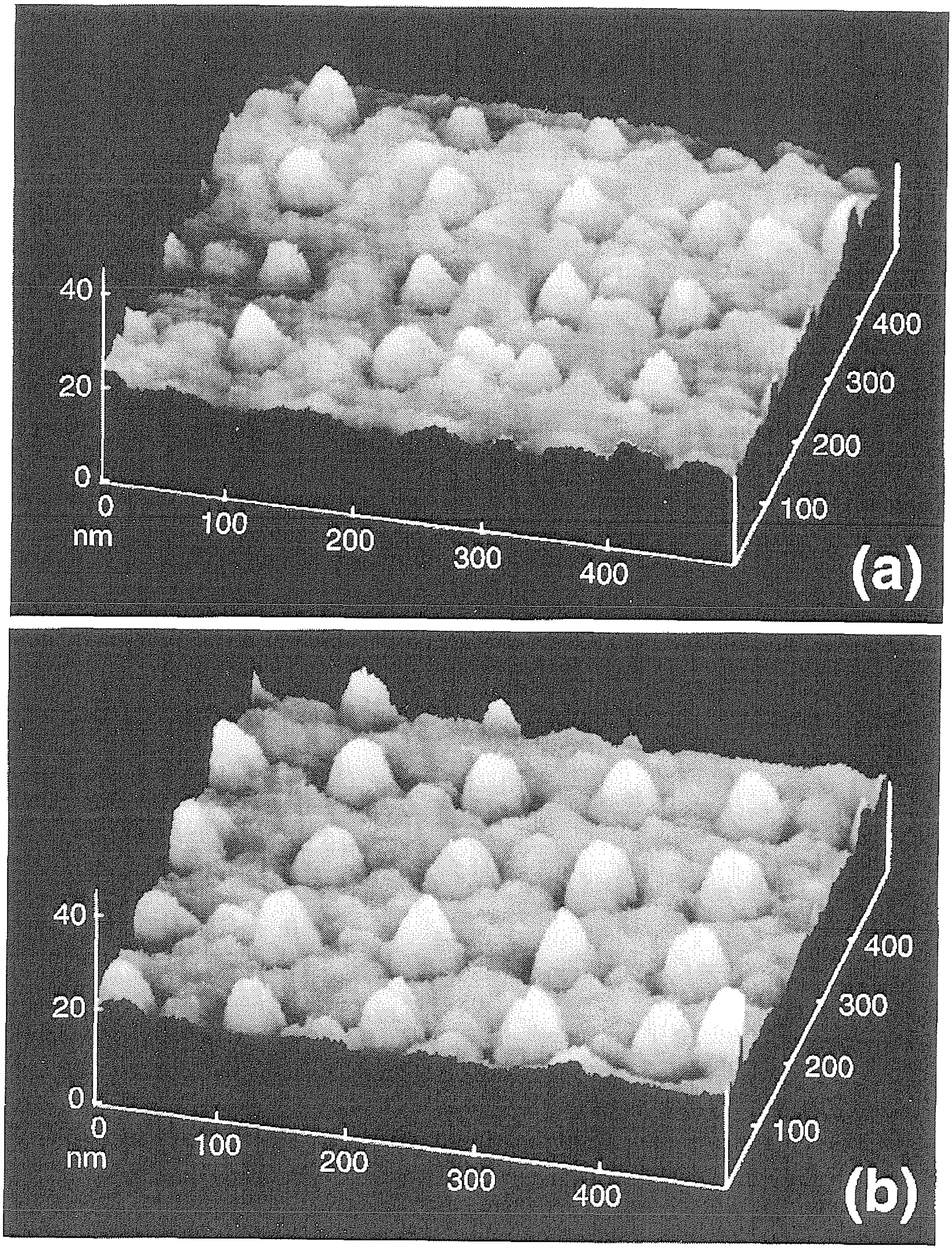

Figure 6.4. Atomic-force micrographs in three-dimensional view of arrays of (a) small and (b) medium GaAs dots after removal of silicon nitride. The actual scan area is 500 nm x 500 nm and the height range is 40 nm.

The apparent sizes of the dots are (a) 44 nm and (b) 55 nm. These images appear to be noisier than the previous images. Possible reasons for the noise include chemical contamination (a result of taking the samples off the AFM mount), uneven plasma etching, and/or surface roughening from the plasma etching.

The height and the base diameter of the GaAs dots, with the silicon-nitride layer removed, were measured to produce the plot in figure 6.5. A best-fit line is also drawn in this figure. The x-intercept of this line is not at zero base diameter, but instead at ~29 nm, indicating that the AFM tip is affecting the determination of the actual dot size. The inset on figure 6.5 illustrates how an idealized AFM tip with a radius of curvature R could affect the imaging of a small dot structure. The x-intercept of the best-fit line at ~29 nm corresponds reasonably well with the tip specifications from the manufacturer (tip radius of curvature of 10-30 nm) and tip-wear during scanning.

The slope of the best-fit line is ~0.48, indicating that the growth of the dots is self-limited, most likely by 45° planes or (110)-type crystallographic planes (0.476 converts to 43.6° facet angle from the horizontal plane), which are the slow-growth crystallographic planes previously observed in this growth process [9,10]. Corrected data, accounting for the AFM tip radius of curvature, indicate that the dots are as small as 15-20 nm in base diameter and 8-10 nm in height with the growth of individual dots self-limited by slow-growth crystallographic planes.

6.4 Conclusion

The formation of highly-uniform and densely-packed arrays of GaAs dots by selective epitaxy using diethylgallium chloride and arsine has been achieved. Atomic-force micrographs of the arrays of GaAs dots have been presented. Accounting for the limitations imposed by the AFM tip radius of curvature, the smallest GaAs dots fabricated are 15-20 nm in base diameter and 8-10 nm in height with slow-growth crystallographic planes limiting individual dot growth. Completely selective GaAs

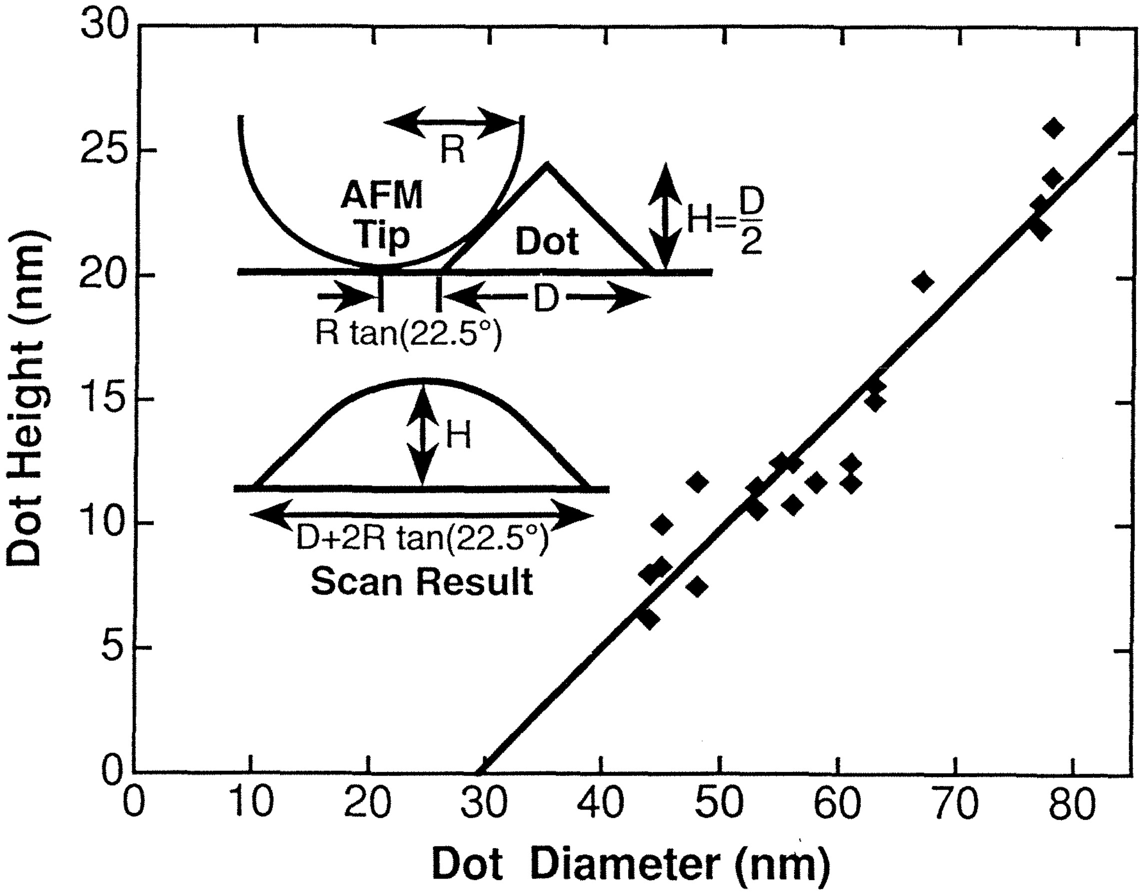

Figure 6.5. Plot of GaAs dot height versus base diameter, measured after silicon-nitride removal. A best-fit line of the measured data is also shown with x-intercept of 29.4 nm and slope of 0.476. *Inset*: idealized schematic illustrating the effect of an atomic-force microscope tip, with a radius of curvature R, on the imaging scan of a dot structure with 45° facets and base width D.

deposition within dielectric-mask openings is also confirmed at these small size-scales. The size uniformity of the dots within each array ranged from 6% for the larger dots to 16% for the smallest dots (normalized standard deviations of the areas of individual dots within each array).

Bibliography

[1] J. Cibert, P. M. Petroff, G. J. Dolan, S. J. Pearton, A. C. Gossard, and J. H. English, Appl. Phys. Lett. **49**, 1275 (1986).

[2] K. Kash, A. Scherer, J. M. Worlock, H. G. Craighead, and M. C. Tamargo, Appl. Phys. Lett. **49**, 1043 (1986).

[3] H. Temkin, G. J. Dolan, M. B. Panish, and S. N. G. Chu, Appl. Phys. Lett. **50**, 413 (1986).

[4] D. Leonard, M. Krishnamurthy, C. M. Reaves, S. P. Denbaars, and P. M. Petroff, Appl. Phys. Lett. **63**, 3203 (1993).

[5] J. Oshinowo, M. Nishioka, S. Ishida, and Y. Arakawa, Appl. Phys. Lett. **65**, 1421 (1994).

[6] J. A. Lebens, C. S. Tsai, K. J. Vahala, and T. F. Kuech, Appl. Phys. Lett. **56**, 2642 (1990).

[7] Y. D. Galeuchet, H. Rothuizen, and P. Roentgen, Appl. Phys. Lett. **58**, 2423 (1991).

[8] Y. Nagamune, S. Tsukamoto, M. Nishioka, and Y. Arakawa, J. Crystal Growth **126**, 707 (1993).

[9] T. F. Kuech, M. S. Goorsky, M. A. Tischler, A. Palevski, P. Solomon, R. Potemski, C. S. Tsai, J. A. Lebens, and K. J. Vahala, J. Crystal Growth **107**, 116 (1991).

[10] T. F. Kuech, M. A. Tischler, and R. Potemski, Appl. Phys. Lett. **54**, 910 (1989).

[11] C. S. Tsai, R. B. Lee, and K. J. Vahala, Mat. Res. Soc. Symp. Proc. **358**, *Microcrystalline and Nanocrystalline Semiconductors*, 969 (1995).

[12] G. Binnig, C. F. Quate, and C. Gerber, Phys. Rev. Lett. **56**, 930 (1986).

[13] G. Meyer and N. M. Amer, Appl. Phys. Lett. **53**, 1045 (1988).

[14] A. L. Weisenhorn, P. K. Hansma, T. R. Albrecht, and C. F. Quate, Appl. Phys. Lett. **54**, 2651 (1989).

Chapter 7

Facet-Modulation Selective Epitaxy - a Technique for Quantum-Well Wire Doublet Fabrication

The technique of facet-modulation selective epitaxy and its application to quantum-well wire doublet fabrication are described. Successful fabrication of wire doublets in the $Al_xGa_{1-x}As$ material system is achieved. The smallest wire fabricated has a crescent cross-section less than 140 Å thick and less than 1400 Å wide. Backscattered-electron images, transmission electron micrographs, cathodoluminescence spectra, and spectrally-resolved cathodoluminescence images of the wire doublets are presented.

7.1 Introduction to Facet-Modulation Selective Epitaxy

Semiconductor structures exhibiting quantum confinement in two or three dimensions have attracted considerable attention for their potential in improving optoelectronic devices [1,2] and in revealing new phenomena in solid state physics, such as polarization anisotropy in quantum wires [3]. Many approaches to fabricate these quantum-confinement structures have been studied. Already grown quantum well material has been physically patterned by a combination of lithography and etching [4-6] or has been selectively disordered by ion implantation [7] to achieve lateral confinement. *In situ* formation of nanostructures during epitaxial growths has also been studied. Migration-enhanced epitaxy on tilted substrates has exhibited quantum-confinement effects [8], and stimulated emission from quantum wires [9,10] has been demonstrated by performing organometallic vapor-phase epitaxy (OMVPE) growths on etched substrates. Wire and dot structures have been selectively grown on substrates covered with patterned dielectric masks [11-15]. The formation of crystal facets in single precursor chemistry (trimethyl) selective growth has also been studied as a potential method for quantum-well wire fabrication [16].

In this chapter, a new technique, facet-modulation selective epitaxy [17], is described and its application to quantum-well wire doublet fabrication in the $Al_xGa_{1-x}As$ material system is presented. The original concept that initiated this work is illustrated in figure 7.1. One or more alternating layers of GaAs and $Al_xGa_{1-x}As$ are deposited selectively within stripe openings of a dielectric mask on a substrate. The facets thus formed would create angular bends in the GaAs layers and form regions of quantum confinement located at the apexes of the selectively grown structures. Switching of the growth chemistries was not a part of the original concept. Due to limitations imposed by the OMVPE reactor utilized here ("Reactor A" as described in chapter 2), trimethyl-based precursor chemistry had to be used for $Al_xGa_{1-x}As$ growths. In order to maintain some selectivity, GaAs layers were grown using diethylgallium chloride (DEGaCl). As a result, the original concept evolved into facet-modulation selective epitaxy.

Facet-modulation selective epitaxy, as it is defined here, is the application of different *precursor chemistries to layers within a single growth to alter sequentially the appearance* of facets on a growing structure and to thereby form heterostructures of novel geometry. Two precursor chemistries are used here, a combination of diethylgallium chloride (DEGaCl) and arsine (AsH_3) for GaAs growth and a combination of trimethylaluminum (TMAl), trimethylgallium (TMGa) and arsine (AsH_3) for $Al_xGa_{1-x}As$ growth. The morphology of GaAs selective growth using DEGaCl and AsH_3 is dominated by the appearance of the {111} and {110} families of slow-growth crystallographic planes, with the appearance of a particular plane dependent on the growth temperature and the mask opening orientation [11,13,18]. The morphology of $Al_xGa_{1-x}As$ selective growth using TMAl, TMGa, and AsH_3 is similar, but the bounding planes include higher-index-

Fabrication of Quantum Wires by Facet-Defined Selective Epitaxy

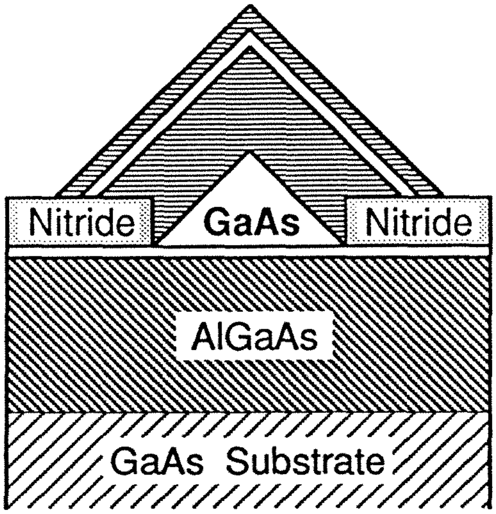

Single Quantum Wire

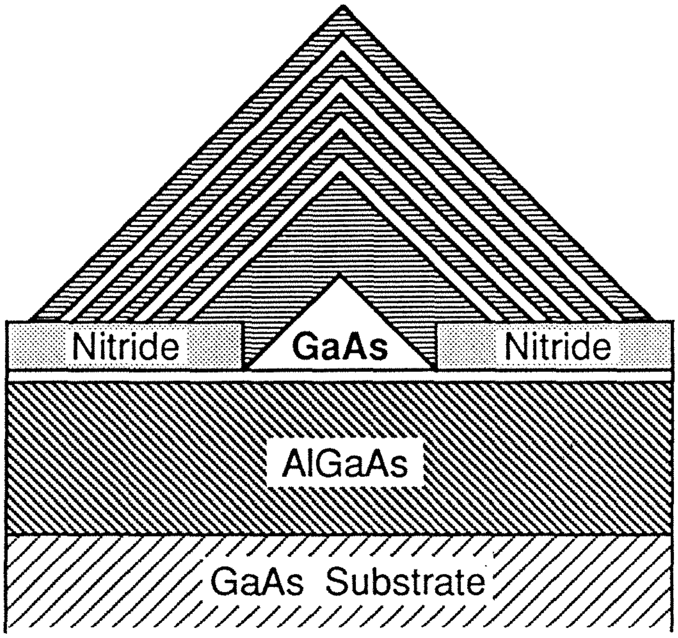

Multiple Quantum Wires

Figure 7.1. Schematic illustration of the original concept that preceeded facet-modulation selective epitaxy.

number planes (one or more indices greater than one) in addition to the {111} and {110} families of slow-growth planes.

One application of facet-modulation selective epitaxy is the fabrication of quantum-well wire doublets in a single growth as illustrated in figure 7.2. Using DEGaCl and AsH_3, a GaAs buffer layer bounded by the low-index-number facets is grown on a substrate covered with a stripe-patterned mask. Then an $Al_xGa_{1-x}As$ layer is grown using TMAl, TMGa, and AsH_3. Using DEGaCl and AsH_3 again, a GaAs wire doublet is formed as the higher-index-number $Al_xGa_{1-x}As$ facets are partially filled in by the GaAs growth attempting to form low-index-number GaAs facets. The wire doublet is buried *in situ* by another layer of $Al_xGa_{1-x}As$ growth to eliminate any free surface that would produce nonradiative-recombination centers. The width of the starting $Al_xGa_{1-x}As$ facets and the amount of GaAs deposited determine the size of the wires and the spacing between wires in a wire doublet. In the work presented here, successful fabrication of wire doublets by facet modulation selective epitaxy is achieved. Analysis of these wire doublet structures by backscattered-electron microscopy, transmission electron microscopy, and cathodoluminescence scanning electron microscopy is presented.

7.2 Substrate Preparation and Growth Conditions

The substrates used in this study contained a 2 μm Si-doped $Al_{0.4}Ga_{0.6}As$ layer, an undoped 100 nm $Al_{0.2}Ga_{0.8}As$ layer, and a 10 nm GaAs cap layer all deposited by OMVPE on Si-doped (100) GaAs substrates. The dielectric mask was 175 Å of silicon nitride deposited by plasma-enhanced chemical-vapor deposition. Arrays of 5-mm-long stripe openings, with stripe widths varying from 1 μm to 8 μm and center-to-center spacing between stripes of 250 μm, were patterned into the silicon-nitride mask by photolithography and reactive-ion etching in CF_4 plasma. The stripes were oriented along the $[01\bar{1}]$ direction.

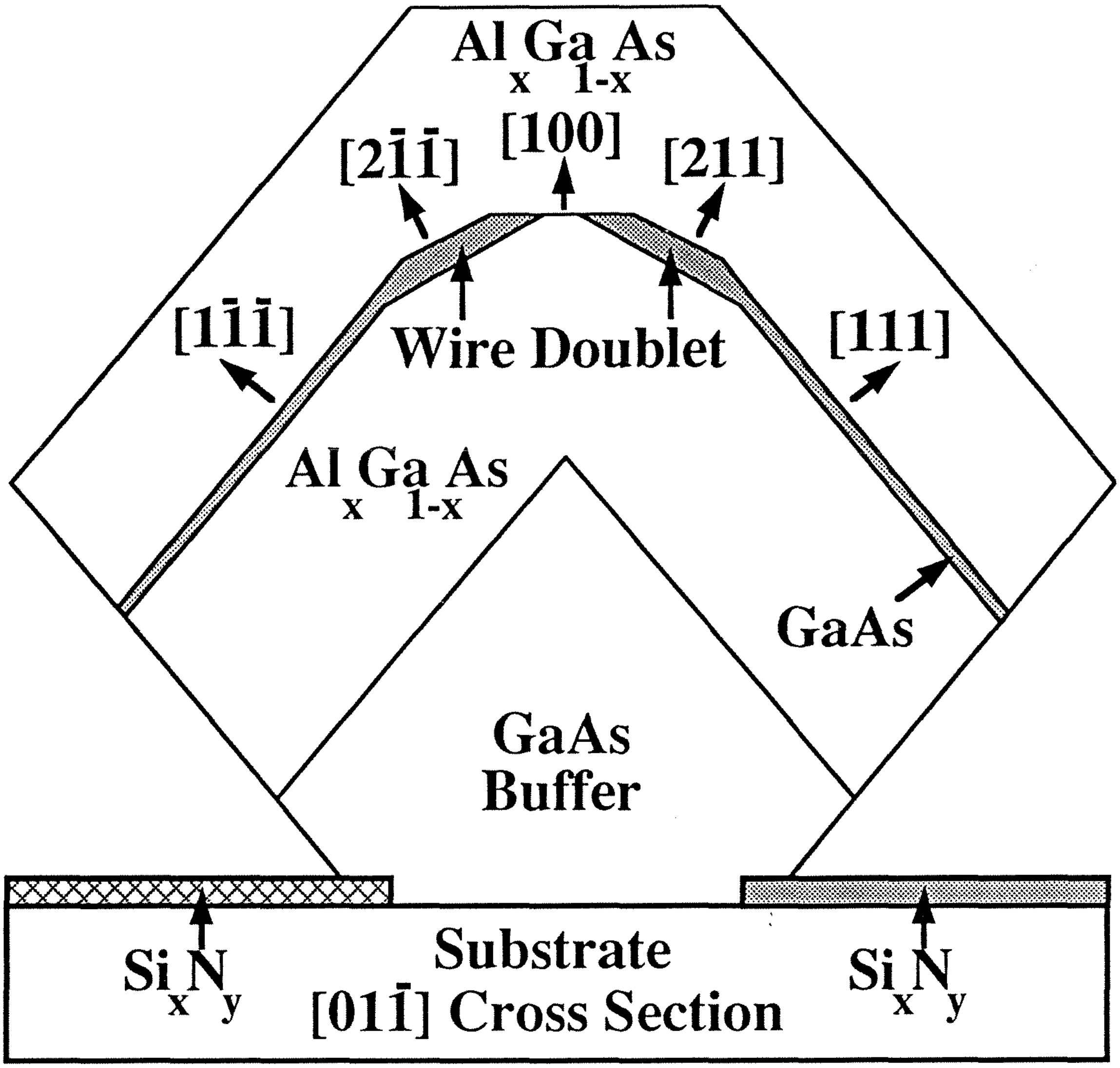

Figure 7.2. Schematic illustration of quantum-well wire doublet fabrication by facet-modulation selective epitaxy.

Sample growth was performed in an atmospheric-pressure OMVPE reactor with graphite susceptor temperature set to 730°C. Precursors for the buffer and quantum-well layers were DEGaCl and AsH_3. Precursors for the barriers were TMAl and AsH_3. AlAs barriers were chosen here to test the extreme case. Growth interruptions were placed between layers while AsH_3 flow was maintained. No dopant was intentionally introduced.

7.3 Characterization of Growth Samples

Figures 7.3a and 7.3b show a complete structure grown in a stripe opening 1.2 μm wide. The structure exhibits a facetted profile bounded mainly by the {111} family of planes. Measured along the [100] crystal direction from the substrate to the crystal apex, the growth consists of 1.3 μm of GaAs, 0.6 μm of AlAs, first quantum well, 0.4 μm of AlAs, second quantum well, 0.2 μm of AlAs, third quantum well, and finally 0.13 μm of AlAs. Measured along the [111] crystal direction on the (111) facet, the first, second, and third quantum wells are approximately 10, 20, and 5 nm thick respectively.

The wire doublet is shown clearly in figures 7.3c and 7.3d. The transmission electron micrograph in figure 7.3c reveals the higher-index-number {211}-type AlAs facets near the crystal apex. The micrograph also shows the growth of the third quantum well partially filling in the two {211}-type facets, thereby forming a wire doublet as predicted earlier. The two wires in the wire doublet are almost identical in shape and size. Both wires are approximately 140 Å thick at the center and 1400 Å wide, although the effective width of these wires is probably smaller than 1400 Å, because the wires have a tapered cross-section.

The luminescence properties of these wire-doublet structures were investigated by applying low-temperature cathodoluminescence (CL) scanning electron microscopy [19]. Figure 7.4 contains the CL spectra of the sample region near the wire doublet. Two distinct peaks appear in the CL spectra, one from the wire doublet at 690 nm and another

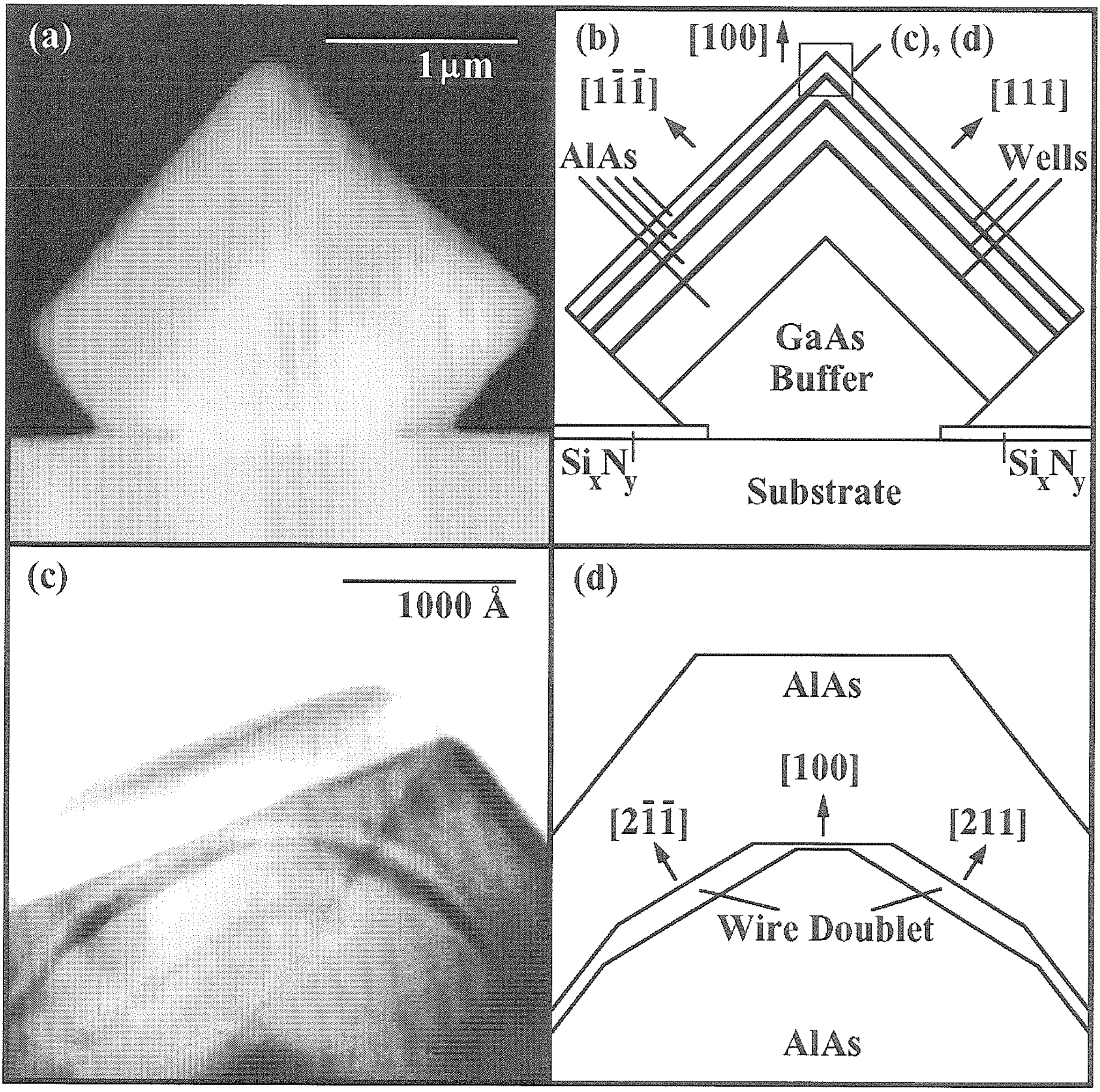

Figure 7.3. (a) $[01\bar{1}]$ cross-sectional backscattered-electron image of a complete structure grown by facet-modulation selective epitaxy. (b) Schematic illustration of the complete structure. (c) $[01\bar{1}]$ cross-sectional transmission electron micrograph of the wire doublet. (d) Schematic illustration of the wire doublet.

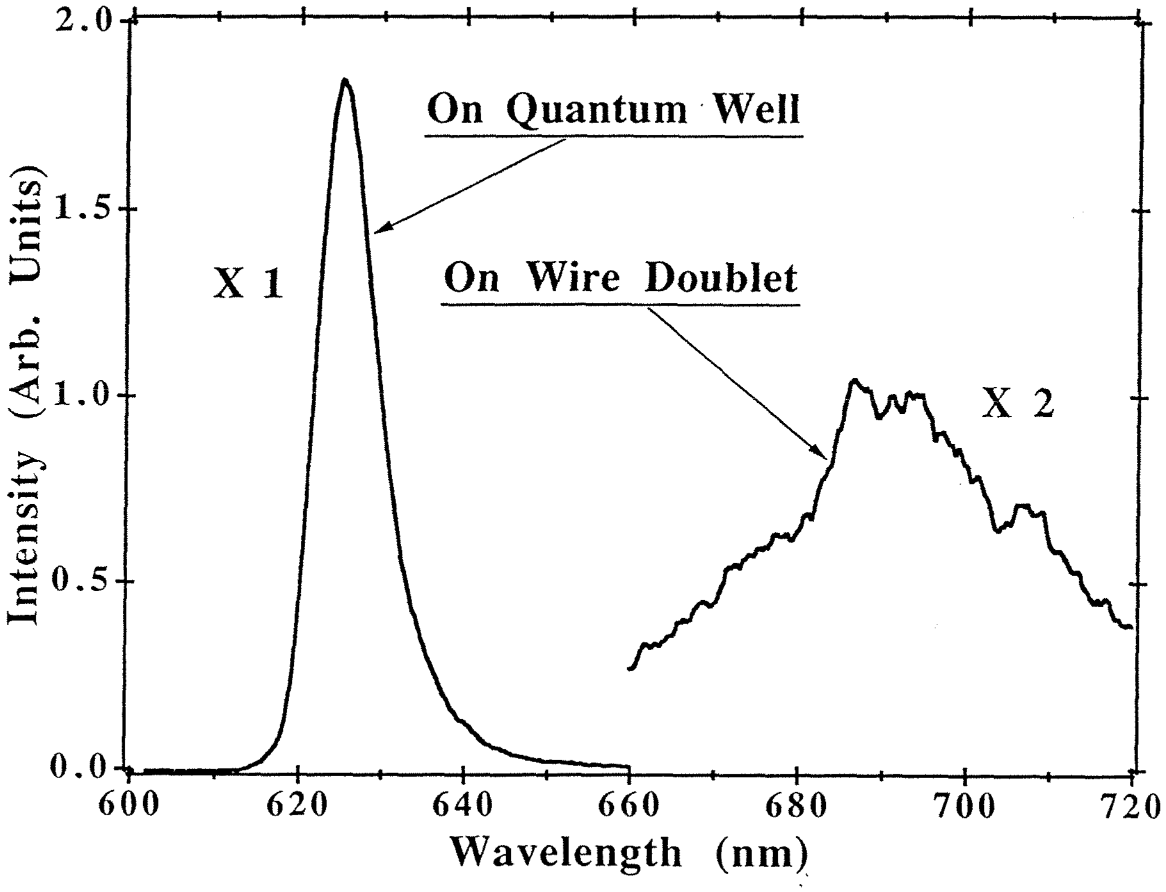

Figure 7.4. Cathodoluminescence spectra of the region near the wire doublet. The sample is at 14°K.

from the side-wall quantum wells at 625 nm. The red shifting of the wire-doublet peak with respect to the side-wall quantum-well peak is as expected from the thickness modulation seen in figure 7.3c. However, it is clear from the CL spectra and the thicknesses measured from figure 7.3c that the wire doublet and the side-wall quantum wells are most likely $Al_{0.2}Ga_{0.8}As$, not GaAs, because a 140 Å GaAs quantum well at 14°K luminesces at about 800 nm, not at 690 nm as shown in the CL spectra, and a 50 Å well luminesces at about 710 nm, not at 625 nm. Here the wire doublet is approximated as a quantum well because the widths of the wires are much larger than their thicknesses. The presence of aluminum is due to interlayer mixing, presumably caused by incomplete purging of TMAl before the DEGaCl growth had begun. The wire-doublet luminescence peak at 690 nm also appears broadened. Possible reasons for this broadening may include the fluctuations in the widths of the {211}-type AlAs facets, the surface roughness on the {211}-type AlAs facets, or some aluminum segregation resulting from mixing the two precursor chemistries.

Figures 7.5a-c are spectrally-resolved CL images of the wire-doublet structure in cross-section. Figure 7.5a is imaged at 625 nm where the side-wall quantum wells and the substrate $Al_{0.4}Ga_{0.6}As$ luminesce. Figure 7.5b is imaged at 693 nm, the luminescence peak of the wire doublet. Figure 7.5c is imaged at 820 nm, the luminescence wavelength of the buffer and substrate GaAs. The scanning electron micrograph in figure 7.5d shows the cross-section imaged in figures 7.5a-c. Figures 7.6a-d are spectrally-resolved CL images of structures seeded by stripe openings of different widths on the same sample. These images demonstrate the various configurations of wire doublets.

7.4 Conclusion

The technique of facet-modulation selective epitaxy and its application to the fabrication of quantum-well wire doublets have been described. Successful fabrication

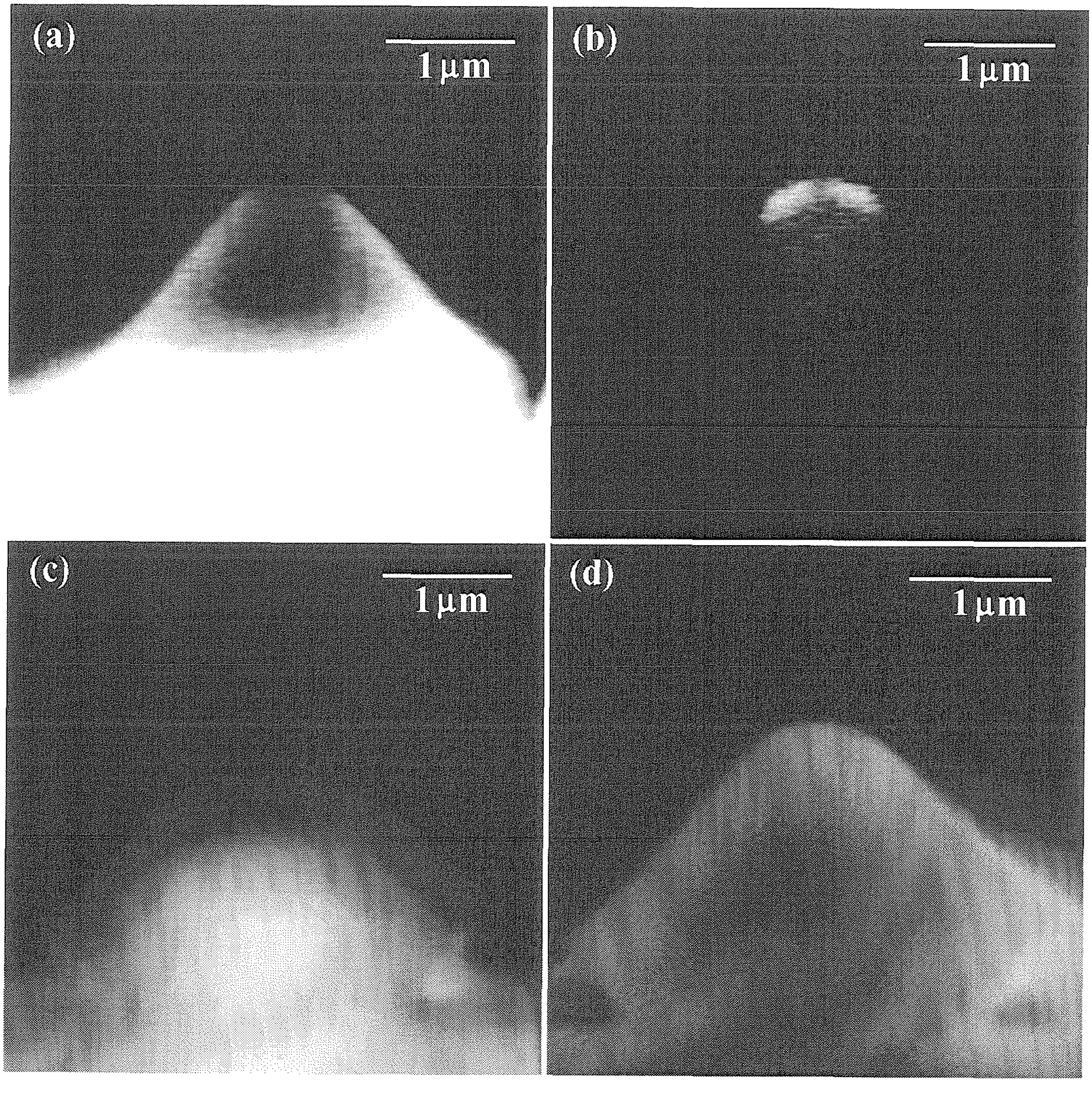

Figure 7.5. Spectrally-resolved cathodoluminescence images of a wire-doublet structure in cross-section. The sample is at 12°K, and the wavelengths are set at (a) 625 nm, (b) 693 nm, and (c) 820 nm. (d) Scanning electron micrograph of the same structure in cross-section.

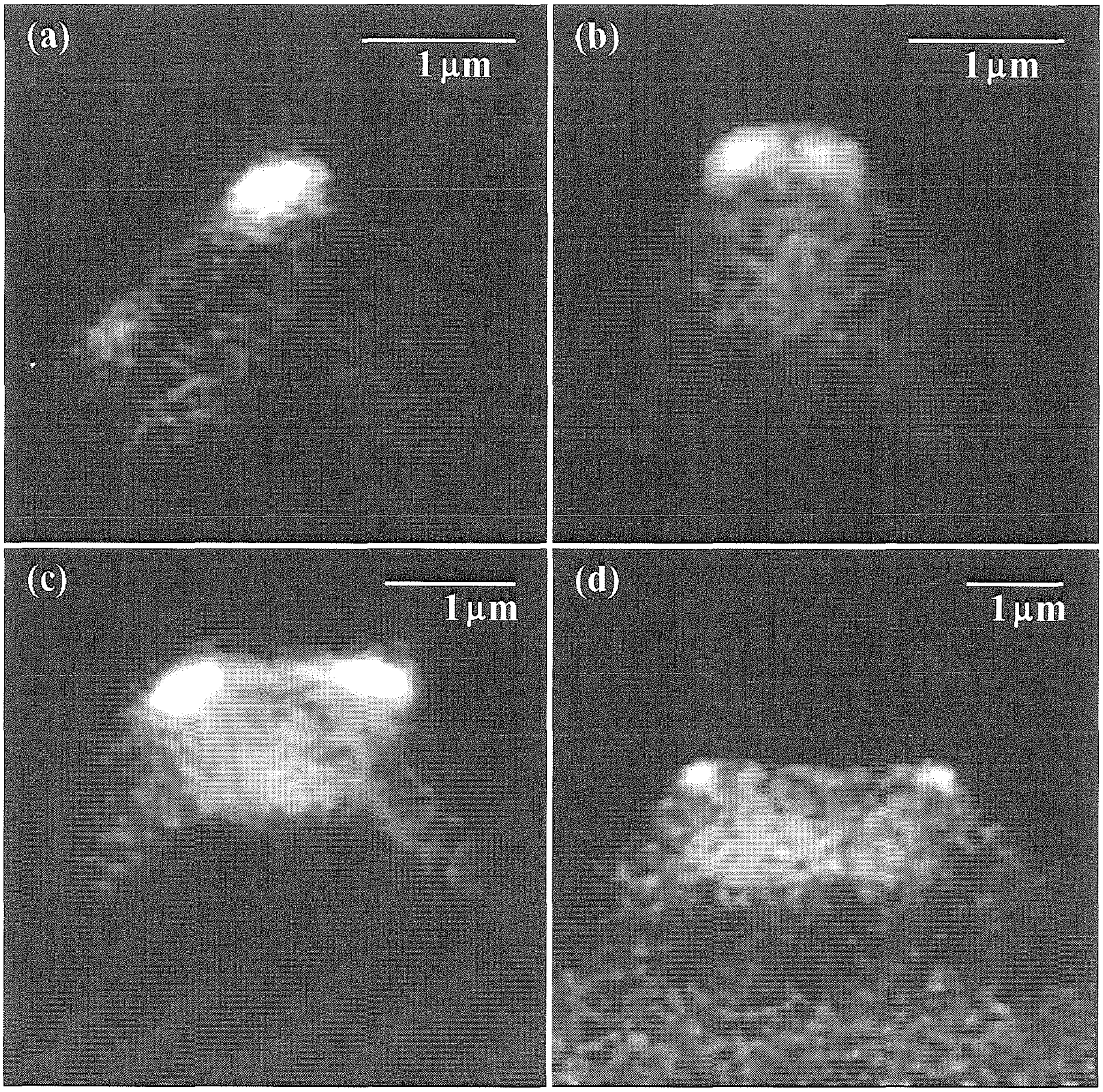

Figure 7.6. Spectrally-resolved cathodoluminescence images of different wire-doublet structures on the same sample. The sample is at 77°K, and the wavelengths are set at (a)-(c) 690 nm and (d) 680 nm.

of wire doublets in the $Al_xGa_{1-x}As$ material system has been achieved. The smallest wire fabricated has a crescent cross-section less than 140 Å thick and less than 1400 Å wide. By reducing the width of the starting $Al_xGa_{1-x}As$ facets and the amount of GaAs deposited, further reduction in wire size is possible. By doping the layers above and below the wire doublet p-type and n-type respectively, and by embedding the wire doublet in an $Al_xGa_{1-x}As$ optical waveguide, an injection laser may be fabricated. Other applications could also be explored, including the fabrication of quantum dots and the extensions of this technique to other material systems besides $Al_xGa_{1-x}As$, such as $In_xGa_{1-x}As$, by using analogous precursor chemistries [13].

Bibliography

[1] Y. Arakawa, K. Vahala, and A. Yariv, Appl. Phys. Lett. **45**, 950 (1984).

[2] M. Asada, Y. Miyamoto, and Y. Suematsu, IEEE J. Quantum Electron. **QE-22**, 1915 (1986).

[3] P. C. Sercel and K. J. Vahala, Appl. Phys. Lett. **57**, 545 (1990)

[4] K. Kash, A. Scherer, J. M. Worlock, H. G. Craighead, and M. C. Tamargo, Appl. Phys. Lett. **49**, 1043 (1986).

[5] H. Temkin, G. J. Dolan, M. B. Panish, and S. N. G. Chu, Appl. Phys. Lett. **50**, 413 (1987).

[6] B. I. Miller, A. Shahar, U. Koren, and P. J. Corvini, Appl. Phys. Lett. **54**, 188 (1989).

[7] J. Cibert, P. M. Petroff, G. J. Dolan, S. J. Pearton, A. C. Gossard, and J. H. English, Appl. Phys. Lett. **49**, 1275 (1986).

[8] M. Tsuchiya, J. M. Gaines, R. H. Yan, R. J. Simes, P. O. Holtz, L. A. Coldren, and P. M. Petroff, Phys. Rev. Lett. **62**, 466 (1989).

[9] E. Kapon, D. M. Hwang, and R. Bhat, Phys. Rev. Lett. **63**, 430 (1989).

[10] M. Walther, E. Kapon, C. Caneau, D. M. Hwang, and L. M. Schiavone, Appl. Phys. Lett. **62**, 2170 (1993).

[11] J. A. Lebens, C. S. Tsai, K. J. Vahala, and T. F. Kuech, Appl. Phys. Lett. **56**, 2642 (1990)

[12] T. Fukui, S. Ando, and Y. K. Fukai, Appl. Phys. Lett. **57**, 1209 (1990).

[13] T. F. Kuech, M. S. Goorsky, M. A. Tischler, A. Palevski, P. Solomon, R. Potemski, C. S. Tsai, J. A. Lebens, and K. J. Vahala, J. Crystal Growth **107**, 116 (1991)

[14] Y. D. Galeuchet, H. Rothuizen, and P. Roentgen, Appl. Phys. Lett. **58**, 2423 (1991)

[15] M. Nishioka, S. Tsukamoto, Y. Nagamune, T. Tanaka, and Y. Arakawa, J. Crystal Growth **124**, 502 (1992).

[16] S. Ando and T. Fukui, J. Crystal Growth **98**, 646 (1989)

[17] C. S. Tsai, J. A. Lebens, C. C. Ahn, A. Nouhi, and K. J. Vahala, Appl. Phys. Lett. **60**, 240 (1992).

[18] T. F. Kuech, M. A. Tischler, and R. Potemski, Appl. Phys. Lett. **54**, 910 (1989)

[19] M. E. Hoenk and K. J. Vahala, Rev. Sci. Instrum. **60**, 226 (1989)

Chapter 8

Visible-Wavelength Vertical-Cavity Surface-Emitting Laser by OMVPE

The development of OMVPE epitaxial layers for a visible-wavelength vertical-cavity surface-emitting laser (VCSEL) is presented. Passive fabry-perot cavities with $Al_{0.5}Ga_{0.5}As/AlAs$ $\lambda/4$-stack mirrors were grown as test structures for mirror calibration. The defect density of the mirror layers was reduced to a negligible level by optimizing gas-switching sequences during OMVPE growth. Transmission electron micrographs and reflectance measurements of one calibration cavity are presented. $In_{0.5}Ga_{0.5}P/In_{0.5}Al_{0.5}P$ heterostructure p-n diodes, processed by using the actual fabrication procedures for VCSEL, were prepared as an intermediate test structure for the $In_{0.5}Ga_{0.5}P/In_{0.5}Al_{0.2}Ga_{0.3}P/In_{0.5}Al_{0.5}P$ multiple-quantum-well (MQW) active region. Electroluminescence spectrum of the p-n diode is presented. Test structures containing only the MQW active region were grown. The defect density of the MQW active region was also reduced to a negligible level by optimizing the gas-switching sequences. Full structures containing both the mirror and the MQW active region were grown. Optical micrographs of these full structures are also presented.

8.1 Introduction to Visible-Wavelength VCSEL

Visible-wavelength vertical-cavity surface-emitting lasers (VCSEL) have attracted considerable interest because of their surface-normal operation, potential for extremely low threshold currents, and ease of integrating multiple VCSEL into closely spaced one-and two-dimensional arrays or integrating with other devices such as transistors. In addition, the visible-wavelength operation of the VCSEL would allow two-dimensional arrays for plastic-fiber-based optical communications, for high-brightness optical displays or projectors, and for replacing conventional light-emitting diodes (LED) and He-Ne lasers.

Recently, photopumped [1,2] and electrically-injected [3,4] lasing of visible-wavelength VCSEL has been demonstrated. As seen in figure 8.1a, the overall structure of the demonstrated VCSEL devices comprised a p-type top mirror with alternating $Al_{0.5}Ga_{0.5}As/AlAs$ $\lambda/4$ layers, an active region of $In_{0.5}Ga_{0.5}P/In_{0.5}Al_xGa_{0.5-x}P/In_{0.5}Al_{0.5}P$ multiple-quantum-well (MQW), a n-type bottom mirror with alternating $Al_{0.5}Ga_{0.5}As/AlAs$ $\lambda/4$ layers, and the necessary electrical contact metallization and isolation. Proton implantation is illustrated as one possible method of isolating the device by making the p-type mirror layers non-conductive surrounding the device. This structure suffers from high series resistance in the top contact because of the long circuitous conduction path through the thick p-type mirror (up to 3 μm thick).

An alternative VCSEL structure is shown in figure 8.1b which eliminates the high series resistance in the top contact. A SiO/SiN dielectric top mirror is utilized in place of the $Al_{0.5}Ga_{0.5}As/AlAs$ p-type top mirror. Annular metal contact is made directly to the active region of $In_{0.5}Ga_{0.5}P/In_{0.5}Al_{0.2}Ga_{0.3}P/In_{0.5}Al_{0.5}P$ MQW. The device junction is entirely encircled by dielectric material. This alternative VCSEL structure would have low series resistance and high modulation speed. In addition, the thickness variations in the OMVPE epitaxial layers can be compensated by adjusting the thicknesses of the SiO/SiN top mirror, since the device structure is formed in two separate steps. This chapter presents the development of OMVPE epitaxial layers toward achieving this alternative VCSEL structure.

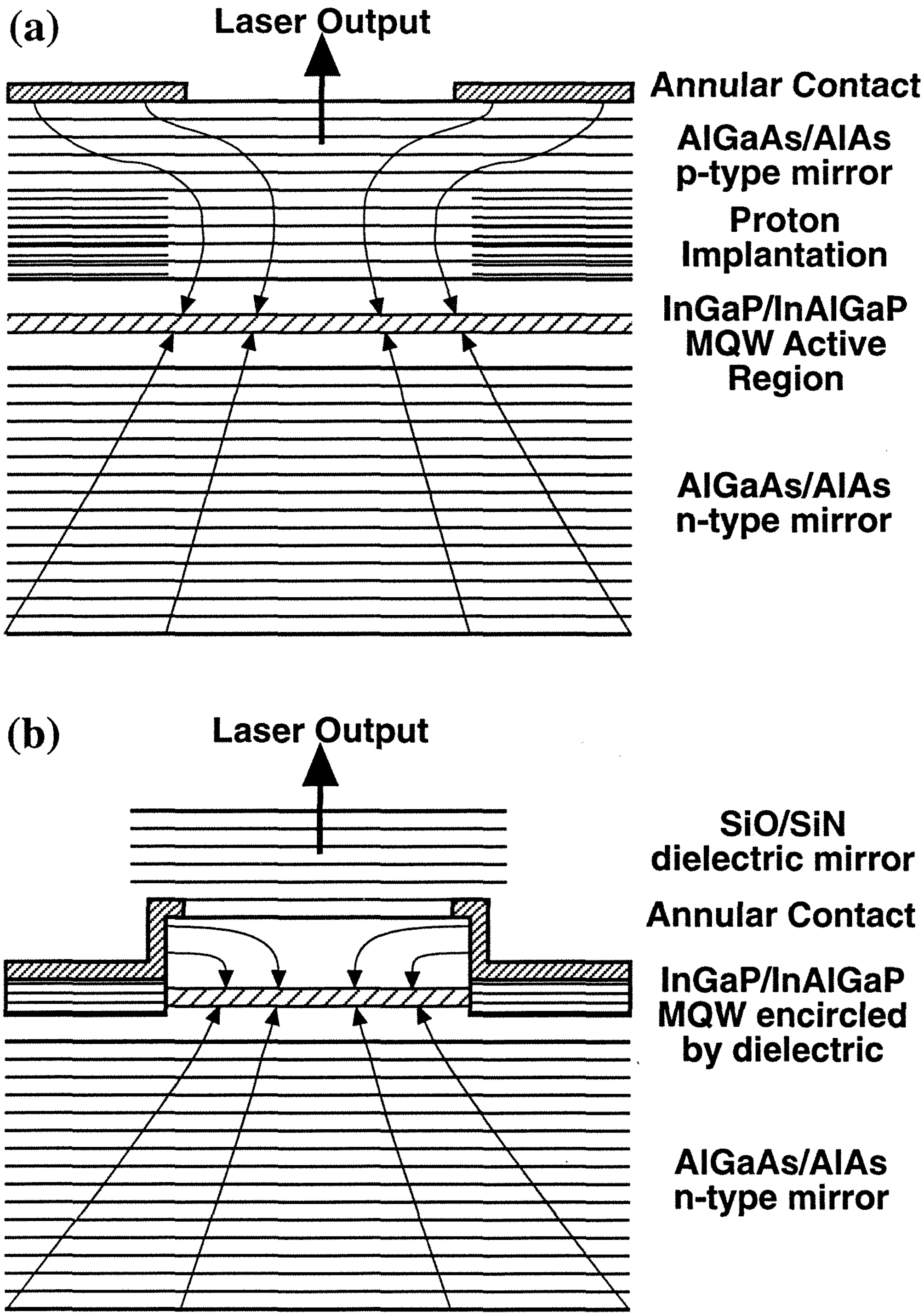

Figure 8.1. Schematic illustration of a conventional VCSEL structure (a) and an etched VCSEL structure with dielectric top mirror (b).

8.2 Growth and Characterization of λ/4-Stack Mirror

The VCSEL structures pose extremely challenging requirements for any epitaxial growth technique. The high optical efficiency required in the small (~ 1 μm thick) laser cavity demands essentially perfect material with precise control of layer thickness and composition. The challenges are compounded by the many layers (up to over 100) and thick epitaxial growths (up to 8 μm) which magnify greatly any tiny imperfections in the epitaxial growth process. Epitaxial problems which are considered minor perturbations in conventional device structures become major obstacles to the successful operation of a VCSEL.

In order to establish the proper OMVPE growth parameters for the λ/4-stack mirror, several passive fabry-perot cavities, each comprising one $Al_{0.5}Ga_{0.5}As$ λ/2 layer placed in between two $Al_{0.5}Ga_{0.5}As/AlAs$ λ/4-stack mirrors, were grown using conventional OMVPE precursors in "Reactor B" as described in chapters 2 and 4. In this case, the target λ is in the range of 670-680 nm. The complete test structure is illustrated in figure 8.2. The top mirror was capped by a thin layer of GaAs (10 nm) to prevent oxidation of the mirror.

The reflectance of the passive fabry-perot cavities were measured in an optical setup containing a broad-band white-light source and an optical spectrometer with an attached photomultiplier tube. In figure 8.3, the measured reflectance of one cavity is plotted with a solid line. The measured cavity-resonance peak is centered at 674 nm, well within the target wavelength range. The calculated reflectance of the same cavity is also plotted. The calculated reflectance was obtained by computer simulation using published material parameters [5,6] in a conventional characteristic-matrix model [7]. The measured and the calculated reflectance correspond qualitatively. Some of the factors preventing the exact correspondence between the two include measurement errors in the optical setup, the use of a simulation model without absorption (GaAs is absorbing at the measured wavelengths), and inaccurate layer thicknesses used in the

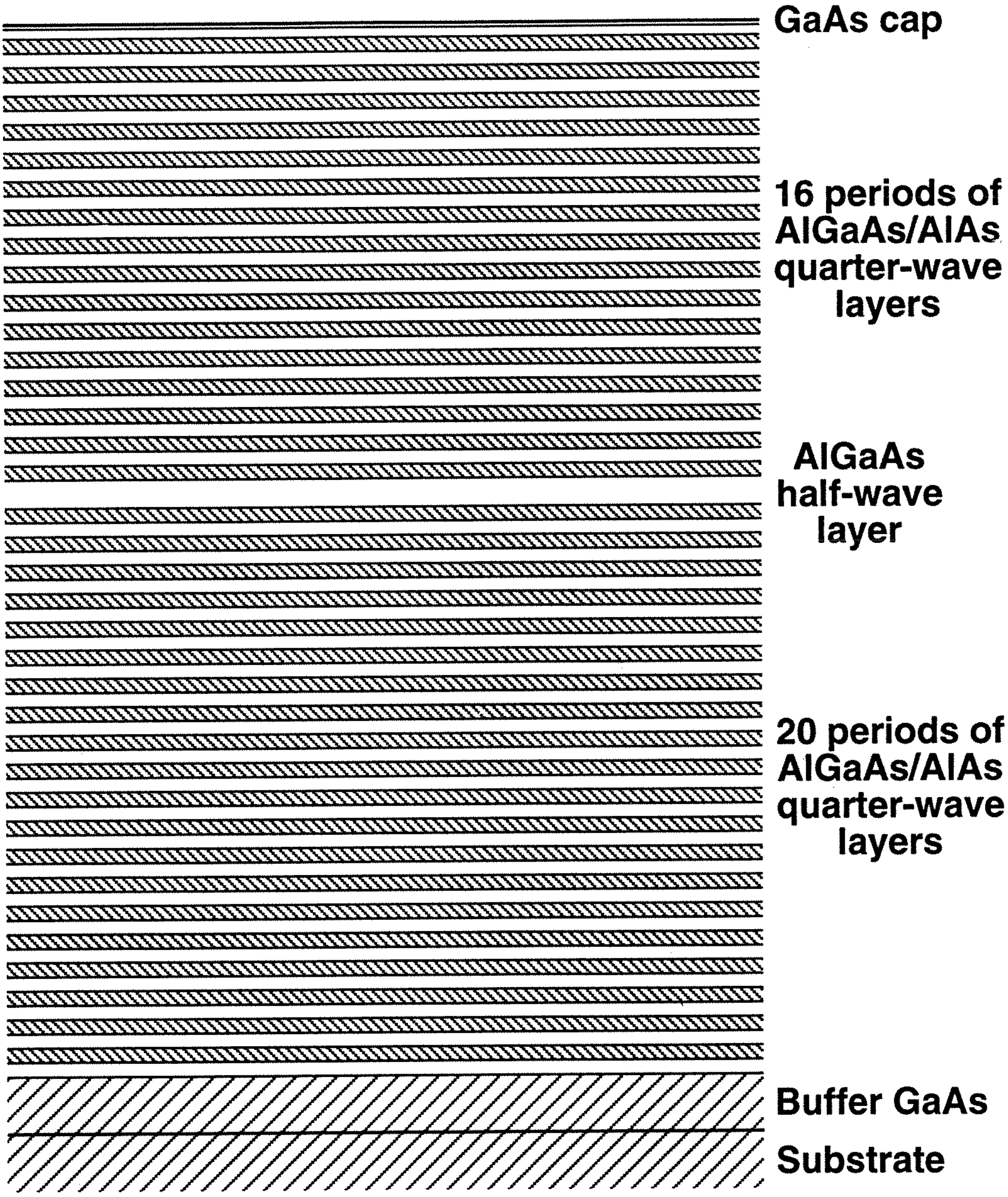

Figure 8.2. Schematic illustration of the passive fabry-perot cavity used as a test structure for mirror calibration.

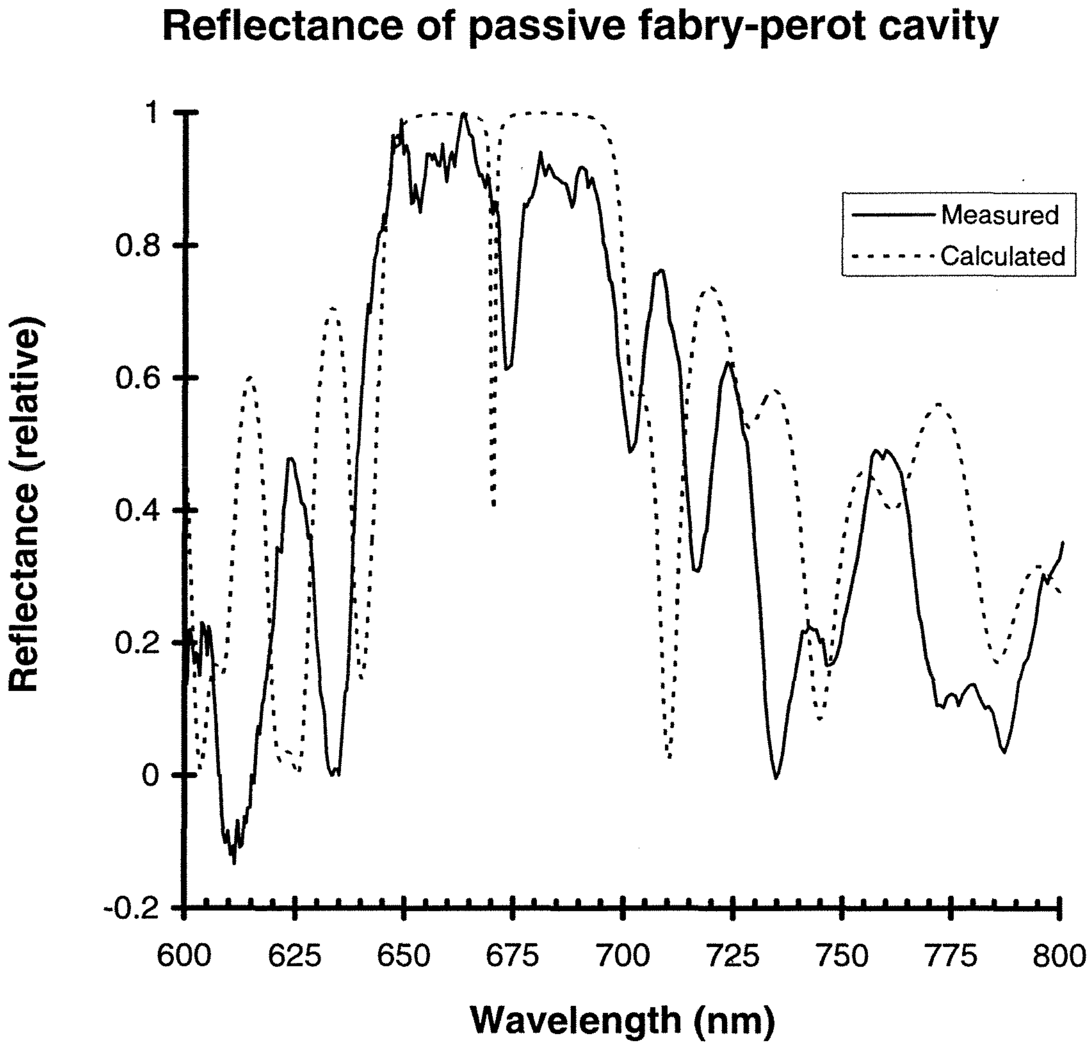

Figure 8.3. Plot of the measured and calculated reflectance of the passive fabry-perot cavity illustrated in figure 8.2.

simulation model. Further refinement of the calculated reflectance is possible by using a more comprehensive model with independently and accurately determined layer thicknesses.

The surface defect-density of the $\lambda/4$-stack mirror was reduced to a negligible level by optimizing gas-switching sequences during OMVPE growth. Several test structures, each containing only 10 periods of $Al_{0.5}Ga_{0.5}As/AlAs$ $\lambda/4$ layers, were grown to optimize the gas-switching sequences. Optical micrographs at 680X of the initial and the final test structures are seen in figures 8.4a and 8.4b respectively. For figure 8.4b, the single defect, seen at the center, had to be located specifically, since the defect density was so low. The number of surface defects was reduced dramatically by minimizing flow-rate changes during layer-switching transitions in the OMVPE growth process.

Cross-sectional transmission electron micrographs (TEM) of the $\lambda/4$-stack mirror are shown in figures 8.4c at 52,000X and 8.4d at 122,000X. These micrographs show that the layers in the $\lambda/4$-stack mirror are uniform and well-defined with extremely abrupt transitions between adjacent layers. The outer edges of the AlAs layers (lighter color) appear oxidized as a result of exposure to atmospheric oxygen.

8.3 Growth and Characterization of MQW Active Region

$In_{0.5}Al_xGa_{0.5-x}P$ materials [8] lattice-matched to GaAs are utilized in the active regions of visible-wavelength VCSEL structures. Conventional OMVPE precursors are employed here in the growth of these materials. A precise match in the lattice constants is required for acceptable growths of these materials. The differences in lattice constants between the $In_{0.5}Al_xGa_{0.5-x}P$ materials and the GaAs substrate are determined by x-ray diffractometry. For this study, the relative mismatch measured on materials grown immediately after calibration is typically less than 2×10^{-4} ($\Delta a/a$). Variations in the material composition and the lattice constant usually result from drifts in the vapor

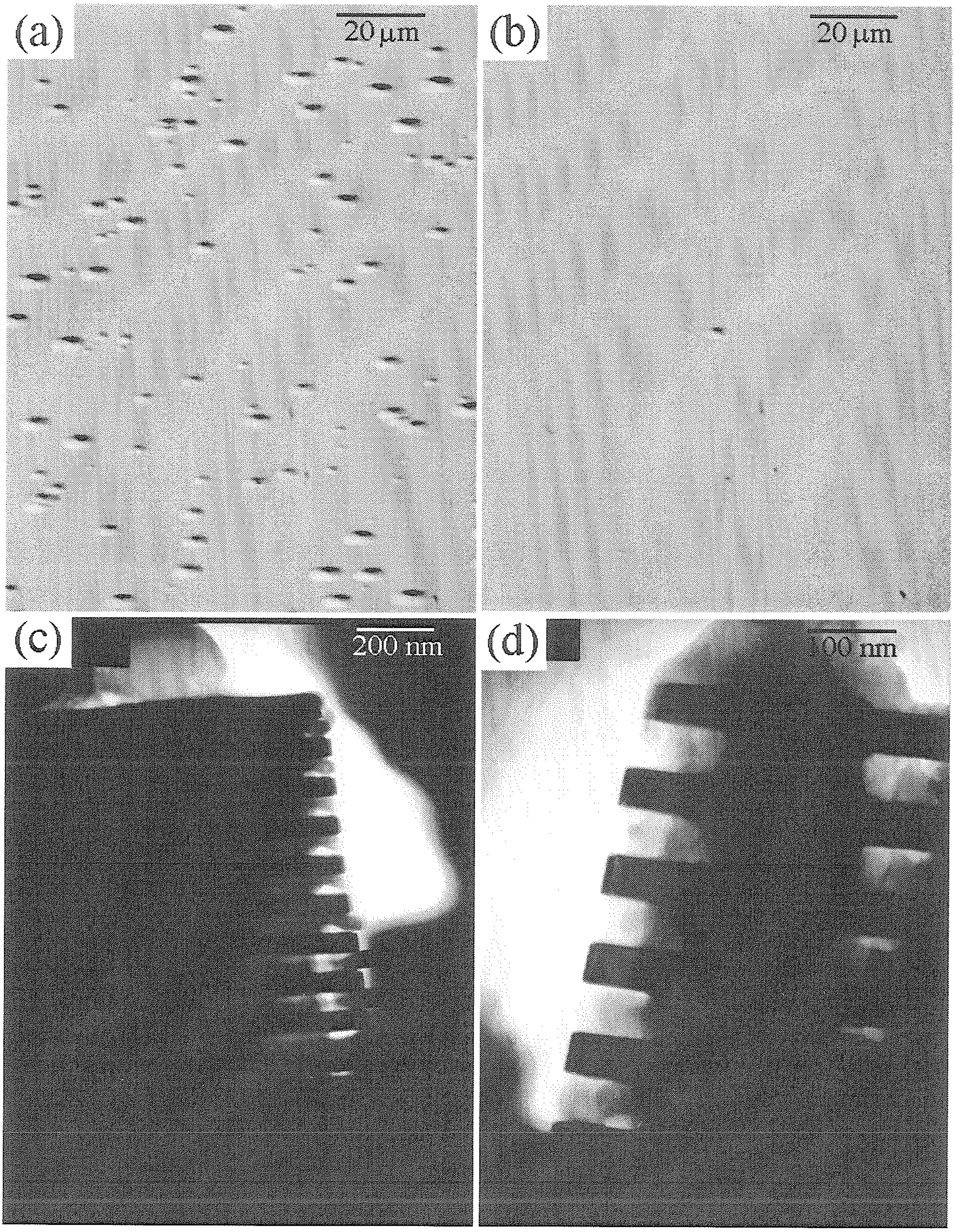

Figure 8.4. Optical micrographs at 680X of the initial (a) and the final (b) test structures for growth optimization of the mirror. Also shown are cross-sectional transmission electron micrographs of the mirror at 52,000X for (c) and 122,000X for (d).

pressure of the trimethylindium (TMIn) source, because TMIn is utilized in the form of a solid. The total surface area of the solid will change gradually as the TMIn source is consumed in the OMVPE growth process.

For electrically-injected VCSEL devices, p-type and n-type dopants are also necessary. Zn from diethylzinc [9] and Si from silane [10] are used as p-type and n-type dopants respectively. The actual doping level is measured by an electrochemical C-V profiler. The test sample is mounted next to a fluid cell containing the appropriate electrolyte. The electrolyte forms a Schottky junction with the sample surface. The Schottky junction is reverse-biased for C-V measurements to determine the doping levels. The same electrolyte is also used as an etchant to remove thin layers from the sample surface after each measurement. A depth profile of the doping levels within the sample is generated by this technique. In this study, the nominal doping levels used in the layers ranged from 10^{17} to $10^{18}/cm^3$, with higher doping levels used for the metallization contact layers.

$In_{0.5}Ga_{0.5}P/In_{0.5}Al_{0.5}P$ heterostructure p-n diodes, processed by using the actual fabrication procedures for VCSEL, were prepared as an intermediate test structure for the VCSEL active region. The heterostructure p-n diodes comprised an undoped 100 nm-thick $In_{0.5}Ga_{0.5}P$ layer placed in between a p-type 1 μm-thick $In_{0.5}Al_{0.5}P$ layer and a n-type 1 μm-thick $In_{0.5}Al_{0.5}P$ layer, all grown on a GaAs substrate. A heavily-doped p-type 200 nm-thick $In_{0.5}Ga_{0.5}P$ layer was grown on the very top of the structure to reduce electrical contact resistance.

Optical micrographs of the completed diodes are shown in figures 8.5a at 380X and 8.5b at 95X. The actual p-n junctions are the circular mesas seen in the micrographs. The speckled regions are the electrical interconnections and contact pads. The overall structure is similar to the one illustrated in figure 8.1b with the elimination of the top and the bottom mirrors and the substitution of the MQW active region with the $In_{0.5}Ga_{0.5}P/In_{0.5}Al_{0.5}P$ heterostructure.

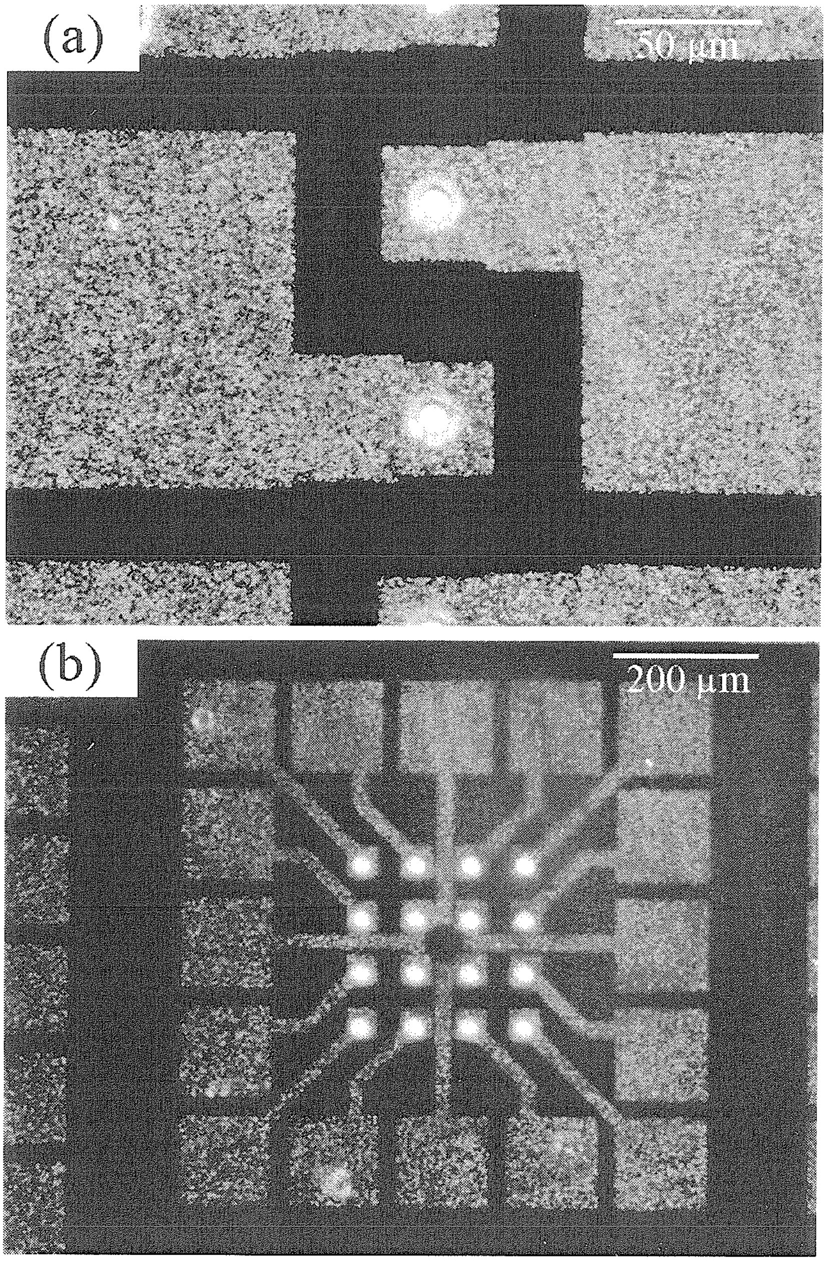

Figure 8.5. Optical micrographs of $In_{0.5}Ga_{0.5}P/In_{0.5}Al_{0.5}P$ heterostructure p-n diodes at 380X for (a) and 95X for (b).

Strong electroluminescence was obtained from the heterostructure p-n diodes. The electroluminescence spectrum of a heterostructure diode is shown in figure 8.6. The luminescence peak is at 685 nm. The heterostructure diode was electrically excited with 500 μs-duration constant-voltage pulses with 30 kHz repetition rate. The peak voltage is set at 6.2 V. The electroluminescence can be observed directly by the eye as an intense deep-red glow coming from a very small point. Continuous electrical excitation was not possible due to device heating. The electrical contact metallization would start to bubble and eventually self-destruct when continuous high voltage (> 5 V) was applied. The high excitation voltage required and the device heating were attributed to two factors. First, the p-type $In_{0.5}Al_{0.5}P$ layer was doped too lightly (low $10^{17}/cm^3$) which resulted in high series resistance and caused considerable device heating. Second, the metallization for the electrical contact was highly resistive due to rough surface morphology that had resulted from incorrect etching conditions during sample processing. For a few of the devices tested, electrical arcing was actually observable in the metallization as random blue flashes. The speckled morphology of the metallization is clearly visible in figure 8.5.

After the successful demonstration of electroluminescence from the $In_{0.5}Ga_{0.5}P$/ $In_{0.5}Al_{0.5}P$ heterostructure p-n diode, test structures containing the multiple-quantum-well (MQW) active region were grown. The MQW active region comprised three undoped 80Å-thick $In_{0.5}Ga_{0.5}P$ layers separated by four undoped 60Å-thick $In_{0.5}Al_{0.2}Ga_{0.3}P$ layers. These layers are placed in between a p-type 130 nm-thick $In_{0.5}Al_{0.5}P$ layer and a n-type 130 nm-thick $In_{0.5}Al_{0.5}P$ layer, all grown on a n-type GaAs substrate. A p-type 430 nm-thick $In_{0.5}Al_{0.2}Ga_{0.3}P$ layer followed by a heavily-doped p-type 15 nm-thick $In_{0.5}Ga_{0.5}P$ layer were grown on the very top of the structure to complete the MQW active region. Cross-sectional TEM micrograph at 122,000X of the MQW active region is shown in figure 8.7d. Here the three $In_{0.5}Ga_{0.5}P$ wells and the four $In_{0.5}Al_{0.2}Ga_{0.3}P$ barriers can be seen clearly in the center of the micrograph.

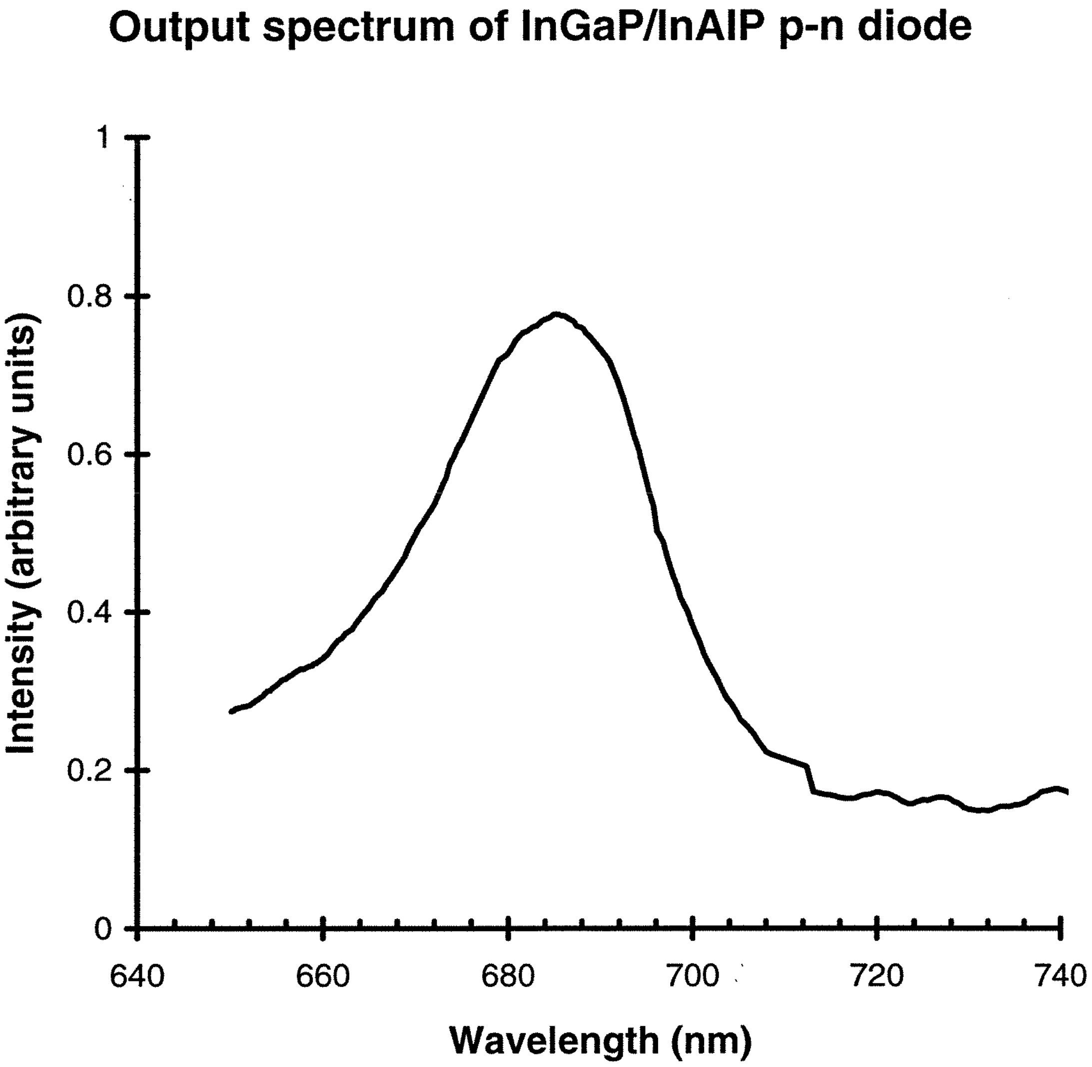

Figure 8.6. Electroluminescence spectrum of the $In_{0.5}Ga_{0.5}P/In_{0.5}Al_{0.5}P$ heterostructure p-n diode. The luminescence peak is at 685 nm.

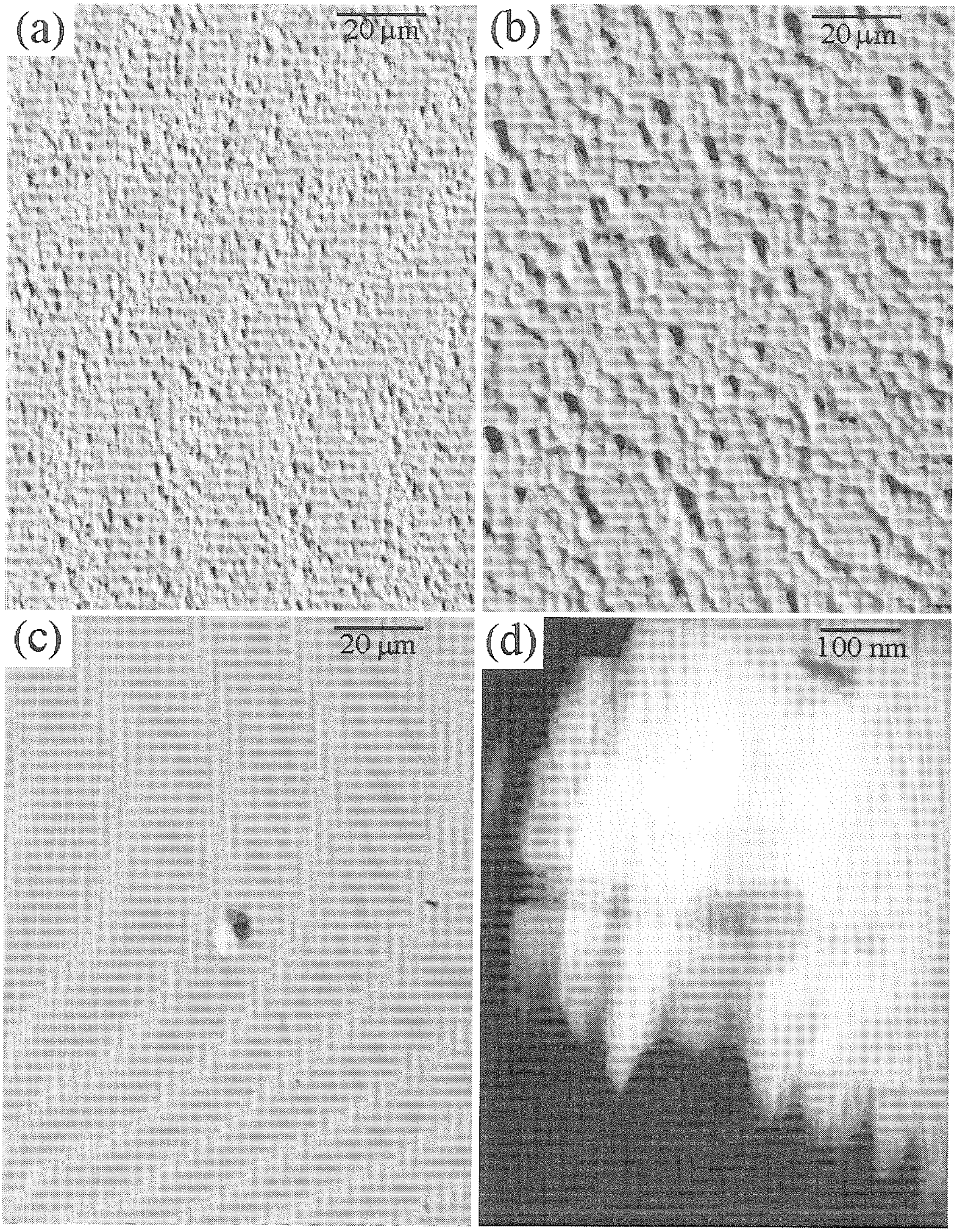

Figure 8.7. Optical micrographs at 680X of the various test structures (a)-(c) for the growth optimization of the MQW active region. Also shown is a cross-sectional transmission electron micrograph (d) of the MQW active region at 122,000X.

The p-type and the n-type $In_{0.5}Al_{0.5}P$ layers can also be seen. The vertical striations in this micrograph are artifacts from TEM sample preparation. The sample imaged in this TEM micrograph corresponds to the sample in figure 8.7b.

The defect density of the MQW active region was also reduced to a negligible level by optimizing the gas-switching sequences. This can be seen in the picture sequence from figures 8.7a to 8.7c. Seen in figure 8.7a, the first test structure grown containing only the MQW active region is densely packed with surface defects. The defects are so dense that their individual sizes are limited by the close spacings between defects. Through improved gas-switching and the elimination of flow-rate changes through the OM source bubblers, the defect density was reduced to the extent where the individual defects were allowed to develop into their full sizes, as seen in figure 8.7b, and a few flat areas between the defects became noticeable. For figure 8.7c, the single defect, seen at the center, had to be located specifically, since the defect density was so low. Between figures 8.7b and 8.7c, the number of surface defects was reduced dramatically by rearranging the gas-switching sequences during the growth of the p-type layers.

8.4 Growth of Complete VCSEL Structure

The chronology of the OMVPE development of the visible-wavelength VCSEL structure is summarized in the optical micrographs (680X) of figure 8.8. Complete VCSEL structures including the $\lambda/4$-stack mirror and the MQW active region were grown during various phases of the development. The very first full VCSEL structure grown is shown in figure 8.8a. This structure contained the first mirror and the first MQW active region before any optimization of the OMVPE growth parameters. The surface morphology was extremely rough. The large and dense defects arose from both the mirror and the MQW active region. The second full VCSEL structure grown is shown in figure 8.8b. The $\lambda/4$-stack mirror had been optimized at this point. The defects arose solely from the MQW active region. The third full VCSEL structure

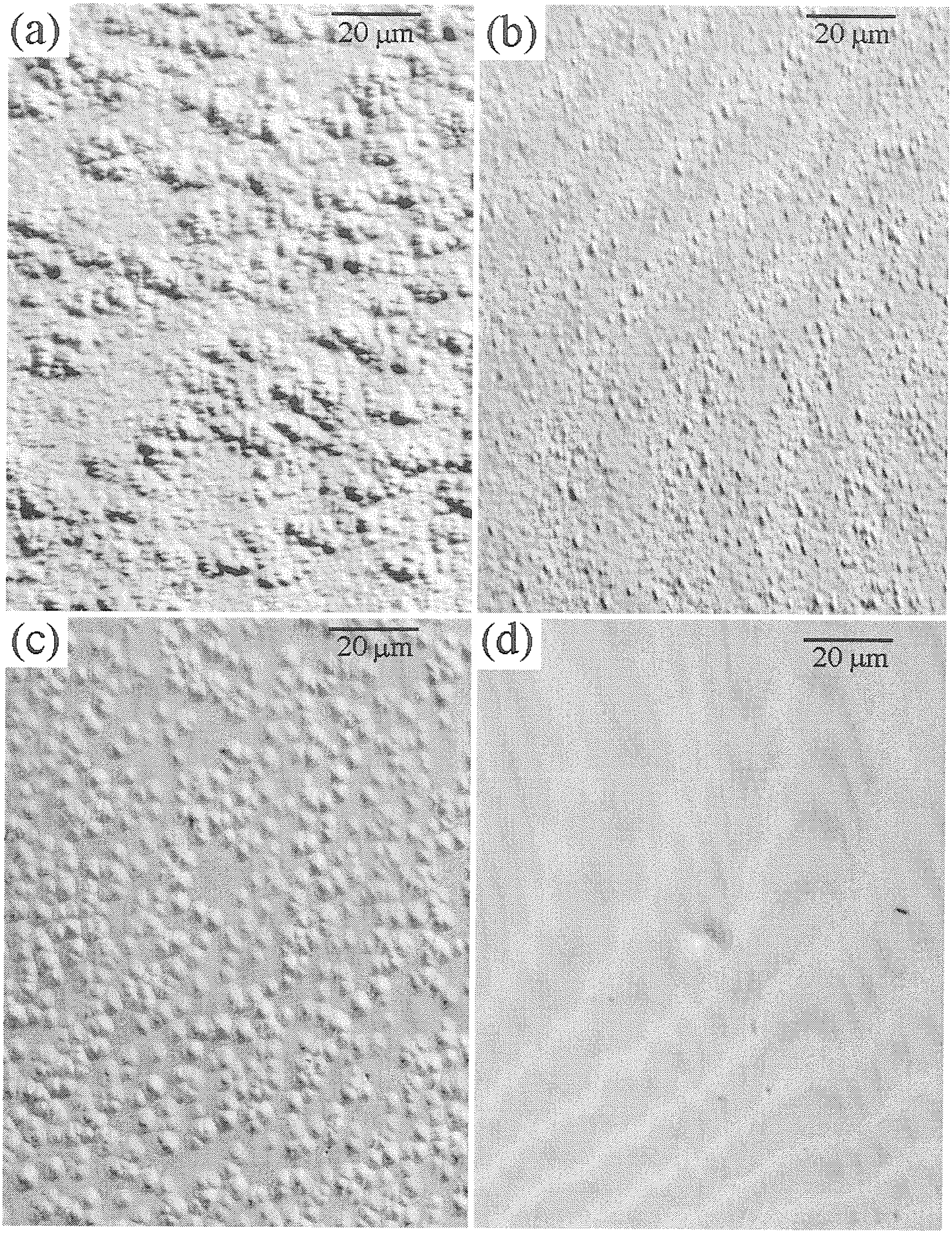

Figure 8.8. Optical micrographs at 680X of four full VCSEL structures containing the λ/4-stack mirror and the MQW active region grown by OMVPE.

grown is shown in figure 8.8c. The defect density of the MQW active region had been reduced considerably. Flat clear areas between defects are clearly visible. Containing the optimized mirror and the optimized MQW active region, the fourth and final full VCSEL structure grown thus far is shown in figure 8.8d. The single defect, seen at the center, had to be located specifically, since the defect density was so low. With this final VCSEL structure, it should be possible to produce a working visible-wavelength VCSEL.

Bibliography

[1] R. P. Schneider, Jr., R. P. Bryan, J. A. Lott, and G. R. Olbright, Appl. Phys. Lett. **60**, 1830 (1992).

[2] R. P. Schneider, Jr., R. P. Bryan, J. A. Lott, E. D. Jones, and G. R. Olbright, J. Crystal Growth **124**, 763 (1992).

[3] R. P. Schneider, Jr. and J. A. Lott, Appl. Phys. Lett. **63**, 917 (1993).

[4] K. Tai, K.-F. Huang, C.-C. Wu, and J. D. Wynn, Appl. Phys. Lett. **63**, 2732 (1993).

[5] S. Adachi, J. Appl. Phys. **58**, R1 (1985).

[6] D. E. Aspnes, S. M. Kelso, R. A. Logan, and R. Bhat, J. Appl. Phys. **60**, 754 (1986).

[7] A. Thelen, *Design of Optical Interference Coatings*, McGraw-Hill (1989).

[8] H. Tanaka, Y. Kawamura, and H. Asahi, J. Appl. Phys. **59**, 985 (1986).

[9] R. W. Glew, J. Crystal Growth **68**, 44 (1984).

[10] E. Veuhoff, T. F. Kuech, and B. S. Meyerson, J. Electrochem. Soc. **132**, 1958 (1985).